UNCLASSIFIED
SECURITY CLASSIFICATION OF THIS PAGE (When Data Entered)

REPORT DOCUMENTATION PAGE

READ INSTRUCTIONS BEFORE COMPLETING FORM

1. REPORT NUMBER: 15556.4-PH	2. GOVT ACCESSION NO.: A119844
3. RECIPIENT'S CATALOG NUMBER	
4. TITLE (and Subtitle): Nitrogen-14 NQR Study of Energetic Materials	5. TYPE OF REPORT & PERIOD COVERED: Final: 12 Feb 79 - 31 Jul 82
	6. PERFORMING ORG. REPORT NUMBER
7. AUTHOR(s): Robert A. Marino, Raymond F. Connors, Lawrence Leonard	8. CONTRACT OR GRANT NUMBER(s): DAAG29 79 C 0025
9. PERFORMING ORGANIZATION NAME AND ADDRESS: Block Engineering, Cambridge, MA 02139	10. PROGRAM ELEMENT, PROJECT, TASK AREA & WORK UNIT NUMBERS
11. CONTROLLING OFFICE NAME AND ADDRESS: U. S. Army Research Office, Post Office Box 12211, Research Triangle Park, NC 27709	12. REPORT DATE: Sep 82
	13. NUMBER OF PAGES: 167
14. MONITORING AGENCY NAME & ADDRESS (if different from Controlling Office)	15. SECURITY CLASS. (of this report): Unclassified
	15a. DECLASSIFICATION/DOWNGRADING SCHEDULE

16. DISTRIBUTION STATEMENT (of this Report)

Approved for public release; distribution unlimited.

17. DISTRIBUTION STATEMENT (of the abstract entered in Block 20, if different from Report)

NA

18. SUPPLEMENTARY NOTES

The view, opinions, and/or findings contained in this report are those of the author(s) and should not be construed as an official Department of the Army position, policy, or decision, unless so designated by other documentation.

19. KEY WORDS (Continue on reverse side if necessary and identify by block number)

molecular structure
electronic structure
trinitrotoluene
nuclear quadrupole resonance spectroscopy
crystallography
HMX
RDX

20. ABSTRACT (Continue on reverse side if necessary and identify by block number)

The complete Nitrogen-14 NQR Spectrum of TNT was obtained for both the stable Phase (monoclinic) and the unstable (orthorhombic) phase. It was established that quadrupole coupling data are very sensitive to and can yield a measure of the angle of twist of the plane of the NO_2 group away from the plane of the benzene ring about the CN bond. For the high explosive 1,3,5,7-tetranitro-1,3,5,7-tetraazacyclooctane (HMX), an analysis of the Nitrogen-14 NQR Spectrum and its temperature dependence yield details of the motion of the molecule in the solid.

DD FORM 1 JAN 73 1473 EDITION OF 1 NOV 65 IS OBSOLETE

UNCLASSIFIED
SECURITY CLASSIFICATION OF THIS PAGE (When Data Entered)

AD A119844
DTIC FILE COPY
DTIC ELECTE OCT 4 1982
82 10 04 053

20. ABSTRACT CONTINUED

The Nitrogen-14 NQR Spectrum of RDX at 77°K was also reported. Finally, two instrumentation advances were made. A New pulse sequence, labelled SORC for Strong-Off-Resonant Comb of RF pulses, was introduced and some of its properties were studied. In addition, moved by a desire to display as much as possible of the crowded NQR spectrum of TNT as possible, Fourier transform techniques were extended to obtain close to an order-of-magnitude increase in the breadth of the spectrum displayed in a single Fourier transform.

Accession For
NTIS GRA&I ☑
DTIC TAB ☐
Unannounced ☐
Justification
By
Distribution/
Availability Codes
Dist | Avail and/or Special
A

DTIC COPY INSPECTED 2

BLOCK
ENGINEERING, INC.

Cambridge, Mass. 02139 •

BE-82-949

NITROGEN-14 NQR STUDY OF ENERGETIC MATERIALS

SEPTEMBER, 1982

by

Robert A. Marino
Raymond F. Connors
Lawrence Leonard

Submitted to:

Department of the Army
U.S. Army Research Office
Research Triangle Park
North Carolina 27709

Contract No. DAAG-29-79-0025

Submitted by:

BLOCK ENGINEERING
Division of Bio-Rad Laboratories, Inc.
19 Blackstone Street
Cambridge, Massachusetts 02139

BLOCK
ENGINEERING

TABLE OF CONTENTS

Section		Page
1.0	INTRODUCTION	1-2
2.0	EXPERIMENTAL TECHNIQUES	2-1
2.1	Pulsed Techniques for Nitrogen-14 NQR	2-1
2.1.1	Free Induction Decay	2-2
2.1.2	Spin-Echo and Carr-Purcell (CP) Sequence	2-3
2.1.3	Spin-Lock Spin-Echoes (SLSE)	2-5
2.1.4	Strong Off-Resonance Comb (SORC) of RF Pulses	2-5
2.2	Fourier Transform Techniques for Nitrogen-14 NQR	2-18
2.2.1	Broadband Fourier Transform Techniques for Nitrogen-14 NQR	2-33
2.3	Temperature Dependence	2-40
2.4	A Method to Pair Up ν_- and ν_+ Lines	2-44
3.0	NQR STUDY OF TNT	3-1
3.1	Sample Preparation and NQR Spectrum	3-2
3.2	Structure and Bonding of TNT:General	3-6
3.2.1	Structure and Bonding of TNT:Townes-Dailey Theory	3-9
3.2.2	Structure and Bonding of TNT:Nitro Group Conformation	3-13
3.2.3	Structure and Bonding of TNT: Supporting NQR Data	3-17
3.3	Temperature Dependence	3-21
4.0	NQR STUDY OF HMX AND RDX	4-1
4.1	Introduction	4-1
4.2	Experimental	4-3
4.3	Results and Discussion	4-5
5.0	CONCLUSIONS AND RECOMMENDATIONS	5-1
6.0	ACKNOWLEDGEMENTS	6-1
APPENDIX A	NQR Theory	A-1
APPENDIX B	TNT Spectra	B-1
APPENDIX C	Broadband FT Spectrum of Exceptional Wide NQR Lines	C-1
APPENDIX D	Princeton Applied Research Interface	D-1
	References	R-1

LIST OF TABLES

Tables		Page
2.2-I	Lorentzian FID and Echo Complex Signals and Their Fourier Transform	2-20
3.1-I	Nitrogen-14 NQR Spectra of Trinitrotoluene	3-5
3.2-1-I	sp^2 Hybrid Orbitals and Occupation Numbers of the Nitrogen Site in C-Nitro Compounds	3-12
3.2.3-I	Nitrogen-14 NQR Spectral Data for Some Nitrobenzenes at 77°K	3-18
3.3-I	List of Twelve Nitrogen-14 NQR Spectral Frequencies for Monoclinic TNT as a Function of Temperature from 77°K to 321°K	3-23
3.3-II	List of Twelve Nitrogen-14 NQR Spectral Frequencies for Orthorhombic TNT as a Function of Temperature from 77°K to 279°K	3-24
3.3-III	The Components q_{xx}, q_{yy}, and q_{zz} of the Electric Field Gradient Tensor of Monoclinic TNT at 77°K and at 321°K	3-30
3.3-IV	The Components q_{xx}, q_{yy}, and q_{zz} of the Electric Field Gradient Tensor of Orthorhombic TNT at 77°K and at 279.6°K	3-32
3.3-V	The Root Mean Square Libration Angle at Room Temperature for Monoclinic and Orthorhombic TNT	3-33
4.3-I	^{14}N NQR Data for the Amine Nitrogen Atoms of β-HMX	4-6
4.3-II	^{14}N NQR Data Measured in RDX at 77°K	4-9
4.3-III	The Hybrid Orbitals of the Amine Nitrogen Atoms According to the Axis System	4-14
4.3-IV	The Hybrid Orbital Occupations of the Amine Nitrogen Atoms.	4-17
4.3-V	The Temperature Coefficients for the Axial and Equatorial Amine Atoms of HMX	4-22

BLOCK ENGINEERING

LIST OF FIGURES

Figures		Page
2.1.1-1	Parameters for Carr-Purcell Sequence	2-4
2.1.3-1	Spin-Locked-Spin-Echo (SLSE) train for ν_- line of $NaNO_2$ at 77°K. Transmitter frequency set at center of resonance line.	2-6
2.1.3-2	Spin-Locked-Spin-Echo train for ν_- line of $NaNO_2$ at 77°K. The transmitter frequency was chosen a few kHz away from resonance.	2-7
2.1.3-3	Double logarithmic plot of $T_{2\varepsilon}$, the long decay constant (ε= effective) of the spin of the echo train vs. τ, the spacing of the first two pulses in the SLSE excitation sequence. The transition is the ν_- line of $NaNO_2$ at 77°K at 3757kHz. Also shown are the relaxation times T_1 and T_2 for the transition.	2-8
2.1.4-1a	Parameters	2-11
2.1.4-1b	NQR Signal	2-11
2.1.4-1c	NQR Signal vs. Resonance Offset	2-11
2.1.4-2 a-e	Trace of steady state nuclear induction signal in a SORC sequence for various values of the pulse spacing, τ. Signals are to scale. All data were taken on the ν_- line of $NaNO_2$ at 77°K.	2-13
2.1.4-2 f-j	Continuation of Figure 2.1.4-2. Figures 2.1.4-2e and 2.1.4-2f are identical signals displayed with two different scales.	2-13
2.1.4-3	A semilogarithmic plot of the type I signal height vs. the pulse spacing parameter, τ. The data are taken from Figure 2.1-6.	2-14
2.1.4-4	A plot of magnitude of type II signals vs. the time average value if the RF field, $\langle H_1 \rangle$, using a SORC sequence. All data were taken on the ν_- line of $NaNO_2$ at 77°K with Δf = 3.5/2 kHz; τ = 3 msec.	2-16
2.1.4-5	A plot of the magnitude of type II signals vs. the time-average value of the RF field, $\langle H_1 \rangle$, using a SORC sequence. Data at 77°K with f = 1.5/2 kHz; τ = 1 msec.	2-17
2.2-1	Computer-simulated exponential FID signal (a) and its Fourier transform (b-e). (a) time domain signal [$e^{-\alpha t}\cos \omega t$]; (b) cosine FT of (a); (c) sine FT, (d) modulus squared (C^2+S^2) (e) modulus FT, $\sqrt{C^2+S^2}$	2-21

BLOCK ENGINEERING

LIST OF FIGURES (CONTINUED)

Figures		Page
2.2-2	Computer-simulated exponential echo signal (a) and its Fourier transforms (b-e). (a) time domain signal $[e^{-\alpha\|t\|}\cos \omega t]$; (b) cosine FT of (a); (c) Sine FT vanishes in this case; (d) modulus squared FT, (C^2+S^2). (e) modulus FT, $\sqrt{C^2+S^2}$	2-22
2.2-3	Computer-simulated Gaussian FID signal (a) and its Fourier transforms (b-e) (a) time domain signal $[e^{-(\alpha t)^2}\cos \omega t, t \geq 0]$; (b) Cosine FT of (a); (c) Sine FT, (d) modulus squared FT, (C^2+S^2) (e) mdoulus FT, $\sqrt{C^2+S^2}$	2-23
2.2-4	Computer-simulated Gaussian echo signal (a) and its Fourier transforms (b-e). (a) time domain signal $[e^{-(\alpha t)^2}\cos \omega t]$; (b) Cosine FT; (c) Sine FT vanishes in this case; (d) modulus squared FT, (C^2+S^2) (e) modulus FT, $\sqrt{C^2+S^2}$	2-24
2.2-5	Computer-simulated exponential FID signal with phase shift (a) and its Fourier transforms (b-e). (a) time domain signal $[e^{-\alpha t}\cos (\omega t - \phi]$; (b) Cosine FT of (a); (c) Sine FT; (d) modulus squared FT, (C^2+S^2) (e) modulus FT $\sqrt{C^2+S^2}$	2-25
2.2-6	Computer-simulated exponential echo signals with phase shift (a) and its Fourier transforms (b-e). (a) time domain signal $[e^{-\alpha\|t\|}\cos (\omega t - \phi)]$; (b) Cosine FT of (a); (c) Sine FT; (d) modulus squared FT, (C^2+S^2) (e) modulus FT, $\sqrt{C^2+S^2}$	2-26
2.2-7	Computer-simulated Gaussian FID signal with phase shift (a) and its Fourier transforms (b-e). (a) time domain singal $[e^{-(\alpha t)^2}\cos(\omega t-\phi), t \geq 0]$; (b) Cosine FT of (a); (c) Sine FT; (d) modulus squared FT, (C^2+S^2) (e) modulus FT, $\sqrt{C^2+S^2}$	2-27
2.2-8	Computer-simulated Gaussian echo signal with phase shift (a) and its Fourier transforms. (a) time domain signal $[2^{-(\alpha t)^2}\cos (\omega t - \phi]$; (b) Cosine FT of (a); (c) Sine FT; (d) modulus squared FT, (C^2+S^2) (e) modulus FT, $\sqrt{C^2+S^2}$	2-28
2.2-9	Experimental N^{14} FID signal from hexamethylenetetramine (HMT) at room temperature (a) and its Fourier transforms (b-e). (a) time domain signal, (b) Cosine FT of (a); (c) Sine FT; (d) modulus squared (C^2+S^2) (e) modulus FT, $\sqrt{C^2+S^2}$	2-30
2.2-10	Experimental N^{14} FID signal from the ν_+ line in area at 77°K (a) and its Fourier transforms (b-e). (a) time domain signal, (b) Cosine FT of (a); (c) Sine FT; (d) modulus squared FT, (C^2+S^2) (e) modulus FT, $\sqrt{C^2+S^2}$	2-31

BLOCK ENGINEERING

LIST OF FIGURES (CONTINUED)

Figures		Page
2.2-11	Experimental N^{14} spin echo signal from the 727 kHz ν_- doublet in monoclinic TNT at 77°K (a) and its Fourier transforms (b-e). (a) time domain signal, (b) cosine FT of (a); (c) sine FT; (d) modulus squared FT, (C^2+S^2) (e) modulus FT, $\sqrt{C^2+S^2}$	2-32
2.2.1-1	Echo signal interferogram and its broadband Fourier transform showing all six ν_+ lines of monoclinic TNT at 77°K. Other parameters are given in the text.	2-36
2.2.1-2	Normalized spectrum of ν_+ lines of monoclinic TNT at 77°K.	2-38
2.2.1-3	Normalizing function for broadband FT of TNT which was used to obtain Figure 2.2-2 from Figure 2.2-1.	2-39
2.3-1	NQR Temperature Run Assemblies	2-42
2.3-2	Temperature Controller	2-43
2.4-1	Plot of the amplitude resultant from coherently adding echos in a single SLSE train vs. the applied static magnetic field expressed as the corresponding proton NMR resonance frequency. The NQR transition is the 811 kHz ν_- line of m-dinitrobenzene at 77°K.	2-45
3.1-1	NQR Spectrum of TNT (77°K). Brackets indicate paired lines.	3-3
3.2-1	Projection of the crystal and molecular structure of MONOCLINIC TNT on the a-c crystal plane. Data and figure obtained by JRC Duke (private communication,1982).	3-7
3.2-2	Projection of the crystal and molecular structure of ORTHORHOMBIC TNT on b-c crystal plane. Data and figure obtained by J.R.C. Duke (private communication, 1982).	3-8
3.2.1-1	Electric Field Gradient Principal Axes System for the N^{14} Site in the C-Nitro Group	3-11
3.2.2-1	A plot of the expression $(2\nu_- - 4/3\ \nu_+)$ as a function of the Nitrogen-14 lines for each six sites of monoclinic α-TNT at 77°K vs. θ, the angle of twist of the nitro-group the CN bond axis.	3-16

BLOCK ENGINEERING

LIST OF FIGURES (CONCLUDED)

Figures		Page
3.2.3-1	Plot of the parameter $(2\nu_- - \frac{4}{3}\nu_+)$, shown in the text to be proportional to the nitrogen $p\pi$ occupation number of the NO_2 group, vs. the sine of the angle of twist θ, of the NO_2 group away from the plane of the benezene ring.	3-22
3.3-1	Temperature dependence of the Nitrogen-14 NQR Spectrum of Monoclinic TNT.	3-26
3.3-2	Temperature dependence of the Nitrogen-14 NQR Spectrum of Orthorhombic TNT.	3-27
4.1-1	The HMX Molecule	4-2
4.3-1	An ORTEP plot of β-HMX. The equatorial amine atoms are N_2N_2' and the axial amines are N_3N_3'. The orientation of the principal axes of the moment of inertia, I, is shown.	4-11
4.3-2	The approximate orientation of the principal axes of the EFG tensor of the amine atoms. Z is perpendicular to the molecular plane.	4-13
4.3-3	The primary intermolecular interaction in β-HMX. The O_3 atom of the axial NO_2 groups engages in an electrostatic attraction with C_1 and C_2 and a repulsive interaction with N_3 of a neighboring molecule.	4-19
4.3-4	The temperature Dependence of e^2Qq/h for the axial and equatorial amines of HMX. The three temperature regions where $d(e^2Qq/h)/dT$ is constant are indicated with the lines.	4-21
4.3-5	$d(e^2Qq/h)/dT$ for each HMX site shows greater temperature sensitivity at the Equatorial site than at the Axial site.	4-23
4.3-6	A view along the "chains" of β-HMX molecules which form as a result of the interaction shown in Figure 4.3-3. Oscillations of the molecules along this chain are primarily responsible for the changes in $d(e^2Qq/h)dT$ with temperature.	4-27

BLOCK ENGINEERING

1.0 INTRODUCTION

1.1 PROGRAM GOALS

The aim of this program was to study the molecular and electronic structure of Trinitrotoluene (TNT) in its various crystal phases. Sample of cast TNT, which normally contain a mixture of orthorhombic and monoclinic phases, will often develop cracks and voids when orthorhombic monocrystals transform to the denser monoclinic phase upon annealing. The desire to learn more about the molecular structure and molecular dynamics of TNT in these two phases provides part of the rational for this study. Nitrogen-14 nuclear quadrupole resonance (NQR) techniques were proposed as singularly well suited to the problem and because they complement x-ray and other crystallographic studies. It was further proposed to study the molecular dynamics of TNT in the solid state. Finally, explosive systems, such as RDX and HMX, were proposed as candidates for an NQR study.

1.2 SUMMARY OF PROGRAM RESULTS

We have established that NQR studies are well suited to the characterization of explosive substances such as TNT, RDX, and HMX.

The complete Nitrogen-14 NQR Spectrum of TNT was obtained for both the stable phase (monoclinic) and the unstable (orthorhombic) phase. It was established that quadrupole coupling data are very sensitive to and can yield a measure of the angle of twist, θ, of the plane of the NO_2 group away from the plane of the benzene ring about the CN bond. The temperature dependence of the NQR data was then used to obtain $\langle\Delta\theta\rangle$ RMS, the root mean square angular displacements about the equilibrium value of θ at room temperature. Large values of $\langle\Delta\theta\rangle$ RMS were found in excess of 10° at room temperature. Also, large variations in $\langle\Delta\theta\rangle$ RMS were observed among different NO_2 groups.

For the high explosive 1,3,5,7-tetranitro-1,3,5,7-tetraaza-cyclooctane (HMX), an analysis of the Nitrogen-14 NQR spectrum and its temperature dependence yield details of the motion of the molecule in the solid. The Nitrogen-14 NQR spectrum of RDX at 77°K was also reported.

Finally, two instrumentation advances were made. A new pulse sequence, labelled SORC for Strong-Off-Resonant Comb of RF pulses, was introduced and some of its properties were studied. In addition, moved by a desire to display as much as possible of the crowded NQR spectrum of TNT as possible, Fourier transform (FT) techniques were extended to obtain close to an order-of-magnitude increase in the breadth of the spectrum displayed in a single Fourier transform.

BLOCK ENGINEERING

2.0 EXPERIMENTAL TECHNIQUES

Of the many experimental methods [1-3] suitable for the detection of nuclear quadrupole coupling in solids, pulsed NQR in conjunction with Fourier transform techniques[4] offer important advantages for the current project. Principal among these is the high resolution with which individual line shapes can be detected and displayed. This enables us to resolve, for example, all the features of the remarkably crowded Nitrogen-14 NQR spectrum of α-TNT: twenty-four lines were detected in the frequency region 700-900 kHz.

A brief discussion of the basic concepts of the theory of NQR is presented in Appendix A. The pulsed NQR spectrometer used in this work was developed at Block Engineering and has been published elsewhere[5]. In the next sections we will describe some of the specific advances in experimental techniques that were made during this project.

2.1 PULSED TECHNIQUES FOR NITROGEN-14 NQR

Extensive signal enhancement is often required before Nitrogen-14 nuclear quadrupole resonance lines can be displayed with satisfactory signal-to-noise ratio. The pulse sequence most suited to a particular situation and the data handling used are chosen with this in mind. Four possible pulse sequences are discussed below. The optimum choice depends on the value of the relaxation times of the particular transition under study.

2.1.1 Free Induction Decay

The NQR response of a single crystal to a resonant pulse of RF irradiation is completely analogous to the spin 1/2 NMR case. One difference is that the intensity of the free induction decay (FID) response depends on the orientation of the radio-frequency field H_1 with respect to the electric field gradient (EFG) principal axes system. For a spin I = 1 system, the three resonance lines ν_+, ν_- and ν_d can be observed only when the irradiation field H_1 is oriented, respectively, along the x,y, and z principal axes of the EFG tensor. As an example, for a ν_- line, the expected value of the magnetization along the y axis is proportional to:

$$\left(\frac{h\nu_-}{3kT}\right) \sin\left(\sqrt{2}\,\omega_1 t_w\right) \cos\left(2\pi\nu_- t\right) \qquad (2.1.1\text{-}1)$$

where $\omega_1 = \gamma H_1$ measures the intensity of the irradiation, and t_w is the duration of the irradiating pulse. The maximum response is obtained when:

$$\sqrt{2}\,\omega_1\, t_w = \sqrt{2}\,\gamma\, H_1 t_w = \pi/2 \qquad (2.1.1\text{-}2)$$

in analogy with the NMR case.

In NQR, however, the sample often consists of a polycrystalline powder. In such cases a convolution for all orientations must be made. The result[6] is that the $\sin(\sqrt{2}\omega_1 t_w)$ function in the expression for the expectation value of the magnetization becomes a Bessel function, $J_1(\sqrt{2}\omega_1 t_w)$. This function has its first maximum, analogous to a "90° pulse", at $\sqrt{2}\omega_1 t_w = 0.66\pi$ and not at 0.5π as the sine function. Similarly, the first null, corresponding to a "180° pulse" occurs for a value of the argument equal to 1.43π rather than simply to a value of π.

BLOCK ENGINEERING

The time constant of the free induction decay is labelled T_2^*. In solids this parameter is usually small, given the rigid-lattice broadening of energy levels caused by the magnetic dipole-diploe interaction.[7] Therefore, FID signals are usually at least partially masked by the instrument dead-time or recovery-time following each intense RF pulse. For these reasons FID signals are often not observed. This is so even in the case of ^{14}N NQR where the magnetic dipole-dipole interaction is quenched to first order because the nuclear spins have integer values.[8].

2.1.2 Spin Echo and Carr-Purcell (CP) Sequence

Following a FID experiment in a case where T_2 (spin-spin relaxation time) $>>T_2^*$ (FID time constant) it is possible to recall part of the magnetization not lost through T_2 processes by applying a "180° pulse" at a time τ after the first pulse. As is well known, an "echo" will form at the time 2τ; this echo signal can be repeatedly recalled[9] at integral multiples of this time, $2n\tau$, by the application of additional "180° pulses" at times $(2n-1)\tau$. The amplitude of the resultant echo train decays with time constant T_2 (Figure 2.1.1-1). Signal-to-noise enhancement can be obtained by coherently adding successive echoes in the sequence. The optimum time for co-addition is easily shown to be $1.26T_2$. Due to the generally small value of T_2 in solids, however, this method does not result in an appreciable enhancement of the signal-to-noise ratio.

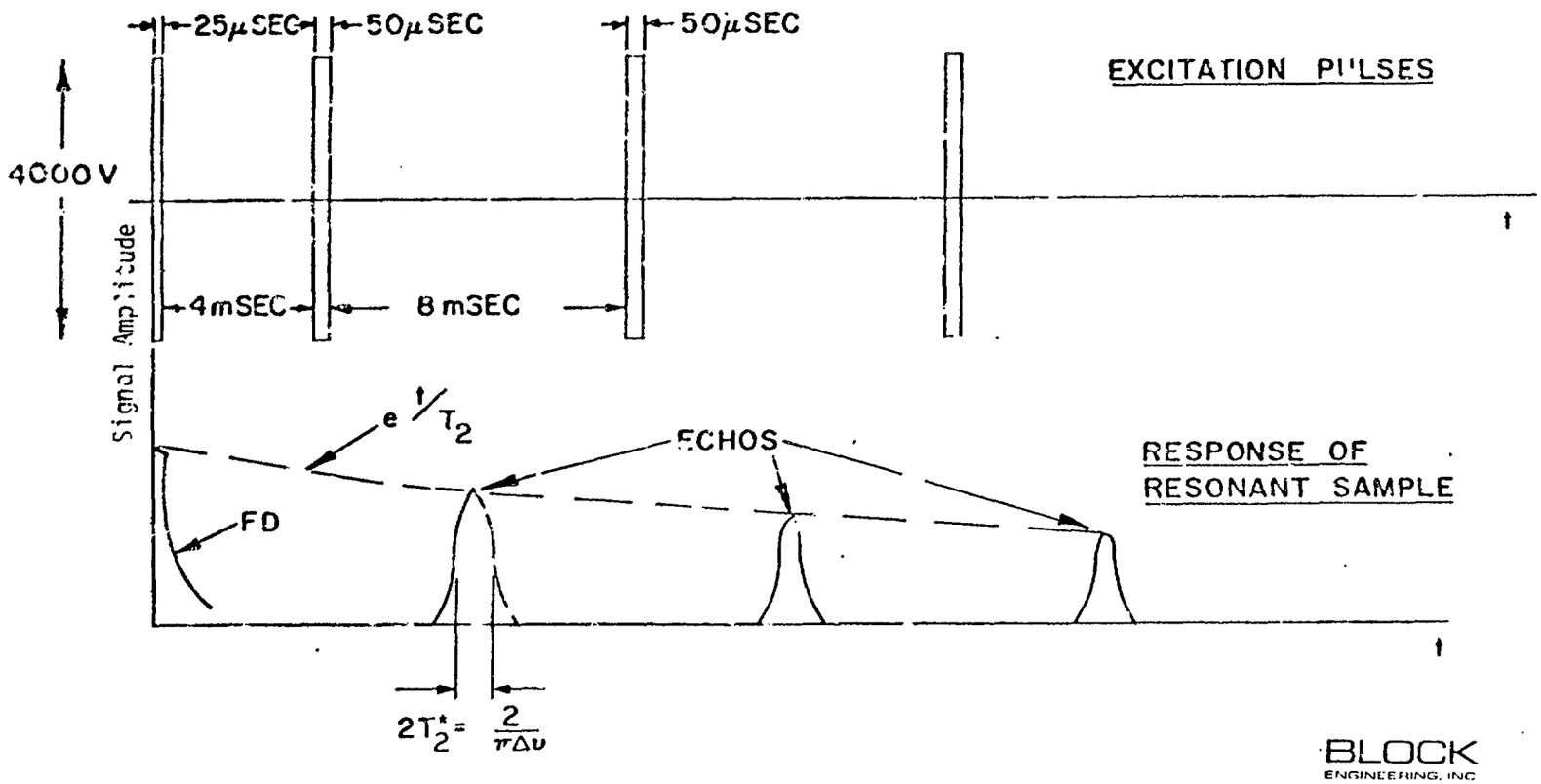

Figure 2.1.1-1. Parameters for Carr-Purcell Sequence

2.1.3 Spin-Lock Spin-Echoes (SLSE)

A major advance in S/N enhancement was made by Marino and Klainer[11] when an adaptation of the Ostroff-Waugh sequence[12] was applied to NQR. The sequence is essentially a Meiboom-Gill-modified-CP sequence[10] where all the pulses have the same flip angle of "90°", which means 0.66π in the NQR of an $I = 1$ nucleus. In Figure 2.1.3-1 ($NaNO_2$ at 77°K, at resonance) and Figure 2.1.3-2 ($NaNO_2$ at 77°K, slightly off resonance) it can be seen that the spin echo train in this sequence persists for times of an order of the spin lattice relaxation time, T_1, and not the much shorter T_2. Coherent addition of the echoes in this case results in considerable enhancement of the S/N, since $T_1 >> T_2$ is the typical situation in these solids. Marino and Klainer showed that the optimum enhancement is $0.64\ (T_{2\varepsilon}/2\tau)^{1/2}$ where $T_{2\varepsilon}$ is the effective decay constant of the echo train and 2τ is the spacing between echoes, or equivalently the spacing between pulses of the excitation sequence. It was further shown that the NQR effect was completely analogous to the spin 1/2, NMR case discussed by Waugh[13] in that the decay constant $T_{2\varepsilon}$ tends to $T_{1\rho}$ as τ is reduced to values less than T_2. Furthermore, for intermediate values of T_2, this parameter is proportional to τ^{-5}, again in analogy to NMR. Figure 2.1.3-3 shows this functional dependence for $NaNO_2$ at 77°K. Recently, Cantor and Waugh[14] have developed a theory to explain the main features of this NQR effect using a model of a polycrystalline solid with each nitrogen site having one nearest neighbor.

2.1.4 Strong Off-Resonance Comb (SORC) of RF Pulses

Recently we developed a new pulsed NQR experiment which can have considerable advantages in enhancing the S/N ratio of weak lines.[4]

BLOCK ENGINEERING

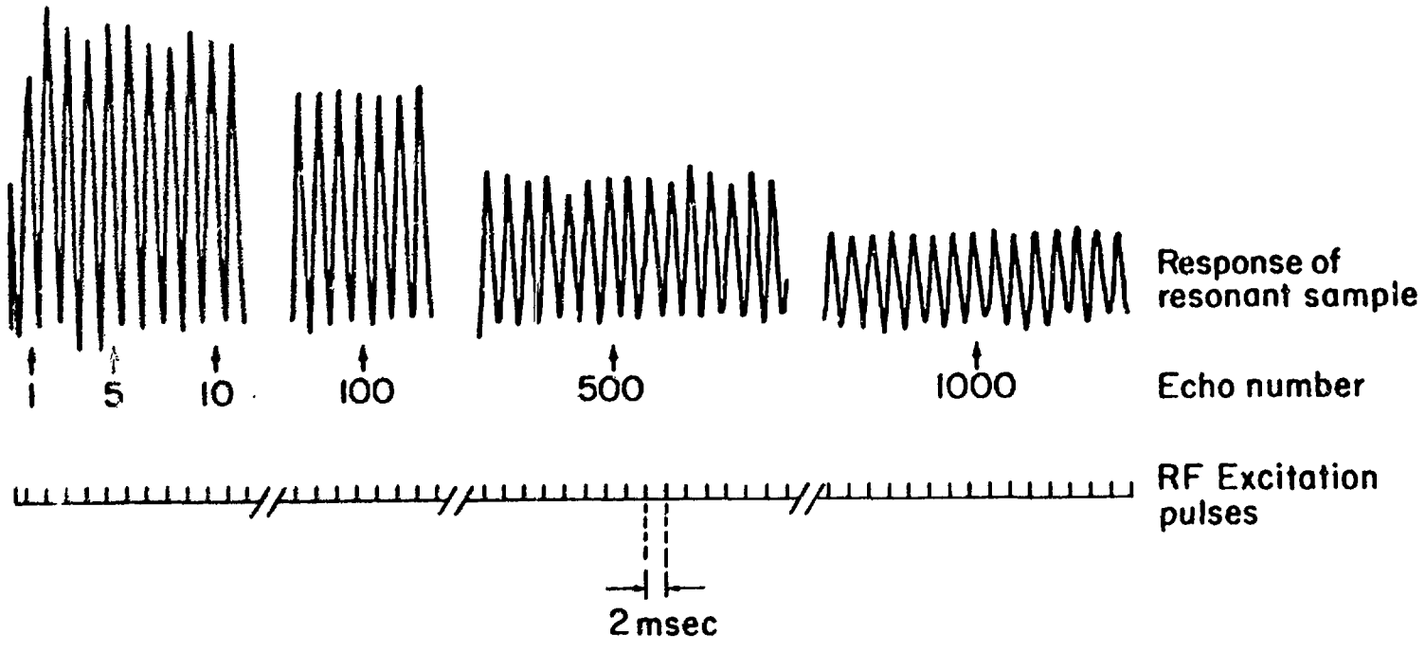

Figure 2.1.3-1. Spin-Locked-Spin-Echo (SLSE) train for ν_- line of $NaNO_2$ at 77°K. Transmitter frequency set at center of resonance line.

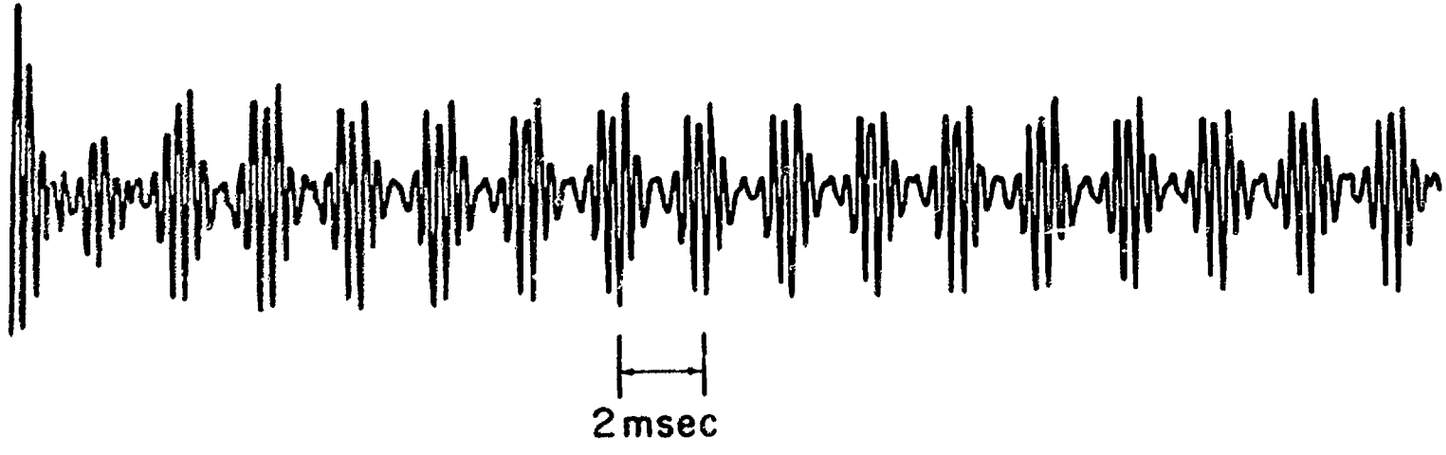

Figure 2.1.3-2. Spin-Locked-Spin-Echo train for ν_- line of $NaNO_2$ at 77°K. The transmitter frequency was chosen a few kHz away from resonance.

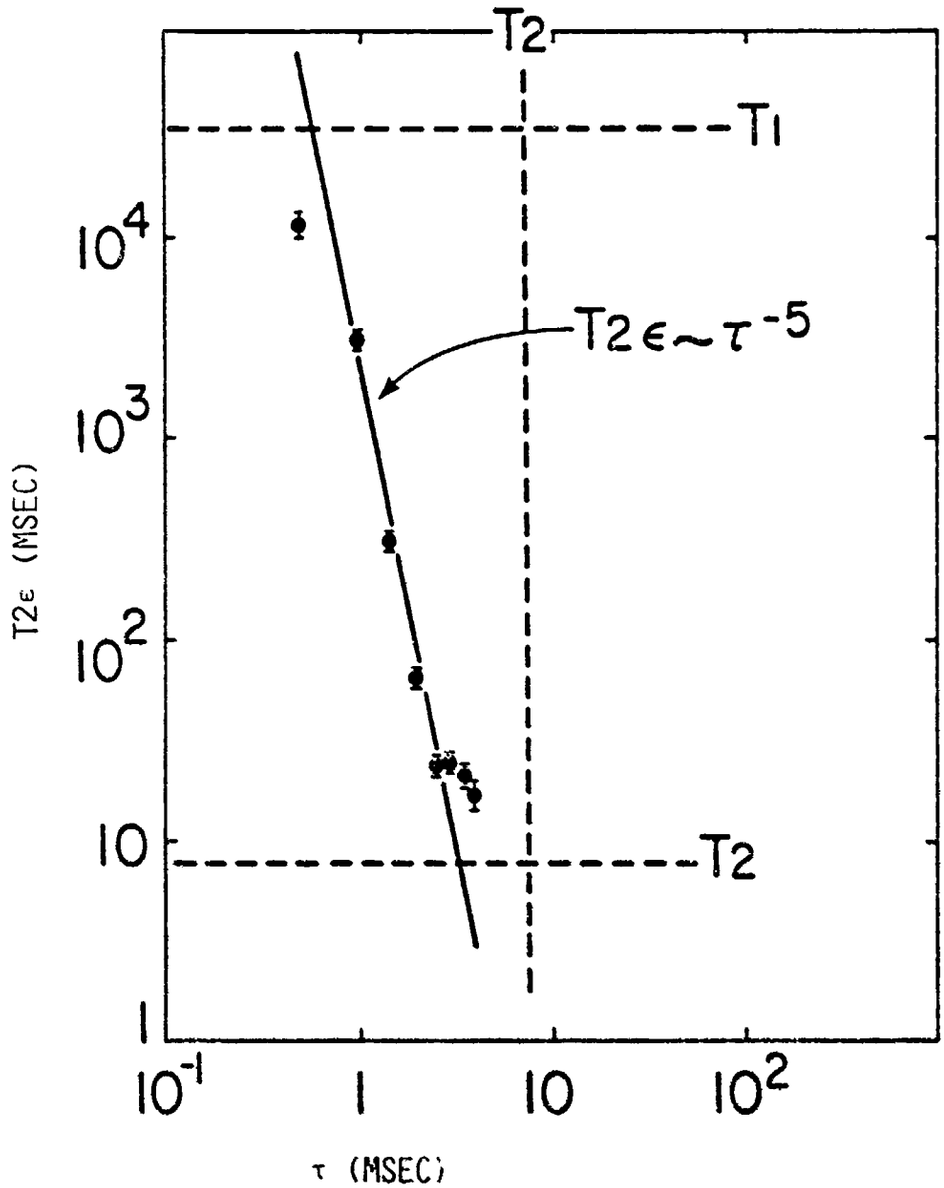

Figure 2.1.3-3. Double logarithmic plot of $T_{2\epsilon}$, the long decay constant (ϵ = effective) of the spin echo train vs. τ, the spacing of the first two pulses in the SLSE excitation sequence. The transition is the ν_- line of $NaNO_2$ at 77°K at 3757kHz. Also shown are the relaxation times T_1 and T_2 for the transition.

BLOCK
ENGINEERING

The steady state response of an ensemble of nuclear spins ($I = 1/2$) in high magnetic field H_o, to a strong radio-frequency field H_1, applied off resonance by Δf, has long been known.[8] When all the conditions for the establishment of a spin temperature in the rotating frame are met,[8] the x-component of the magnetization, M_x, which is experimentally observable, is given by the expression:

$$M_x = M_o \left[\frac{H_1 \ (2\pi\Delta f/\gamma)}{H_1^{\ 2} + H_{loc}^2 + (2\pi\Delta f/\gamma)^2} \right] \qquad (2.1.4\text{-}1)$$

where M_o is the equilibrium longitudinal magnetization, γ is the magnetogyric ratio of the nucleus, and H_{loc} is a measure of the local field at the nuclear site due to its neighbors. Results analogous to Equation 2.1.4-1 have also been derived and observed for a quadrupolar system[15] with nuclear spin $I = 3/2$ when subjected to the same strong, long, off-resonant irradiation, H_1.

The preliminary results obtained, when the irradiation field H_1 is applied in a long train of equally-spaced identical pulses, are presented here. Although the SORC experimental data reported here are for a quadrupolar, $I = 1$ system, analogous effects in a magnetic system or a quadrupolar system with spin different from unity can be expected.

Figure 2.1.4-1a defines the parameters of the SORC sequence. Here a train of radio-frequency pulses of duration t_w, spacing τ, Δf away from exact resonance is applied to a pure nuclear electric quadrupole system in zero external magnetic field.

BLOCK ENGINEERING

Figure 2.1.4-1a

a. Timing diagram for SORC sequence (Strong Off-Resonance Comb of RF pulses).

b. Overlay of nuclear induction signals obtained in SORC observation window when $\Delta f = 3/2$ kHz and $\Delta f = 3.5/2$ kHz. Note destructive interference in former case. All data were taken on the ν_- line of $NaNO_2$ at 77°K.

c. Plot of signal height obtained in the middle and right-hand side of observation window using the SORC sequence.

BLOCK
ENGINEERING

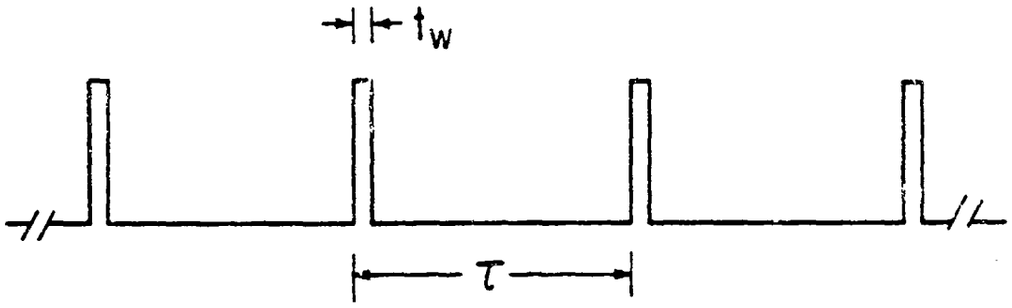

(a) Parameters

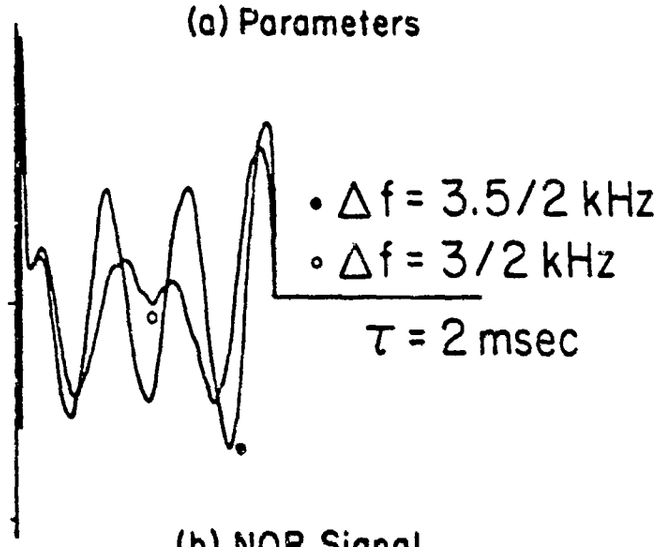

(b) NQR Signal

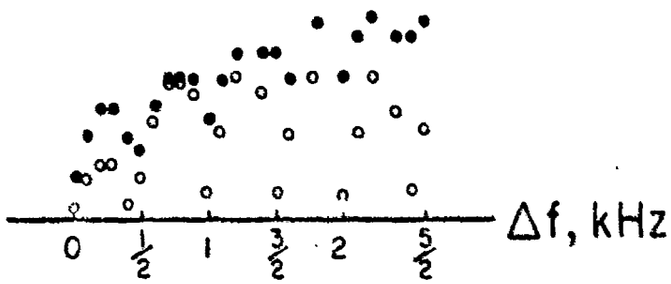

(c) NQR Signal vs. Resonance Offset

The variation of the signal amplitude vs. Δf, the distance from exact resonance, shows two features as depicted in Figures 2.1.4-1b and 2.1.4-1c. First, the signal amplitude is modulated by sinusoid of period $1/\tau$, the reciprocal of the pulse repetition rate. This phenomenon is best understood by considering that the Fourier transform of the transmitter pulses has periodicity $1/\tau$. This leads to successive maxima and minima in the NQR signal (Figures 2.1.4-1b and 2.1.4-1c) as the transmitter frequency is changed, i.e., Δf is varied. Alternatively, and more naively, this modulation can be interpreted as the destructive interfernece of type I signals (FID-like signals immediately following the RF pulse) and type II signals (immediately preceeding the RF pulse) in their overlap region as the frequency, Δf, is slowly varied.

Another feature shown in Figure 2.1.4-1c is the shape of the envelope, possibly conforming to a function of the type $\Delta f/(A^2 + \Delta f^2)$, such as Equation 2.1.1-2. Insufficient data have been taken so far to ascertain the degree of agreement with theory on this last point.

The nuclear induction signals present in the observation window between successive pulses of the SORC sequence are shown in Figure 2.1.4-2 as a function of the pulse separation τ. All data were taken on the ν_- line of $NaNO_2$ at 77°K. The magnitude of the type I signal is then plotted vs. τ in Figure 2.1.4-3. Note that for $\tau \geq 8$ msec, the magnitude of type I signals increases with τ, as might be expected for a FID signal subject to spin-lattice relaxation. On the other hand, for $\tau \leq 5$ msec, signals at both ends of the observation window are of a comparable size and they grow exponentially with decreasing τ; this is the region of interest.

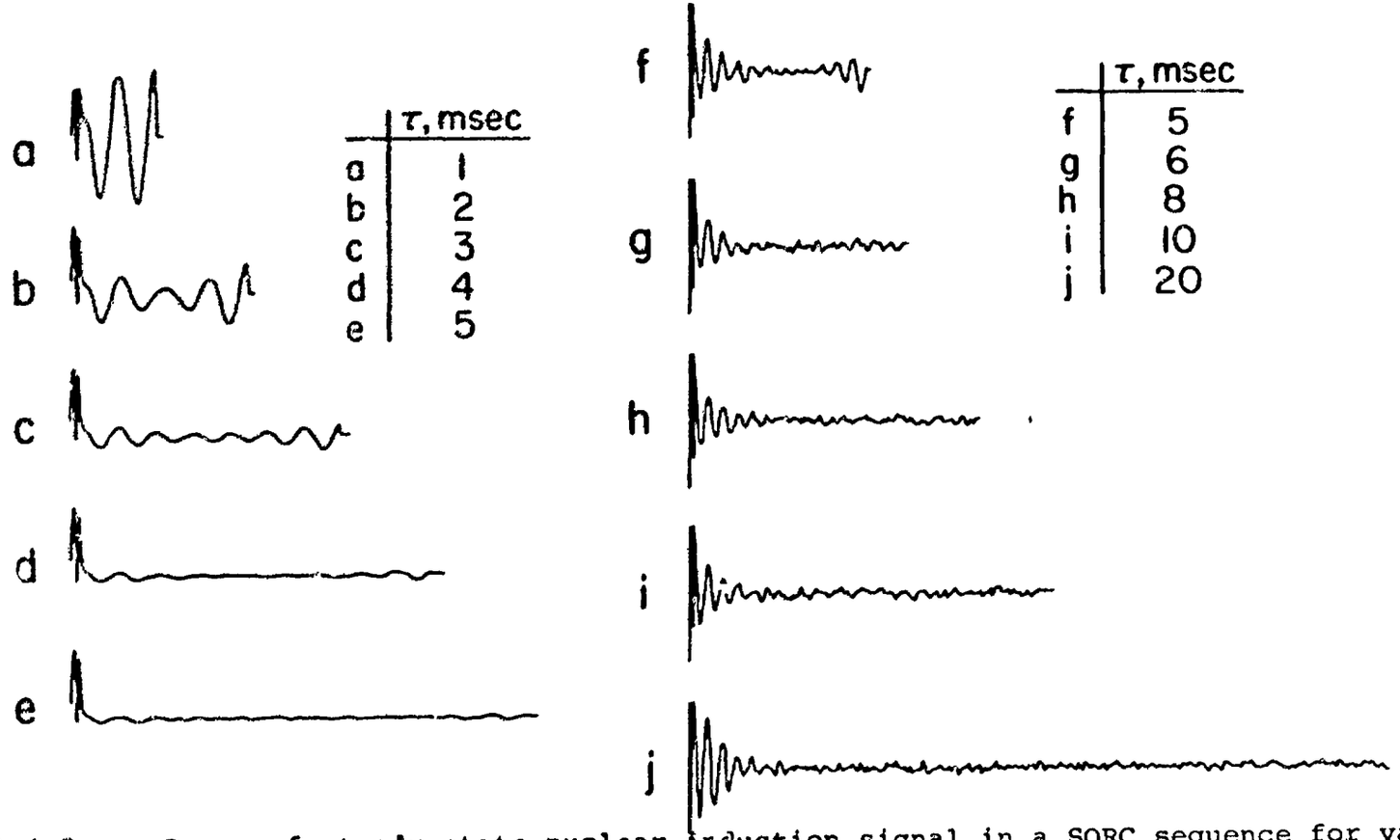

Figure 2.1.4-2 a-e Trace of steady state nuclear induction signal in a SORC sequence for various values of the pulse spacing, τ. Signals are to scale. All data were taken on the ν_- line of $NaNO_2$ at 77°K.

Figure 2.1.4-2 f-j Continuation of Figure 2.1.4-2. Figures 2.1.4-2e and 2.1.4-2f are identical signals displayed with two different scales.

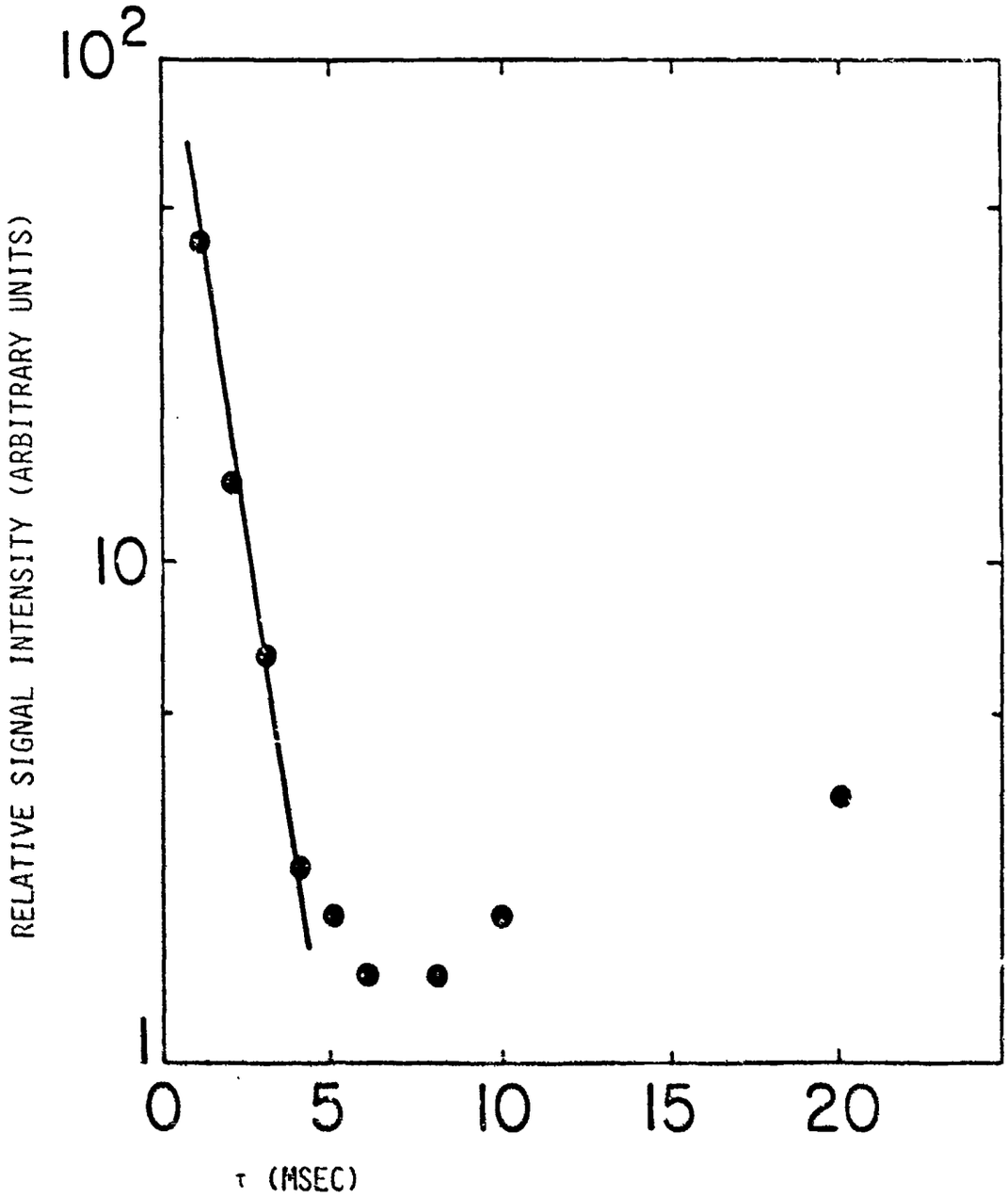

Figure 2.1.4-3. A semilogarithmic plot of the type I signal height (see text) vs. the pulse spacing parameter, τ. The data are taken from Figure 2.1-6.

BLOCK ENGINEERING

Figure 2.1.4-4 shows the variation of the type II signal vs. $\langle H_1 \rangle$ for τ = 3 msec. The experimental points are obtained for four different values of the instantaneous field, H_1, obtained by changing the pulse width, t_w, at constant "flip angle", $\sqrt{2}\ \gamma\ t_w H_1$. The dotted line is the curve $F = \langle H_1 \rangle / [\langle H_1 \rangle^2 + B^2]$ with B = 0.05 G. The fact that $\langle H_1 \rangle$, the average value, rather than H_1, the peak value, is the important parameter and that there is good agreement of the data with the form of Equation 2.1.1-2 is strong evidence that the ensemble of spins is responding to the time-average field of the SORC sequence in a manner analogous to the conventional long, strong, off-resonant pulse.

The size of the parameter B is found to be about 0.05G which is approximately two orders of magnitude too small for the value expected from the contribution of Δf to Equation 2.1.1-2. This discrepancy is reduced by a factor of 5 when the experiment is repeated for τ = 1 msec, as shown in Figure 2.1.4-5. Comparison of Figures 2.1.4-4 and 2.1.4-5 suggests that the pulsed nature of the experiment is still very important for τ = 1 msec and that quantitative agreement cannot be expected until τ is reduced further.

The potential of this technique for sensitive detection of NQR signals appears great since signals can be obtained and signal averaged at essentially 100% duty cycle. It also appears experimentally that the conditions for efficient signal collection on τ/T_2, the ratio of the pulse spacing to the spin-spin relaxation time, are slightly less stringent here then in the case of SLSE. However, further experimentation is needed to completely understand the operational parameters of SORC.

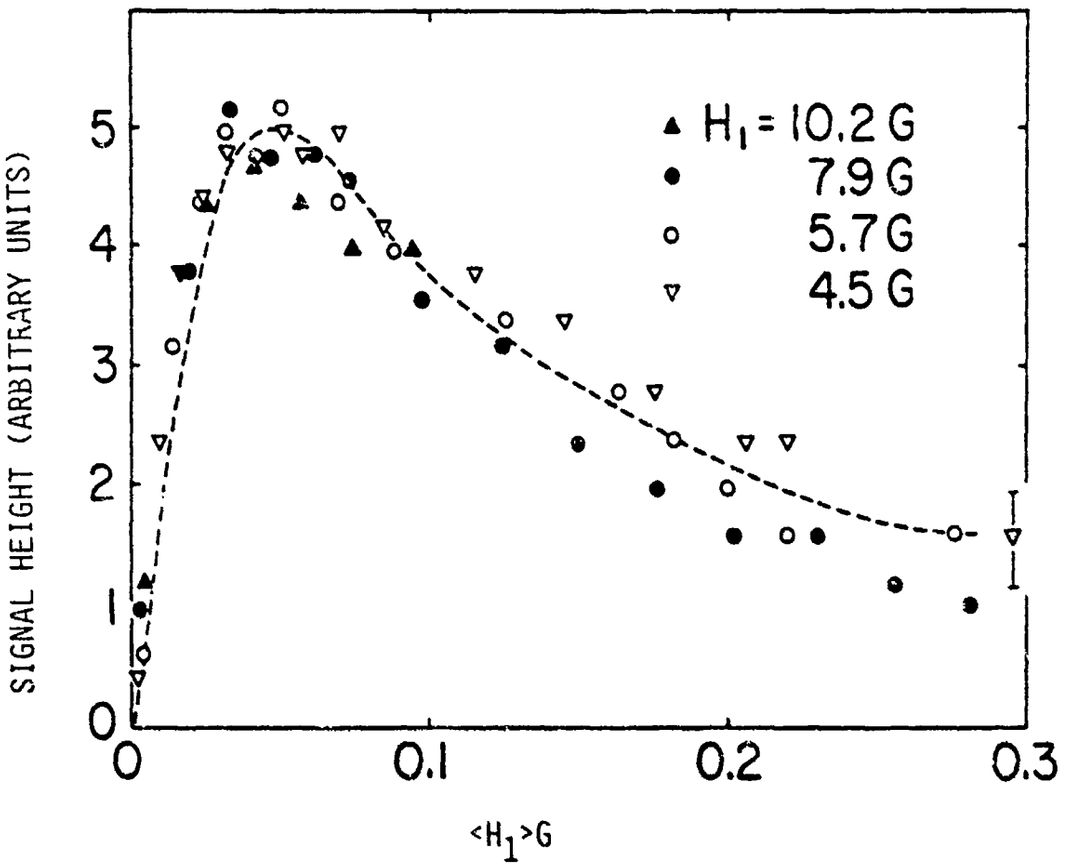

Figure 2.1.4-4. A plot of magnitude of type II signals (see text) vs. the time average value if the RF field, $\langle H_1 \rangle$, using a SORC sequence. All data were taken on the ν_- line of $NaNO_2$ at 77°K with Δf = 3.5/2 kHz; τ = 3 msec.

BLOCK ENGINEERING

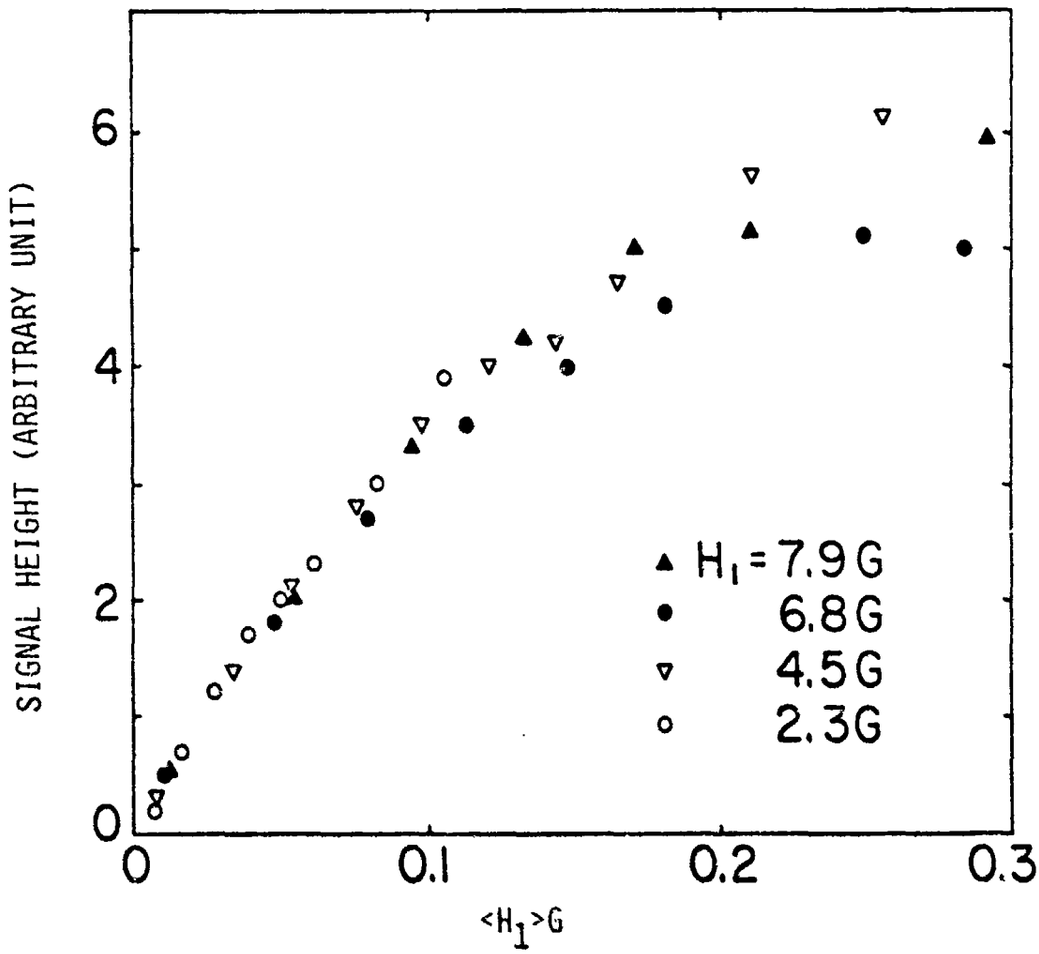

Figure 2.1.4-5. A plot of the magnitude of Type II signals (see text) vs. the time-average value of the RF field, $\langle H_1 \rangle$, using a SORC sequence. Data were taken on the ν_- line of $NaNO_2$ at 77°K with $f = 1.5/2$ kHz; $\tau = 1$ msec.

BLOCK ENGINEERING

2.2 FOURIER TRANSFORM TECHNIQUES FOR NITROGEN-14 NQR

There are three main reasons for doing FT spectroscopy:

a. Enhancement of signal-to-noise over CW methods. The enhancement is given by the square root of the ratio of the total width of the spectrum to the typical line width.

b. Pulsed methods are singularly well-suited to data processing.

c. The line shape is readily obtained directly from the output.

Of these, the first reason, probably the most important in other disciplines, is not nearly as important in NQR, because the ratio defined above is not large and can often be close to unity. This is so because in solids, line widths are relatively large (a few kHz) while the bandwidths which can be suitably irradiated are in the 10-100 kHz range. This implies that the NQR spectrum must be obtained over one short frequency interval at a time, and cannot usually be displayed in a single operation as is the case in high resolution nuclear magnetic resonance. The other two advantages, however, have provided the impetus for our development of FT-NQR techniques.

Once FID or echo signals have been obtained, the proper FT treatment for each will yield the desired lineshape spectrum[16,17]. In this section the procedures the authors found most satisfactory are discussed.

BLOCK ENGINEERING

The problem of phase correction for NQR spectra presents a particular problem not found in fixed-frequency spectrometers. By phase correction here we do not mean the usual procedure performed on FID data to correct for the first few missing data points lost in the spectrometer recovery time. Rather, we are concerned with the problem present in both FID and echo data that the output of our phase-sensitive receiver is a generally unknown admixture of "absorption" and "dispersion" signal. The degree of admixture varies in a complicated manner with the spectrometer operating frequency and tuning. The phase shift of the phase-sensitive receiver output away from true "absorption" can be considerable and must be mathematically corrected in order to obtain a true line shape from the time-domain data. In Table 2.2-I the mathematical results for Lorentzian lineshapes are collected as guides to the solution of this problem. (A more elegant solution would be possible if quadrature detection were available.)

The results in the table show that the presence of phase shifts produces an admixture of absorption and dispersion modes in the case of FID signals, and a possible loss of intensity in echo signals. This problem can be avoided while at the same time the true Lorentzian line shape is preserved, if the <u>modulus squared</u> transform is computed for FID signals, and the <u>modulus</u> transform is computed for echoes. Thus the proper line shapes are obtained in each case regardless of the degree and source of phase shift without need for a separate "phase correction" subroutine.

In Figures 2.2-1 to 2.2-8 the results of computer-simulated spectra are known. An echo and an FID signal have been simulated for both Lorentzian and Gaussian lineshapes. Cosine, Sine, the square of the modulus, and modulus transforms are computed and displayed. Figures 2.2-1 to 2.2-4 are for zero phase shift, while Figures 2.2-5 to 2.2-8 have a phase shift of 30° in the time domain signals. Note that in all cases the conclusions discussed for proper data processing are borne out, mainly that the <u>modulus squared</u> transform should be used for FID signals, and the <u>modulus</u> transform should be used for echo signals.

TABLE 2.2-I

LORENTZIAN FID AND ECHO COMPLEX SIGNALS AND THEIR FOURIER TRANSFORM

FID

TIME DOMAIN: $f(t) = e^{-\alpha t} e^{i\omega_0 t} e^{-i\phi} \quad t \geq 0$

C, Cosine transform $= \dfrac{1}{\alpha^2+(\omega-\omega_0)^2} \left\{\alpha\cos\phi - (\omega-\omega_0)\sin\phi\right\}$

S, Sine transform $= \dfrac{1}{\alpha^2+(\omega-\omega_0)^2} \left\{\alpha\sin\phi + (\omega-\omega_0)\cos\phi\right\}$

C^2+S^2, Modulus squared transform $= \dfrac{1}{\alpha^2+(\omega-\omega_0)^2}$

$[C^2+S^2]^{\frac{1}{2}}$, Modulus transform $= \left[\dfrac{1}{\alpha^2+(\omega-\omega_0)^2}\right]^{\frac{1}{2}}$

ECHO

TIME DOMAIN: $f(t) = \begin{cases} e^{\alpha t} e^{-i\omega_0 t} e^{-i\phi} & t < 0 \\ e^{-\alpha t} e^{i\omega_0 t} e^{-i\phi} & t \geq 0 \end{cases}$

C, Cosine transform $= \dfrac{1}{\alpha^2+(\omega-\omega_0)^2} \; 2\alpha\cos\phi$

S, Sine transform $= \dfrac{1}{\alpha^2+(\omega-\omega_0)^2} \; 2\alpha\sin\phi$

C^2+S^2, Modulus squared transform $= \left[\dfrac{2\alpha}{\alpha^2+(\omega-\omega_0)^2}\right]^2$

$[C^2+S^2]^{\frac{1}{2}}$, Modulus transform $= \left[\dfrac{2\alpha}{\alpha^2+(\omega-\omega_0)^2}\right]^2$

BLOCK ENGINEERING

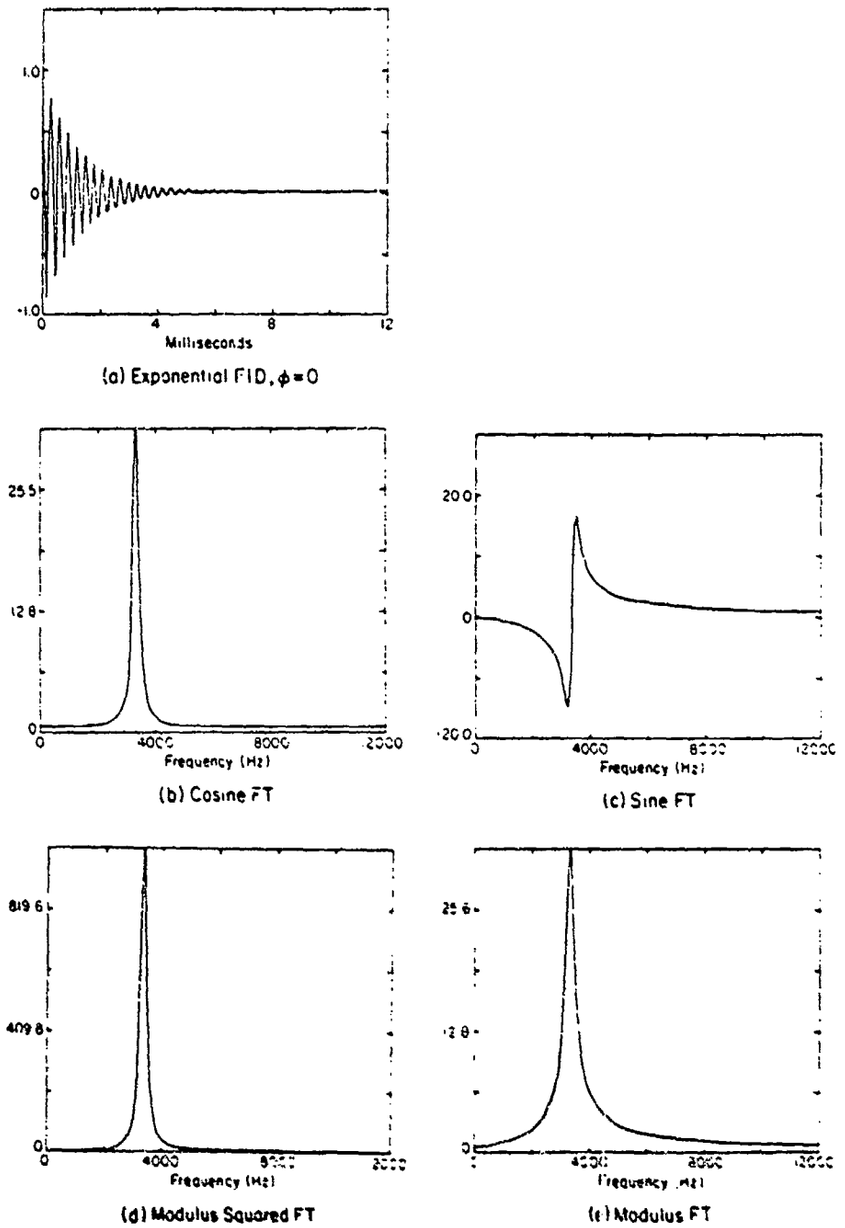

Figure 2.2-1. Computer-simulated exponential FID signal (a) and its Fourier transform (b-e). (a) time domain signal [$e^{-at}\cos \omega t$]; (b) Cosine FT of (a); (c) Sine FT, (d) modulus squared $(C^2 + S^2)$ (e) modulus FT, $\sqrt{C^2 + S^2}$

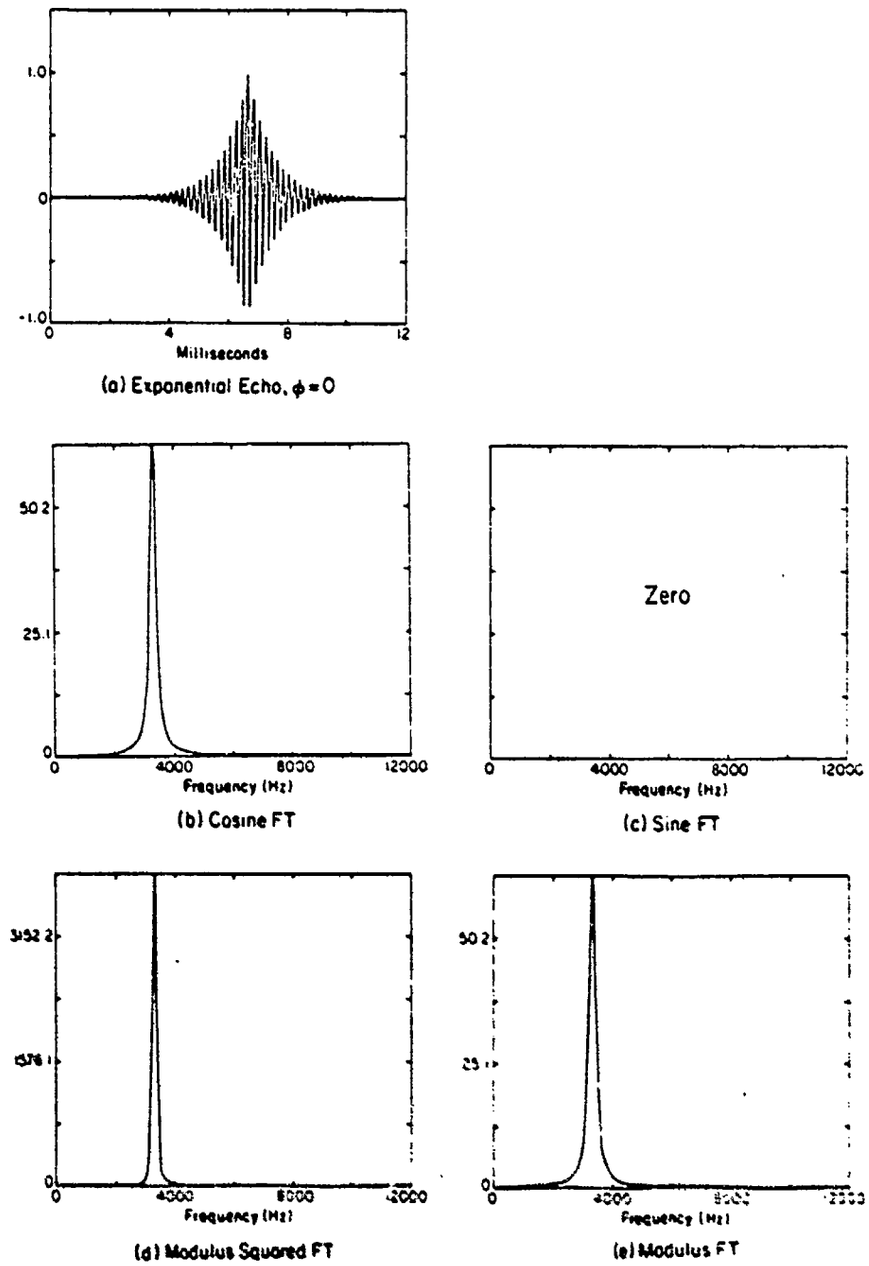

Figure 2.2-2. Computer-simulated exponential echo signal (a) and its Fourier transforms (b-e). (a) time domain signal $[e^{-\alpha|t|}\cos \omega t]$; (b) Cosine FT of (a); (c) Sine FT vanishes in this case; (d) modulus squared FT, $(C^2 + S^2)$. (e) modulus FT, $\sqrt{C^2 + S^2}$

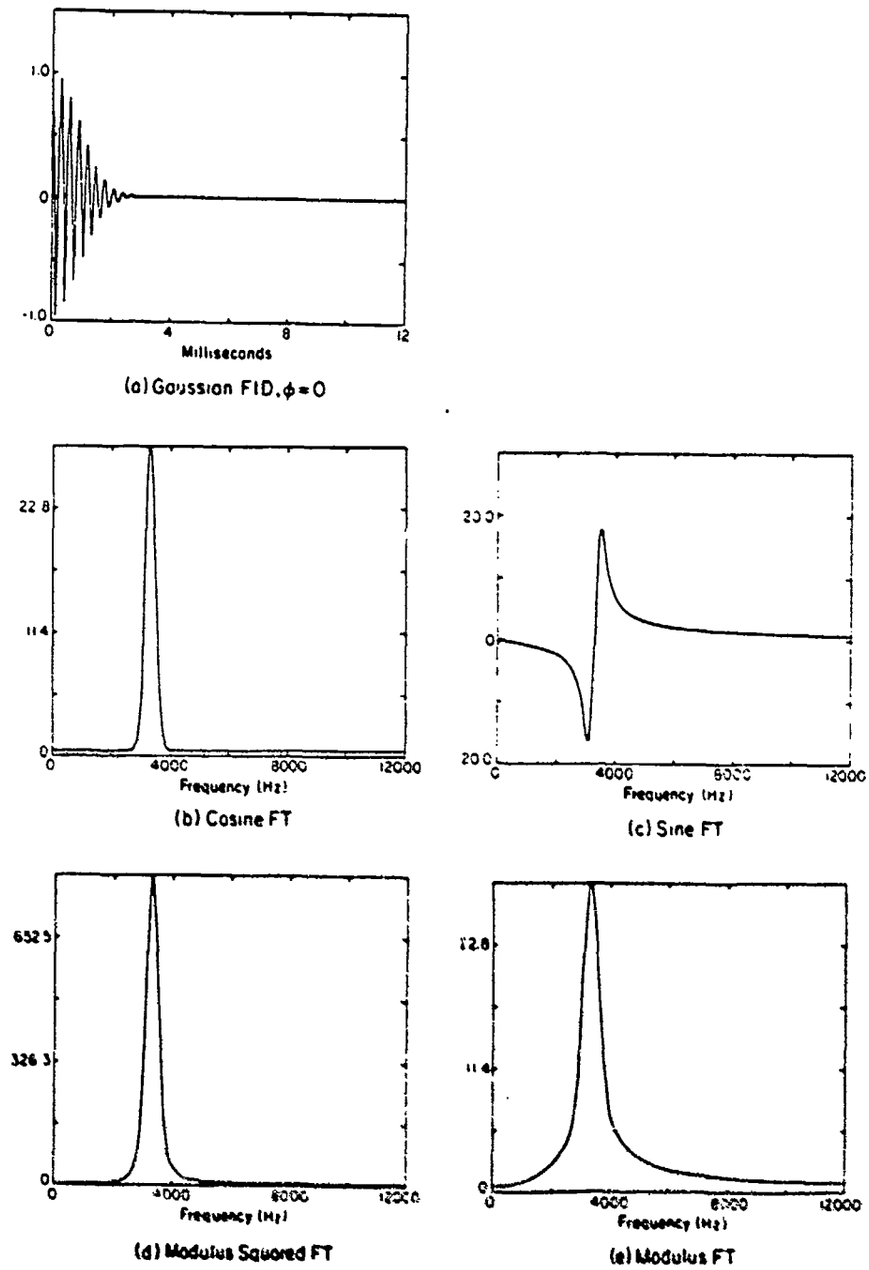

Figure 2.2-3. Computer-simulated Gaussian FID signal (a) and its Fourier transforms (b-e).
(a) time domain signal $[e^{-(\alpha t)^2}\cos \omega t, t \geq 0]$;
(b) Cosine FT of (a); (c) Sine FT,
(d) modulus squared FT, $(C^2 + S^2)$
(e) modulus FT, $\sqrt{C^2 + S^2}$

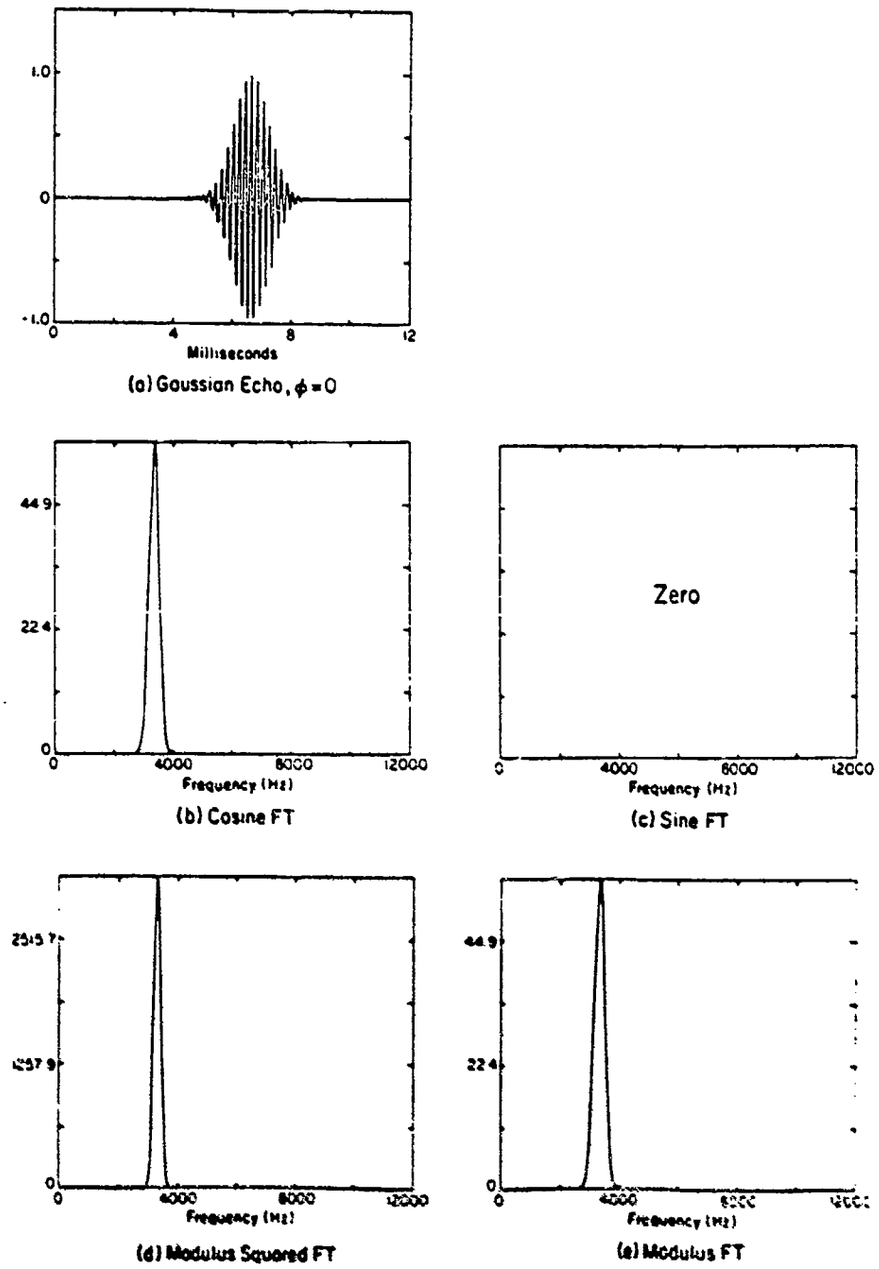

Figure 2.2-4. Computer-simulated Gaussian echo signal (a) and its Fourier transforms (b-e). (a) time domain signal $[e^{-(at)^2} \cos \omega t]$; (b) Cosine FT; (c) Sine FT vanishes in this case; (d) modulus squared FT, $(C^2 + S^2)$ (e) modulus FT, $\sqrt{C^2 + S^2}$

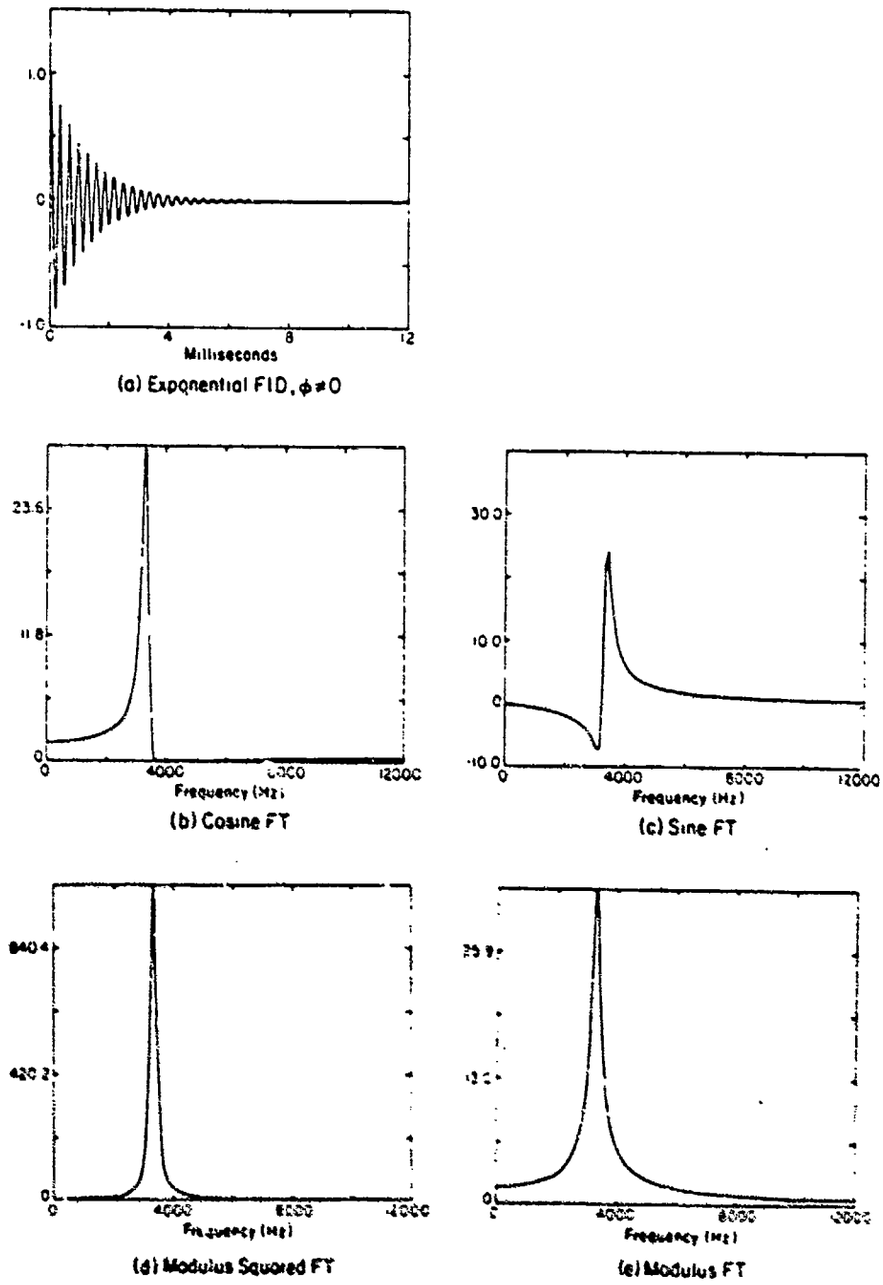

Figure 2.2-5. Computer-simulated exponential FID signal with phase shift (a) and its Fourier transforms (b-e). (a) time domain signal $[e^{-\alpha t}\cos(\omega t - \phi)]$; (b) Cosine FT of (a); (c) Sine FT; (d) modulus squared FT, $(C^2 + S^2)$ (e) modulus FT, $\sqrt{C^2 + S^2}$

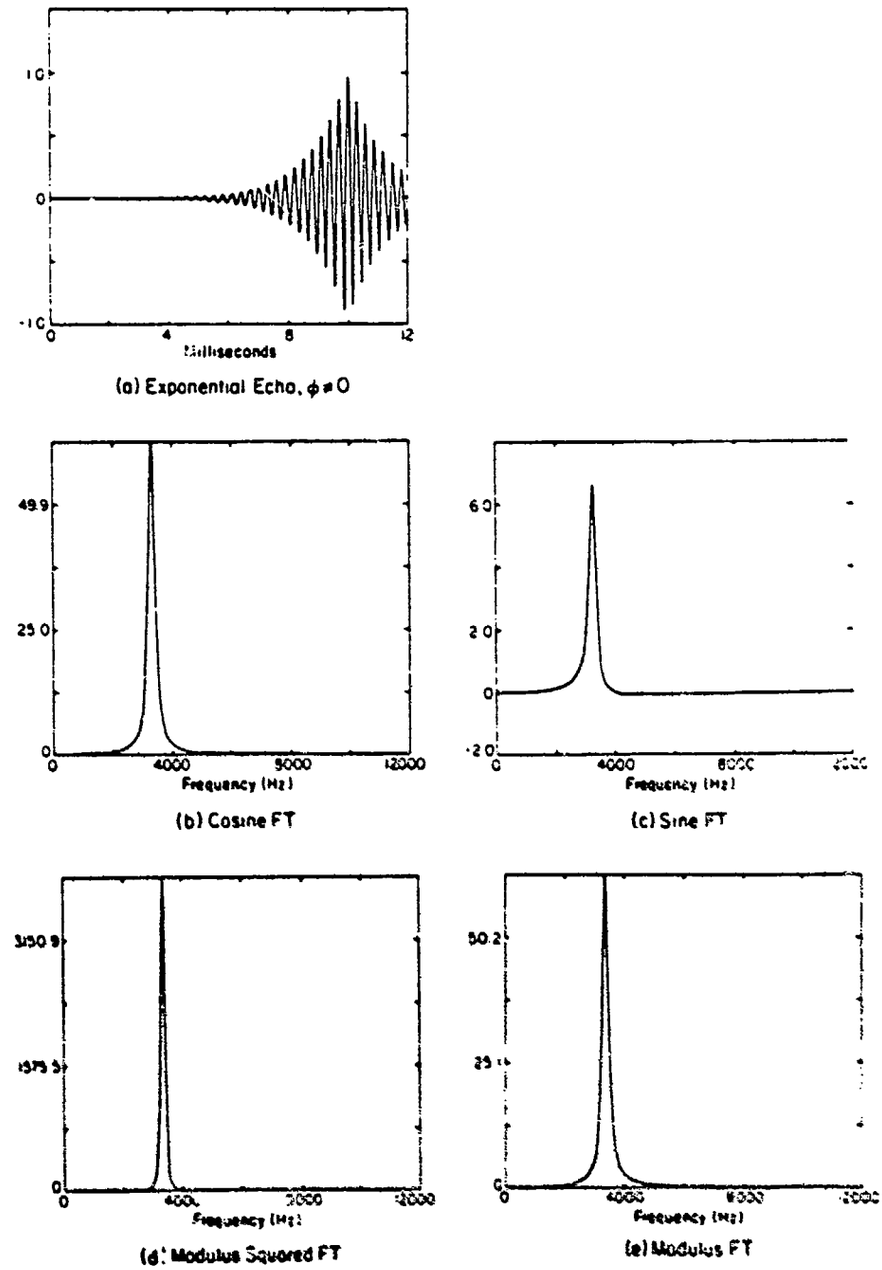

Figure 2.2-6. Computer-simulated exponential echo signals with phase shift (a) and its fourier transforms (b-e). (a) time domain signal $[e^{-a|t|}\cos(\omega t - \phi)]$; (b) Cosine FT of (a); (c) Sine FT; (d) modulus squared FT, $(C^2 + S^2)$ (e) modulus FT, $\sqrt{C^2 + S^2}$

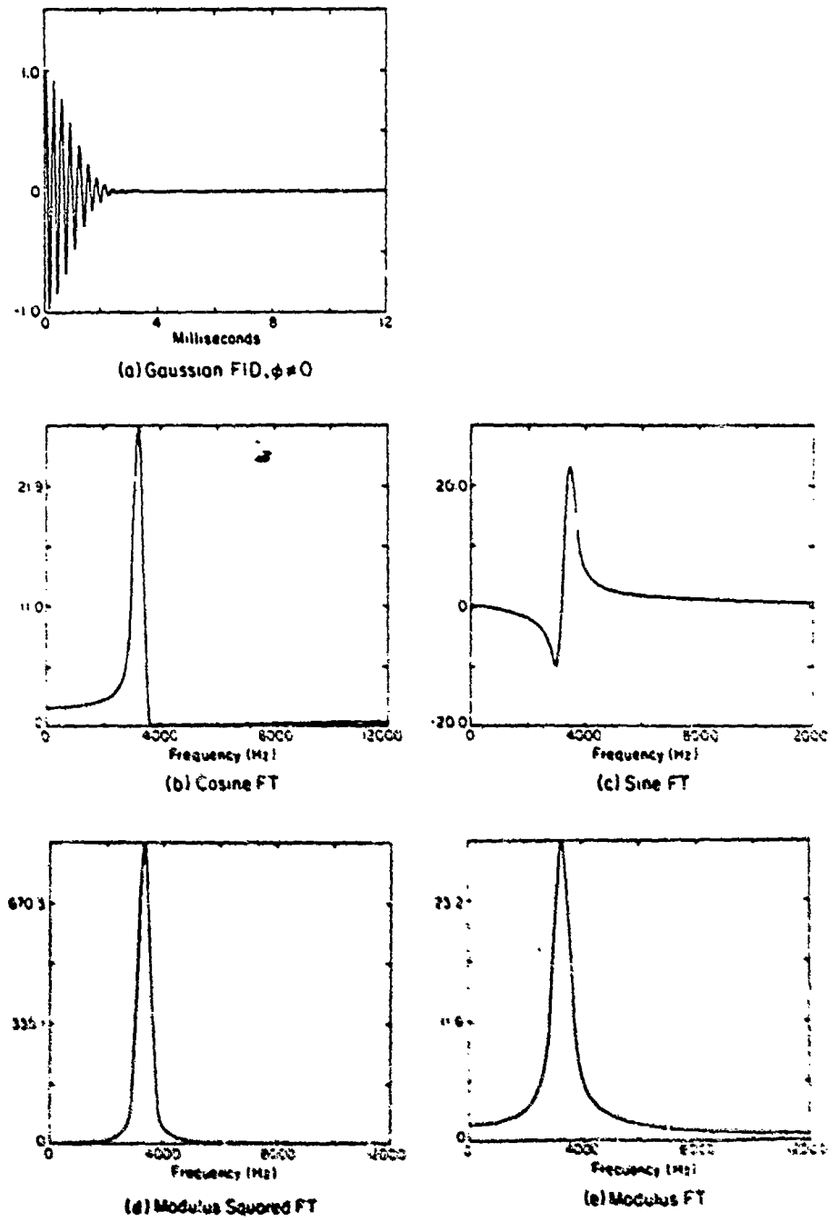

Figure 2.2-7. Computer-simulated Gaussian FID signal with phase shift (a) and its Fourier transforms (b-e). (a) time domain signal $[e^{-(\alpha t)^2}\cos(\omega t - \phi),\ t \geq 0]$; (b) Cosine FT of (a); (c) Sine FT; (d) modulus squared FT, $(C^2 + S^2)$ (e) modulus FT, $\sqrt{C^2 + S^2}$

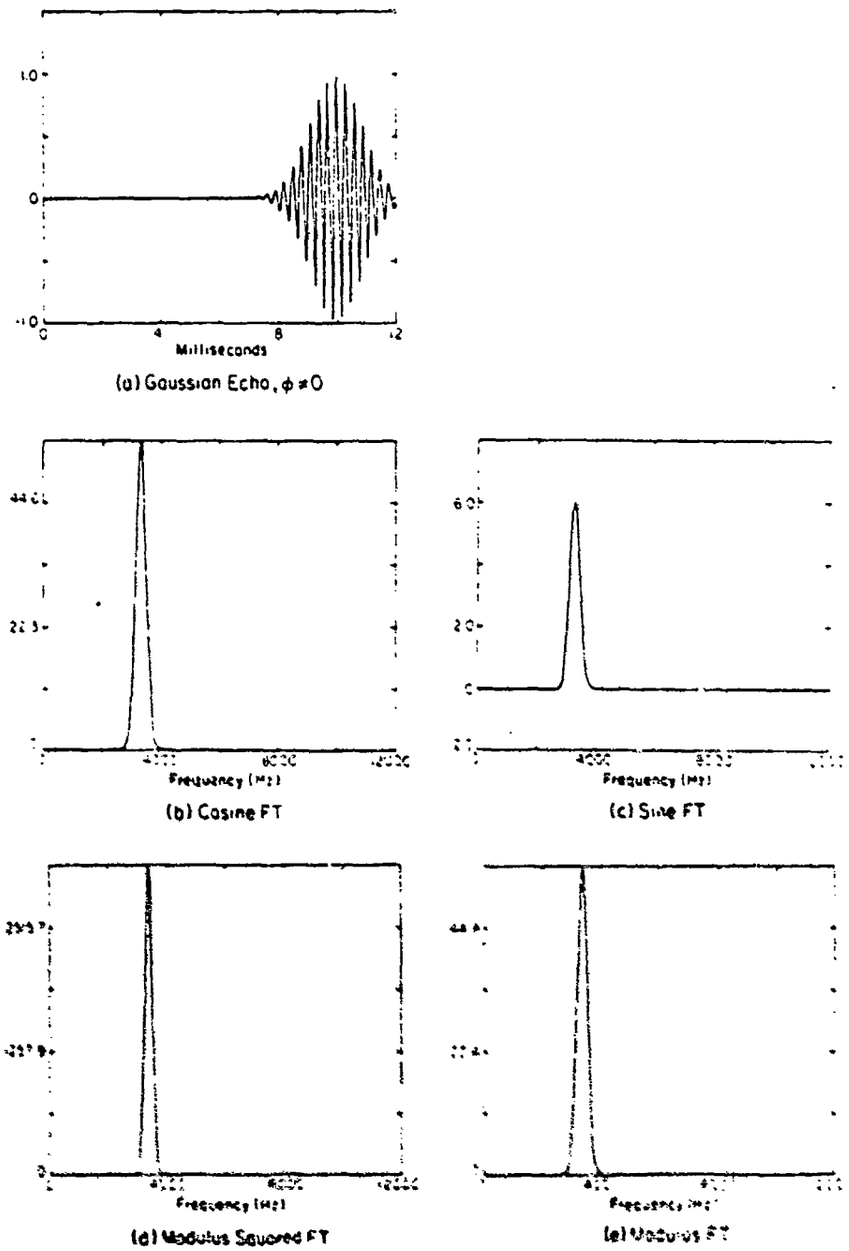

Figure 2.2-8. Computer-simulated Gaussian echo signal with phase shift (a) and its Fourier transforms. (a) time domain signal $[e^{-(\alpha t)^2}\cos(\omega t - \phi)]$; (b) Cosine FT of (a); (c) Sine FT; (d) modulus squared FT, (C^2+S^2) (e) modulus FT, $\sqrt{C^2+S^2}$

Figures 2.2-9, 2.2-10 and 2.2-11 show experimental spectra that demonstrate the foregoing arguments. Figures 2.2-9(a) and 2.2-10(a) are the Nitrogen-14 NQR FID signals at 77°K from hexamethylenetetramine (HMT) and urea, respectively. The Cosine and Sine transforms of HMT, Figures 2.2-9(b) and (c), clearly show the admixture of absorption and dispersion expected when phase shifts exist in the time-domain data. This effect is much less evident in the cosine and sine transforms of urea, Figures 2.2-10(b) and (c), which occured with only a small phase shift. Finally, the proper lineshapes are shown in Figures 2.2-9(d) and 2.2-10(d), the modulus squared transforms of the time-domain signals. Note the fine structure on the HMT line, first reported by Colligiani and Ambrosetti.[18] The modulus transforms, Figures 2.2-9 (e) and 2.2-10 (e), are shown for comparison and they are visibly broader than the true lineshapes.

An example of an echo signal is shown in Figure 2.2-11, a doublet of ν_- lines from the monoclinic phase of TNT at 77°K. Figures 2.2-11(b) and (c) are, respectively, the Cosine and Sine transforms of this signal. Note that, as expected, both of these transforms yield valid lineshapes with fractional amplitudes, and that the modulus transform, Figure 2.2-11 (e), yields the correct lineshape with maximum amplitude.

In Appendix B we collect a library of TNT lineshapes. In each case the time-domain echo signal is shown at the top of each figure, and the modulus Fourier transform, i.e., the lineshape, is shown at the bottom of the figure.

BLOCK ENGINEERING

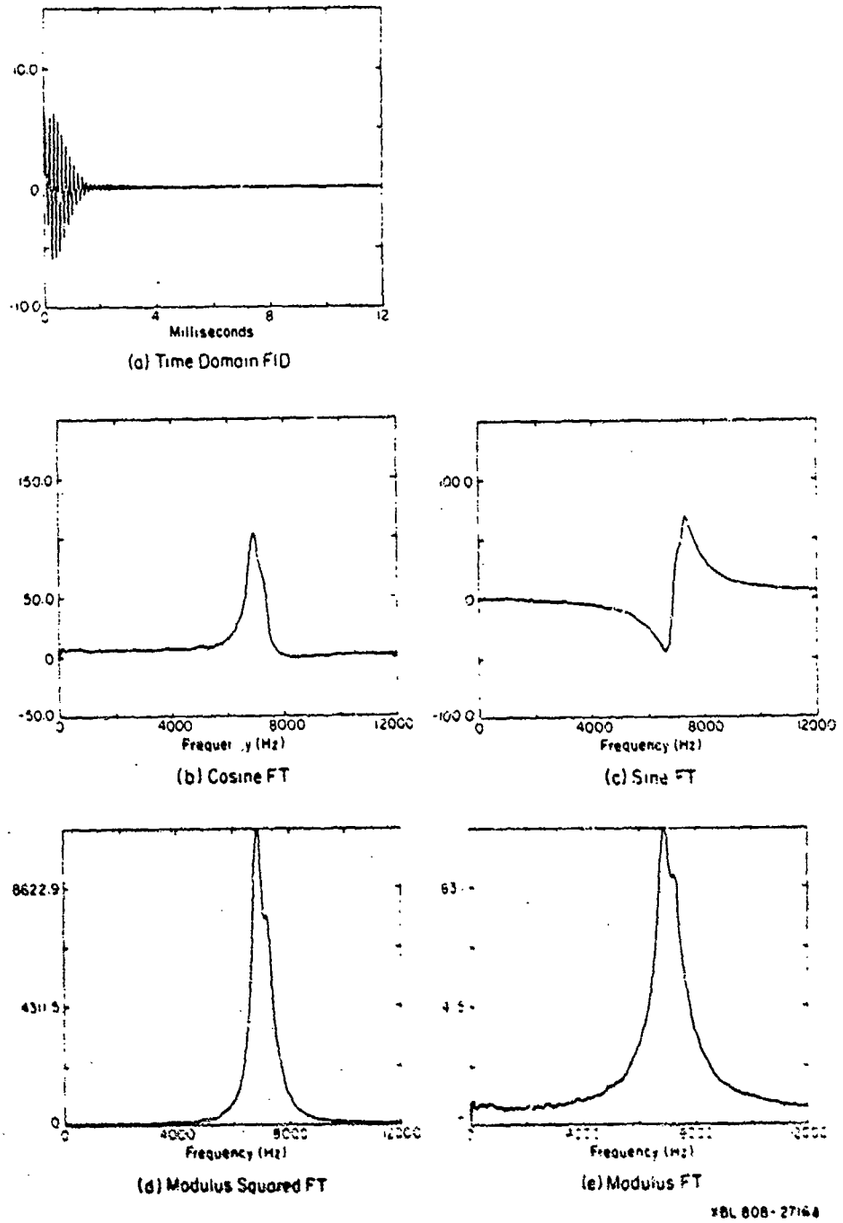

Figure 2.2-9 Experimental N^{14} FID signal from hexamethylenetetramine (HMT) at room temperature (a) and its Fourier transforms (b - e). (a) time domain signal, (b) Cosine FT of (a); (c) Sine FT; (d) modulus squared (C^2+S^2) (e) modulus FT, $\sqrt{C^2+S^2}$

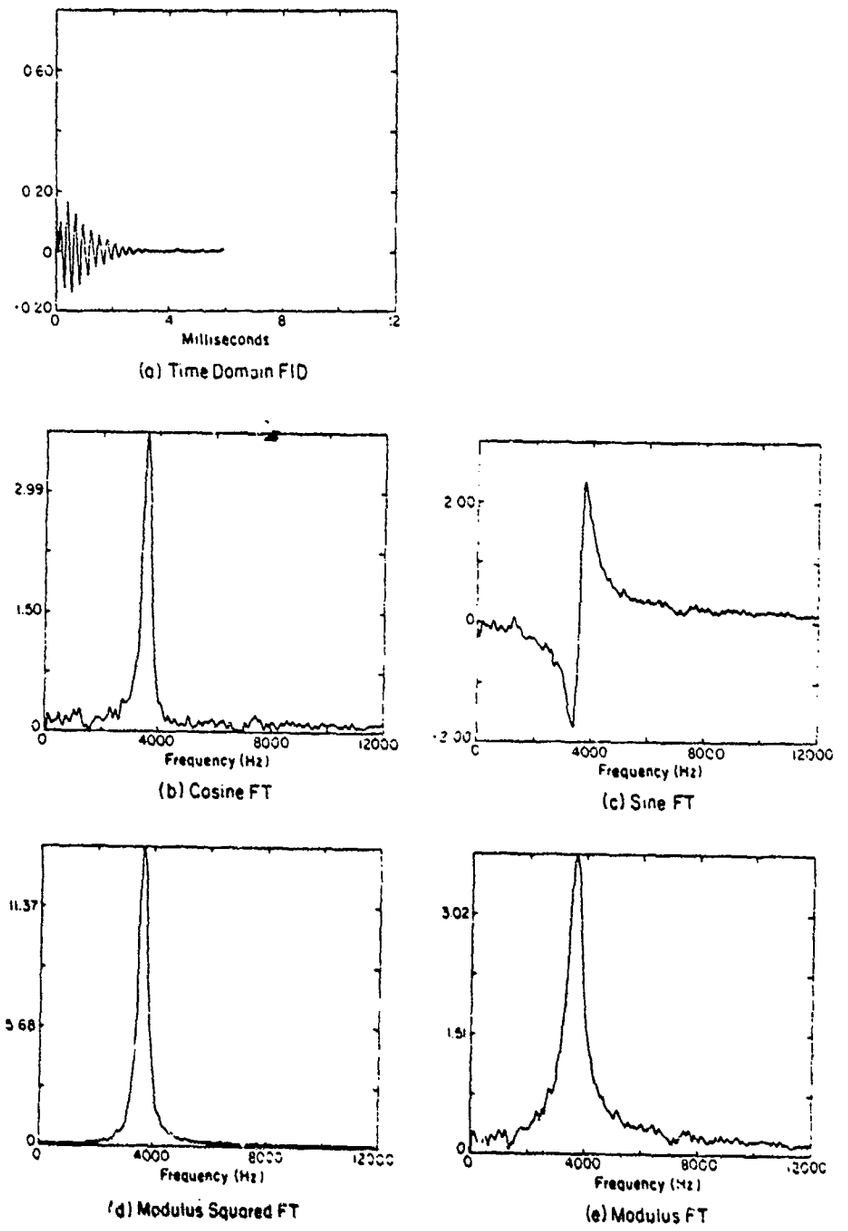

Figure 2.2-10. Experimental N^{14} FID signal from the ν_+ line in urea at 77°K a and its Fourier transforms (b-e). (a) time domain signal, b) Cosine FT of (a); (c) Sine FT; (d) modulus squared FT, (C^2+S^2) (e) modulus FT, $\sqrt{C^2+S^2}$

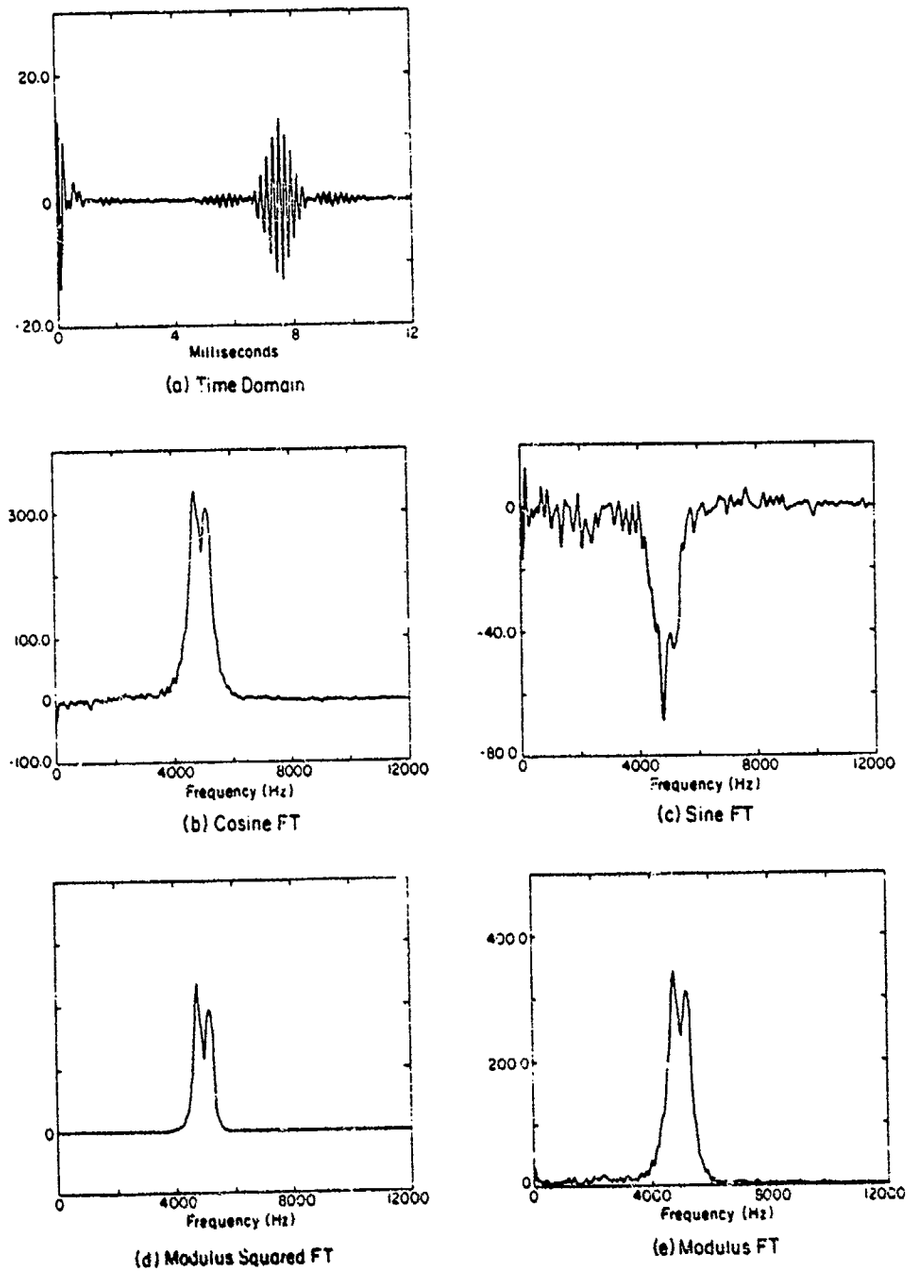

Figure 2.2-11 Experimental N^{14} spin echo signal from the 727 kHz ν_- doublet in monoclinic TNT at 77°K (a) and its Fourier transforms (b - e). (a) time domain signal, (b) Cosine FT of (a); (c) Sine FT; (d) modulus squared FT, (C^2+S^2) (e) modulus FT, $\sqrt{C^2+S^2}$

2.2.1 Broadband Fourier Transform Techniques for Nitrogen-14 NQR

In the last section it was pointed out that unlike the case of high-resolution nuclear magnetic resonance (NMR) it is not generally possible for a single Fourier transform (FT) to display a complete NQR Fourier transform (FT). In fact, typical Nitrogen-14 NQR Fourier transforms (FT) span only a few kHz. For examples, see Appendix B. There are several reasons for this restriction:

A. RECEIVER BANDWIDTH

In order to maximize the signal-to-noise ratio (S/N), the receiver bandwidth is kept low, typically not much larger than 10 kHz. In any event, the cut-off frequency must not be higher than half the frequency of the analog-to-digital converter of the signal averager used.

B. SAMPLE COIL QUALITY FACTOR

High values of the sample coil quality factor, Q, are used to maximize the S/N. The half-width at half-maximum of the receiver coil is given by $\Delta f = f_o/Q$. Thus, typical values of the transmitter frequency f_o = 1 MHz and Q = 100 yield Δf = 10 kHz. Thus we see that under these conditions the sample coil, quality factor introduces considerable distortions for Fourier transforms that extend much beyond 20 kHz.

BLOCK ENGINEERING

C. TRANSMITTER PULSE SHAPE FUNCTIONS

The spectral intensity of rectangular transmitter pulses of duration, t, and carrier RF frequency, $f_o = \omega_o/2\pi$, varies with frequency as $(\pi\Delta ft)^{-1} \sin(\pi\Delta ft)$, where Δf is the frequency offset from f_o. Thus, there is no transmitter power whatever at the first zero of this function, i.e., at a frequency of $\Delta f = 1/t$ away from the carrier f_o. Thus, the width of an NQR spectrum ,D, that is to be evenly excited by one or more transmitter pulses should be small compared to 1/t. Remembering that the choice of pulse width is governed by the need to generate an optimum flip-angle (cf. Equation 2.1-1), these considerations place a rigid constraint on D. For our spectrometer[5], which is comparable to other designs in use in this respect, t $\approx$ 50 microseconds. Thus, one requires

$$D \ll 20 \text{ kHz}, \qquad (2.2.1\text{-}1)$$

which is clearly a very stringent requirement.

The above considerations, together with the fact that the typical NQR spectrum reported in the literature consists of only a few widely separated narrow lines, have resulted in FT/NQR spectral widths,D, of the order of 3 to 5 kHz. However, driven by a desire to display as much as possible of the crowded ^{14}N NQR spectrum of TNT (cf. Figure 3.1-1 in the next section,) we were led to a study of ways to broaden D. The following steps were taken,

a. The signal average analog-to-digital (A-D) converter speed was increased from 50 kHz to 200 kHz. This was accomplished by using a Princeton Applied Research PAR 4202 signal averager with a 9 bit, 200 kHz A-D converter and by designing and building a custom interface for the Digilab Data System NOVA minicomputer. (Details of this work are given in Appendix D).

BLOCK ENGINEERING

b. The spectrometer receiver output filters were changed to allow the choice of a 100 kHz low pass filter.

c. The sample coil Q was lowered to a value of 24 by adding a series resistance to it.

d. Transmitter pulse widths were reduced to 10 microseconds. Because of finite rise and fall times, this value could not be reduced further.

These modifications allow spectra with width D ≈ 50 kHz in a single FT to be displayed, roughly an order of magnitude improvement over past practice. Signal averaging times needed to be sharply increased to make up for the degraded signal to noise ratios resulting from the choices made in "a"- "d" above. In order to minimize distortion of the computed broadband spectrum the transmitter pulse RF carrier, f_o, was placed at the edge of the desired spectrum, D, while the receiver and the sample tank circuit were tuned to the middle of D. The spectrometer was designed[5] to have a low value of Q, about 10, during the transmitter pulse. Therefore, placing f_o at the edge of D, the position of choice to obtain the true spectrum in the absence of quadrature detection poses no significant danger of distortion due to the sample coil Q.

Figure 2.2.1-1 shows our result for monoclinic TNT at 77°K. All six ν_+ lines are contained in a single interferogram, which is itself shown at the top of the figure. The final signal was obtained by the coherent addition of 600,000 echoes as follows: a SLSE train was generated with 100 echoes at 10 millisecond separation each. The spin system was allowed to approach thermal equilibrium with the lattice for 3 seconds, and the process repeated 6,000 times. The total observation time was 6.7 hours. The transmitter frequency and, therefore, also the origin of the FT is at 855.5 kHz. The receiver was tuned to 874.0 kHz.

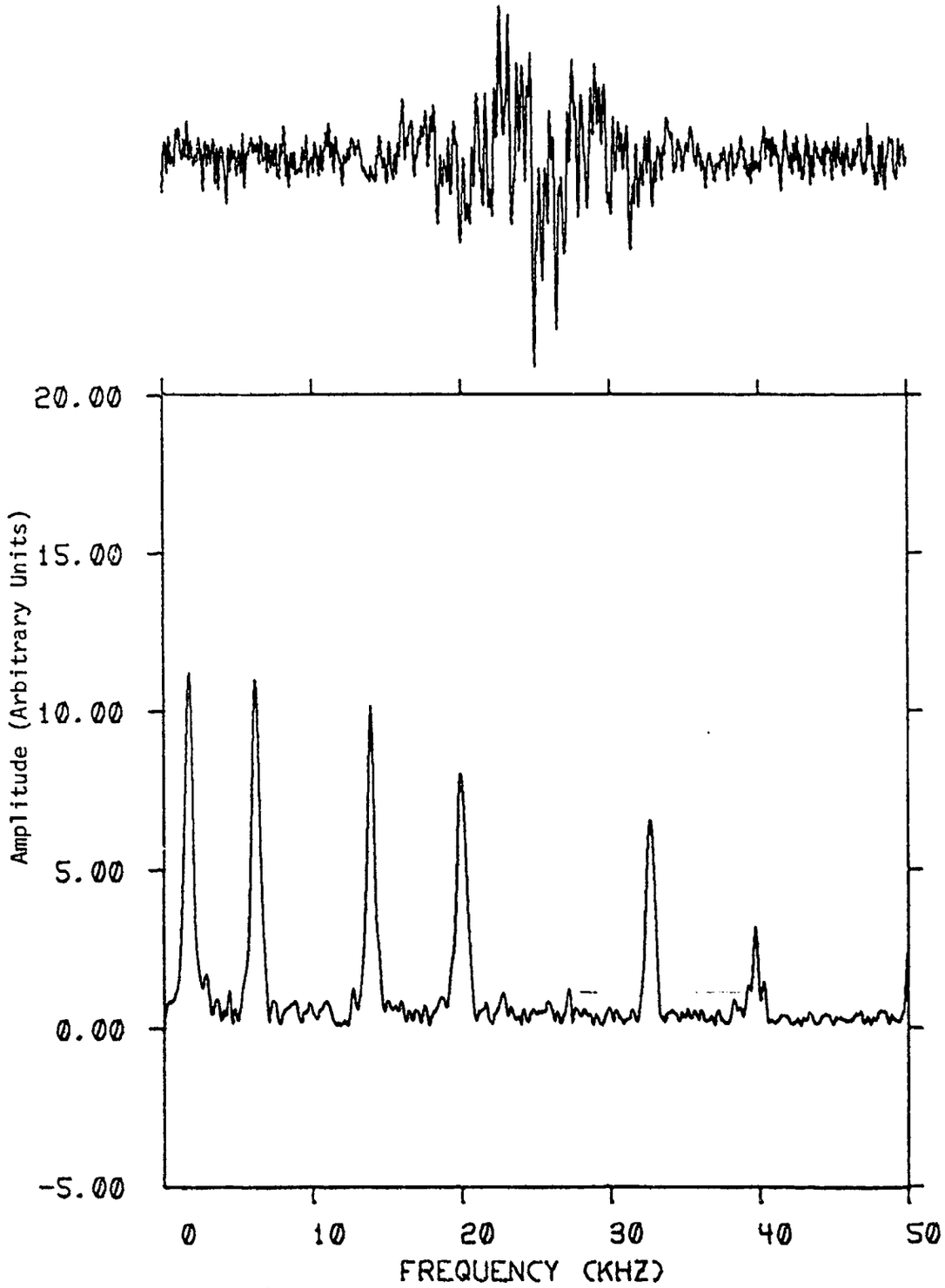

9-14/4 MONO.DT 855.5KHZ R@874.0 77K RATE 10

Figure 2.2.1-1 Echo signal interferogram and its broadband Fourier transform showing all six ν_+ lines of monoclinic TNT at 77°K. Other parameters are given in the text.

Various corrections can be made to the raw data shown in Figure 2.2.1-1 in an attempt to improve the considerable distortion still seen there, exemplified by the decreasing amplitude of peaks with increasing frequency offset. We list some possible remedies,

a. correct for sample coil Q function

b. correct for the receiver filter characteristics

c. correct for the transmitter pulse spectral intensity variations

d. correct for the transmitter pulse non-ideality, e.g., the phase shifts introduced by finite rise and fall times.

e. correct for the fact that the intensity of an interferogram signal obtained from the coherent sum of a train of echoes in a SLSE sequence is a function of the relaxation times of the individual resonances and not merely a reflection of a density-of-states function.

In Figure 2.2.1-2 we show the same TNT spectrum of the previous figure corrected only for a. and b. above. A slight improvement is observed. (N.B., the sharp feature exactly at 50.0 kHz is a spurious "electronic resonance" and is <u>not</u> sample dependent). The correction function was obtained experimentally by measuring the response of the coil and receiver combination in a separate procedure. The resulting normalizing function is shown as Figure 2.2.1-3.

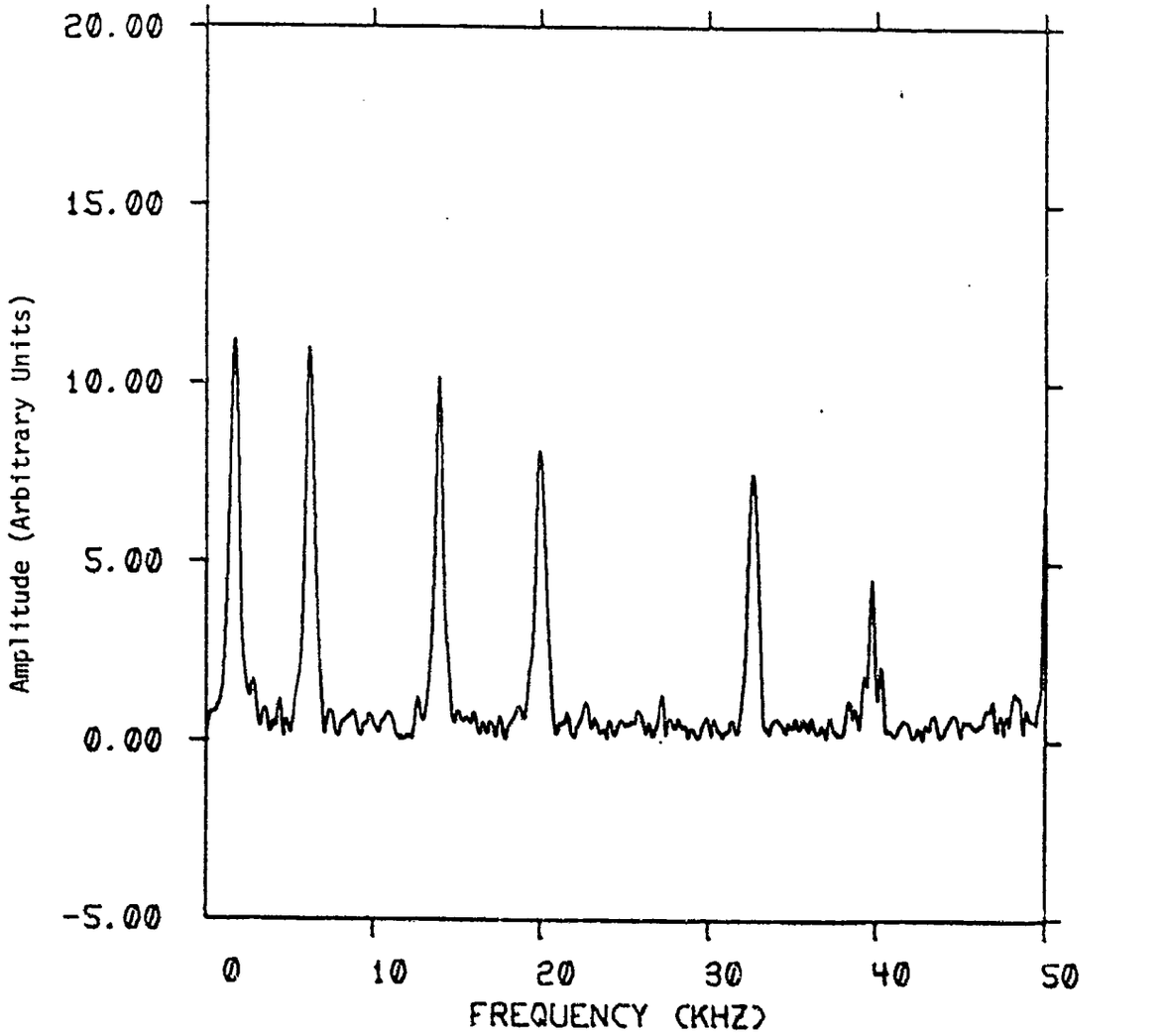

9-14/4 NORMALIZED MONO.DT 855.5KHZ R@874.0 77K RATE 10

Figure 2.2.1-2 Normalized spectrum of ν_4 lines of monoclinic TNT at 77°K.

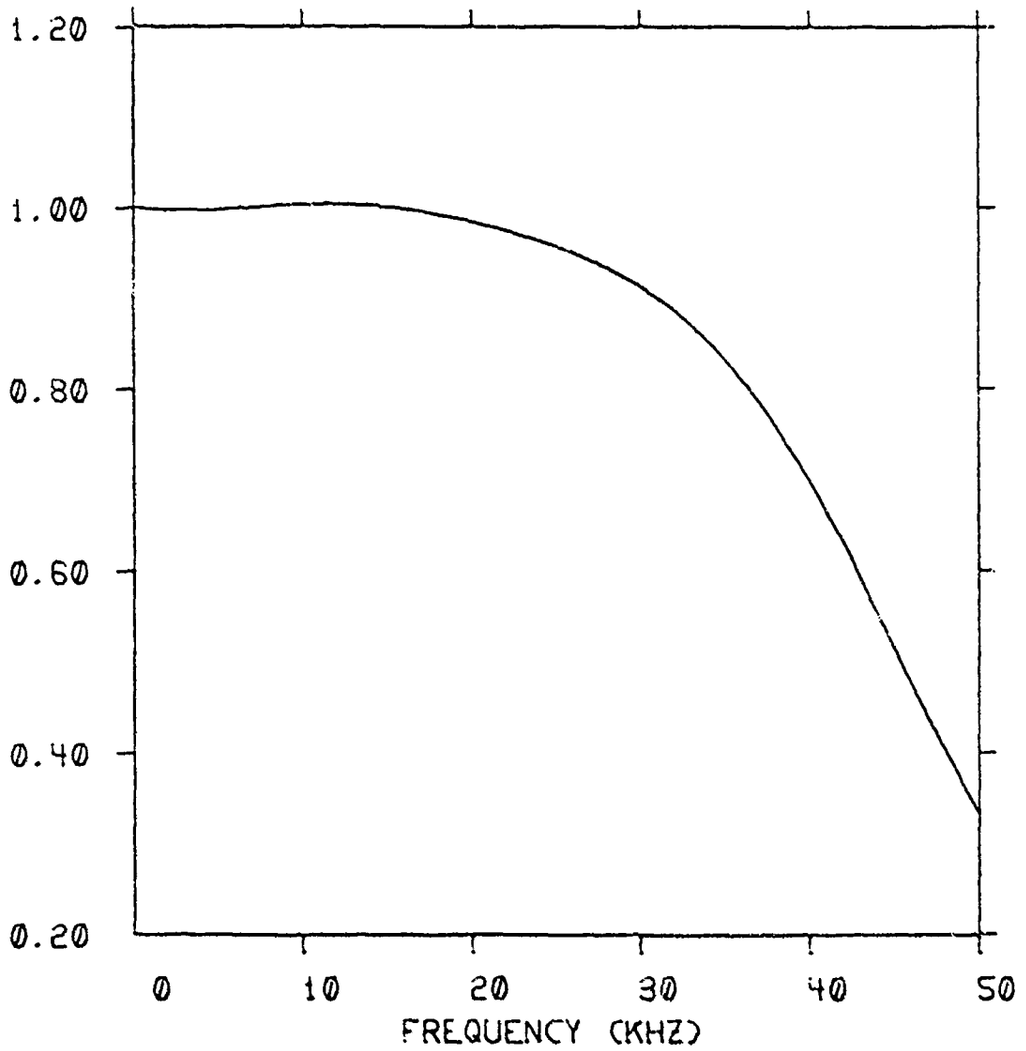

XMONO.DT

Figure 2.2.1-3 Normalizing function for Broadband FT of TNT which was used to obtain Figure 2.2-2 from Figure 2.2-1.

One of the benefits of being able to display a larger spectrum D, is that it enables us to study effects that occur in this larger domain. An obvious case is the situation of the need to study NQR lines that are themselves intrinsically broad in frequency space. An example is the hydrogen bonded crystal Hexamethylenetetramine Hexahydrate which has three NQR lines labelled ν_+, ν_-, and ν_o broaded by positionally disordered protons in the structure. The broadband FT spectra of these lines are shown in Appendix C.

2.3 TEMPERATURE DEPENDENCE

Two methods were used to determine the frequency/temperature dependence of the TNT NQR lines.

The first method of temperature control is shown in Figure 2.3-1a, the temperature stabilization assembly. This assembly with the circuitry shown in Figure 2.3-2, was able to control the temperature to ±0.1°C between 140°K and 320°K. For temperatures reasonably above ambient, the liquid nitrogen ballast is not needed.

BLOCK ENGINEERING

REVISIONS			
LTR	DESCRIPTION	DATE	APPROVED

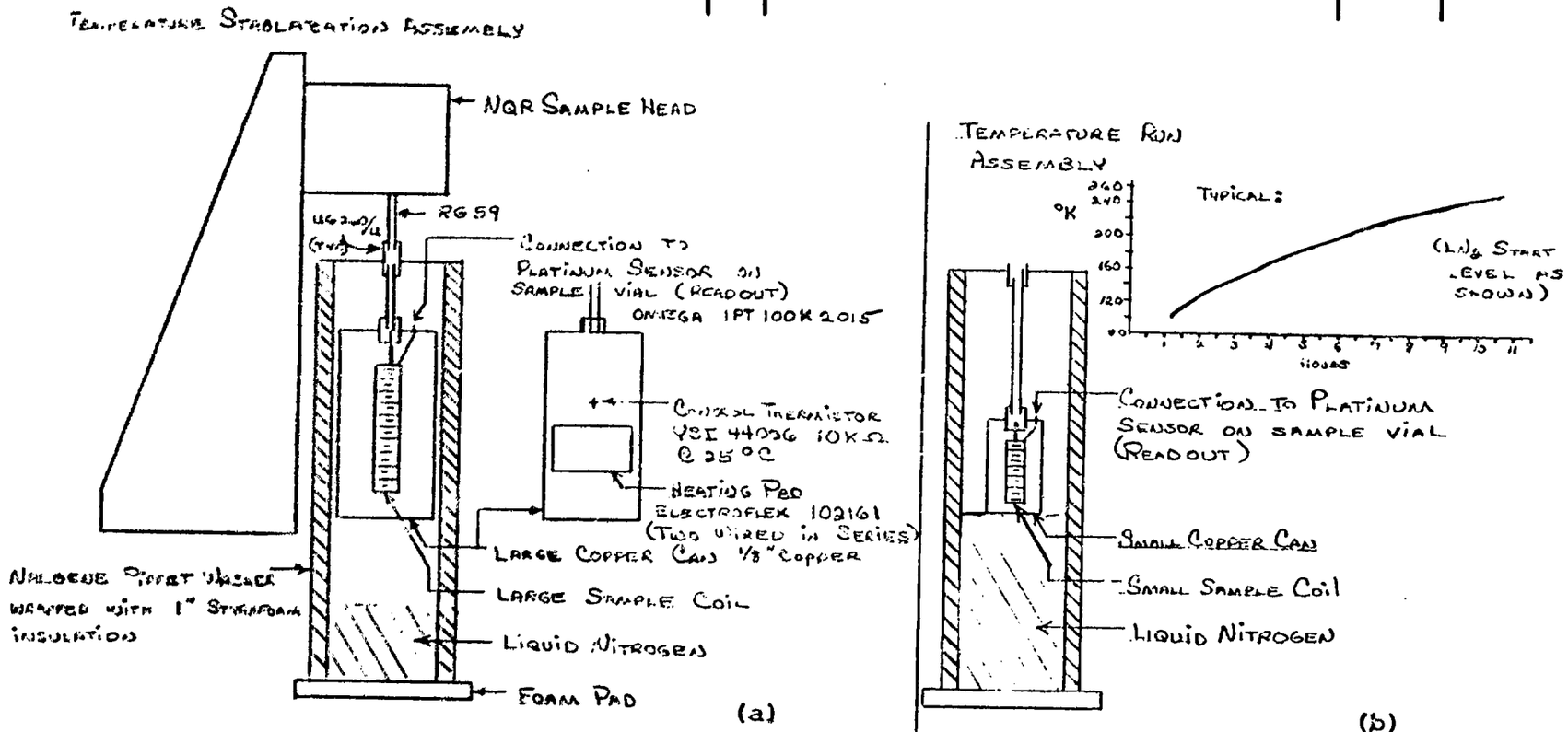

Figure 2.3-1 NQR Temperature Run Assemblies

NEXT ASSY	USED ON
APPLICATION	

LIST OF MATERIALS

UNLESS OTHERWISE SPECIFIED DIMENSIONS ARE IN INCHES
TOLERANCES
FRACTIONS ± 1/64
ANGLES ± 0° - 15'
DECIMALS 2 ± .030, 3 ± .010, 4 ± .005
FINISH MAXIMUM
REMOVE ALL BURRS & SHARP EDGES
DO NOT SCALE THIS DRAWING
MATERIAL
FINISH

DRAWN		DATE
CHECKED		
APPROVED		
APPROVED		
ISSUED		

BLOCK ENGINEERING, INC
CAMBRIDGE, MASSACHUSETTS 02139

NQR TEMPERATURE RUN ASSEMBLIES

SIZE	CODE IDENT NO.	DRAWING NO.	REV.
A	21351	611104	

SCALE 1/10 SHEET 1 OF 1

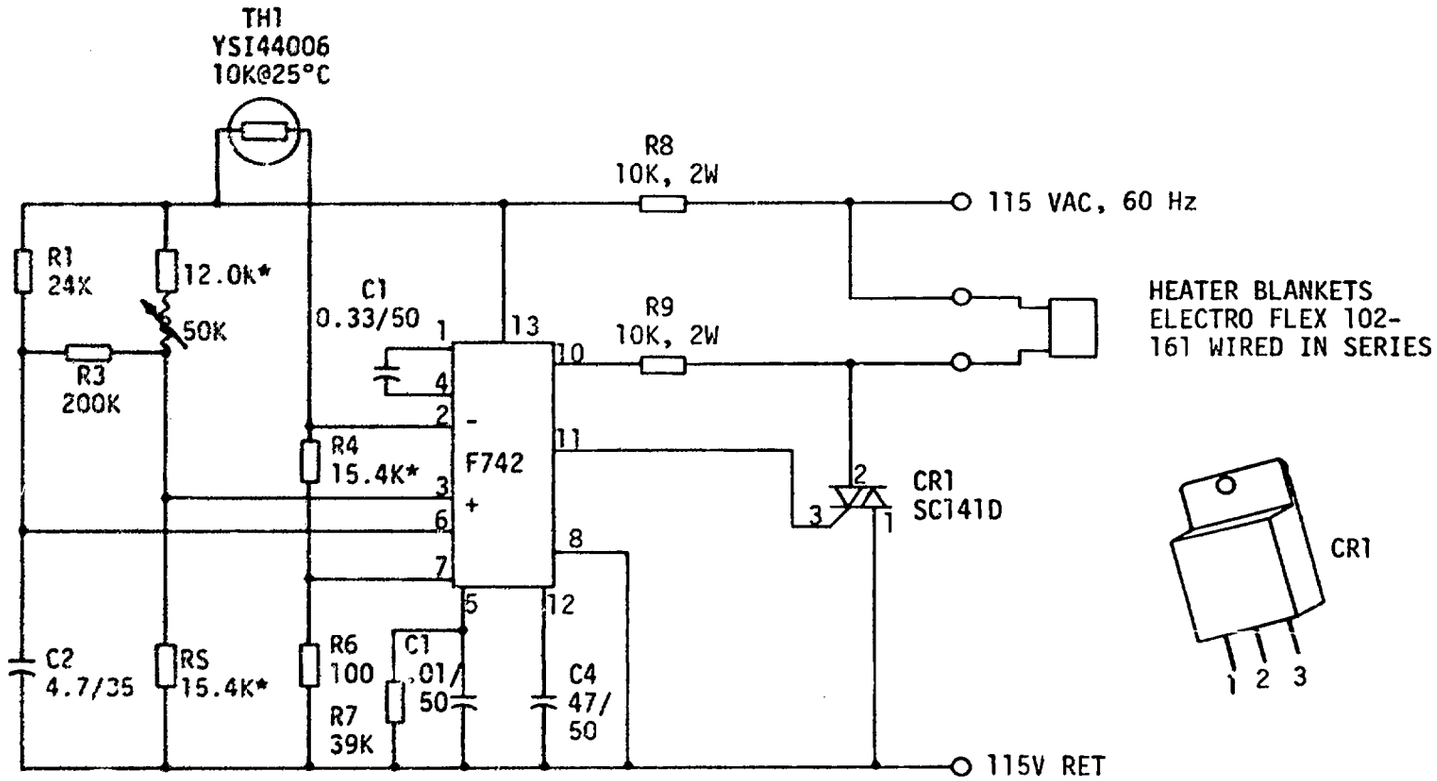

NOTES:

UNLESS OTHERWISE SPECIFIED

1. RESISTORS ARE IN OHMS, ±5%, ½ WATT
2. CAPACITORS IN IN f/RATED VOLTAGE
3. * INDICATES METAL FILM RESISTOR, ±1%
4. LAST REFERENCE DESIGNATIONS USED ARE: R9, C4, TH1, CR1

Figure 2.3-2. Temperature Controller

The temperature control circuitry proportionally controls, and turns "on" only during a zero crossing of the AC signal to minimize RF interference.* No crosstalk into the instrument was observed.

The Nalgene® pipet washer did fairly well holding liquid nitrogen. It is necessary to fill it somewhat slowly in order to minimize the thermal shock.

A second, cruder, method was also used in the initial runs. This was a brute force approach of cooling the sample to 77°K via liquid nitrogen, and following the frequencies as the sample slowly warmed to room temperature in a Dewar. The apparatus used is shown in Figure 2.3-1b, the temperature run assembly. Also shown is a typical Temperature vs. time plot.

* Applications of the μA742 TRIGAC, A Zero Crossing AC Trigger by R.B. Hood, 1970 Fairchild Semiconductor 04-10-0063-50. 2nd printing.

®Registered trademark of the NALGE Corp.

2.4 A METHOD TO PAIR UP ν_- AND ν_+ LINES

In this section we outline a simple double resonance method of pairing up ν_+ and ν_- lines corresponding to the same NQR site. A uniform static magnetic field H_o is applied to the sample and a spin-locked spin echo (SLSE) experiment is performed. The spacing between pulses is chosen small enough that the echo train decay constant $T_{2\varepsilon}$ is appreciably longer than T_2. The individual echoes in the echo train are co-added to give a resultant signal whose magnitude is then plotted vs. the magnetic field H_o. For a unique value of H_o, the NMR splitting of protons in the neighborhood of the ^{14}N site exactly matches the ^{14}N "difference" line $\nu_o=\nu_+-\nu_-$. When this happens, mutual spin flips between the Proton and Nitrogen spin systems will result in lower values of the ^{14}N relaxation times T_2 and T_1. Since the inequality $T_1>T_{2\varepsilon}>T_2$, holds, the concomitant decrease in $T_{2\varepsilon}$ results in an often dramatic decrease in the value of the resultant co-added echo.

Figure 2.4-1 shows just such a plot of NQR echo height vs. the proton NMR frequency γH_o, where γ is the proton magnetogyric ratio. The NQR transition under study is the 811 kHz ν_- lines in m-dinitrobenzene. The sharp dip in the echo enabled the paring-up of this line with the previously detected ν_+ line at 1030 kHz.

BLOCK ENGINEERING

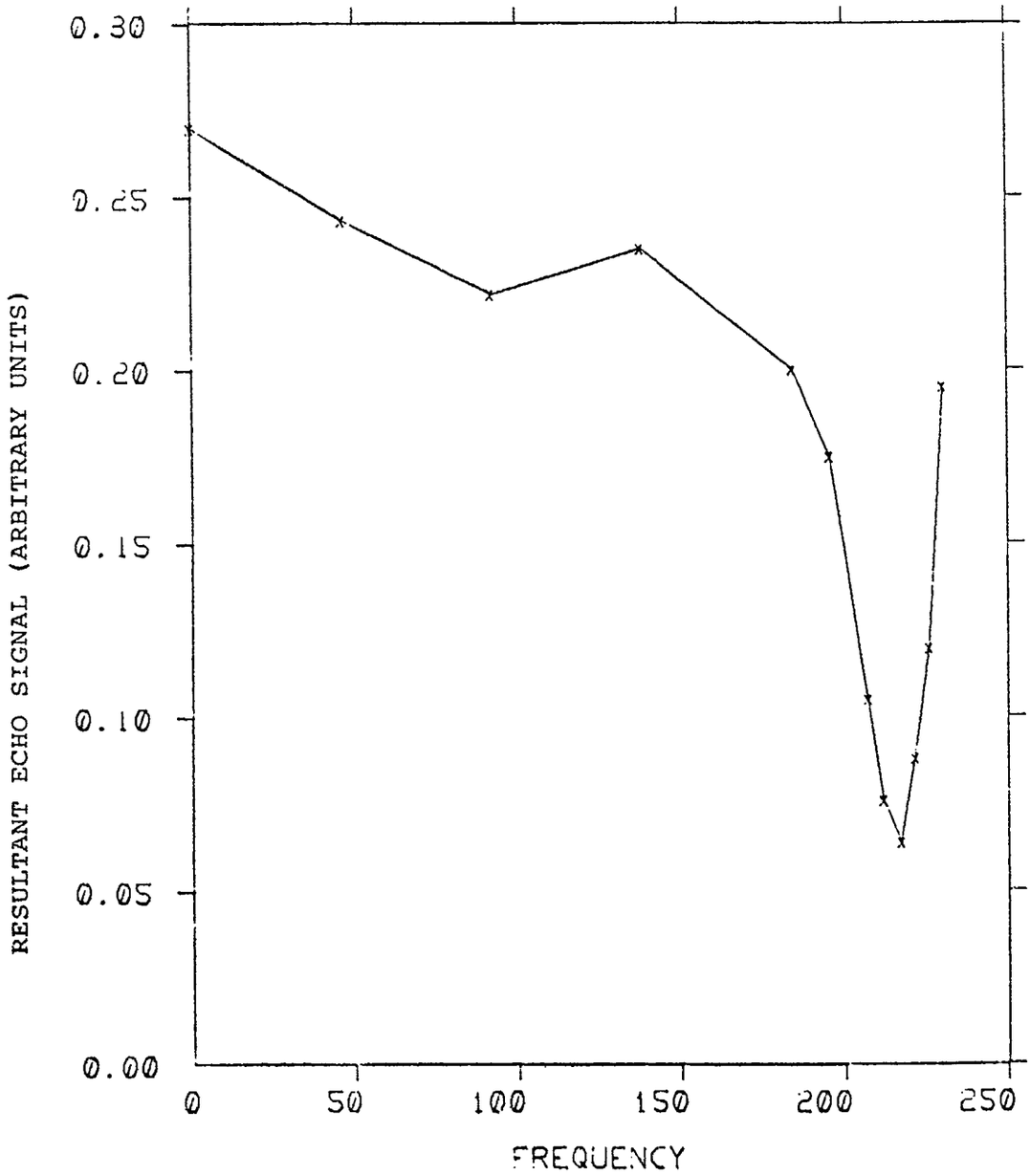

Figure 2.4-1. Plot of the amplitude resultant from coherently adding echoes in a single SLSE train vs. the applied static magnetic field expressed as the corresponding proton NMR resonance frequency. The NQR transition is the 811 kHz ν_- line of m-dinitrobenzene at 77°K.

BLOCK
ENGINEERING

3.0 NQR STUDY OF TNT

It has long been established that α-Trinitrotoluene can coexist[19,20] as two different phases at ambient temperatures. A monoclinic form is the product of annealing cast TNT and has been studied by several workers,[21,23] A crystal structure has only recently been obtained by J.R.C. Duke.[24] Another possible crystal habit has orthorhombic symmetry[23,25,27]. This phase can be formed by quickly chilling molten TNT as well as by recrystallization from cyclohexanol. We have recently become aware that a crystal structure of this phase also has been obtained by J.R.C. Duke[28].

Samples of cast TNT, which commonly contain a mixture of these two phases, will often develop cracks and voids when orthorhombic microcrystals transform to the denser monoclinic phase upon annealing. The desire to learn more about the molecular structure and molecular dynamics of TNT in the two phases provided part of the rationale for this study.

BLOCK ENGINEERING

3.1 SAMPLE PREPARATION AND NQR SPECTRUM

α-TNT obtained from Eastman Kodak arrives in the form of small flakes moist with 10% water. These flakes were gently dried under a heat lamp and recrystallized from acetone. The resulting very pale yellow crystals were used to prepare samples of solid TNT which were preferentially crystallized in one of its two crystal habits. Monoclinic TNT was obtained by seeding the melt[29,30,31] with about ½ of a percent of 2,2',4,4',6,6'--Hexanitrostylbene (HNS) allowing the complex $(TNT)_2 \cdot HNS$ to form and then to nucleate the growth of monoclinic TNT.

The resulting polycrystalline material consisted of a mass of unoriented and very small crystallites as expected. Orthorhombic TNT was prepared by quenching molten TNT in small batches on a copper slab maintained at about 0° C.

The ^{14}N NQR spectrum of monoclinic TNT and of orthorhombic TNT is shown in Figure 3.1-1. The spectrum of each phase consists of twelve resonance lines, corresponding to six distinct nitrogen sites. Each site gives rise to a ν_- and a corresponding ν_+ line (See Appendix A) which are related to the quadrupole coupling constant, e^2qQ/h , and to the asymmetry parameter, η, by the following equations:

$$e^2qQ/h = \frac{2}{3} \quad (\nu_+ + \nu_-)$$
$$\eta = 3 \quad \frac{(\nu_+ - \nu_-)}{(\nu_+ + \nu_-)} \qquad (3.0\text{-}1)$$

BLOCK ENGINEERING

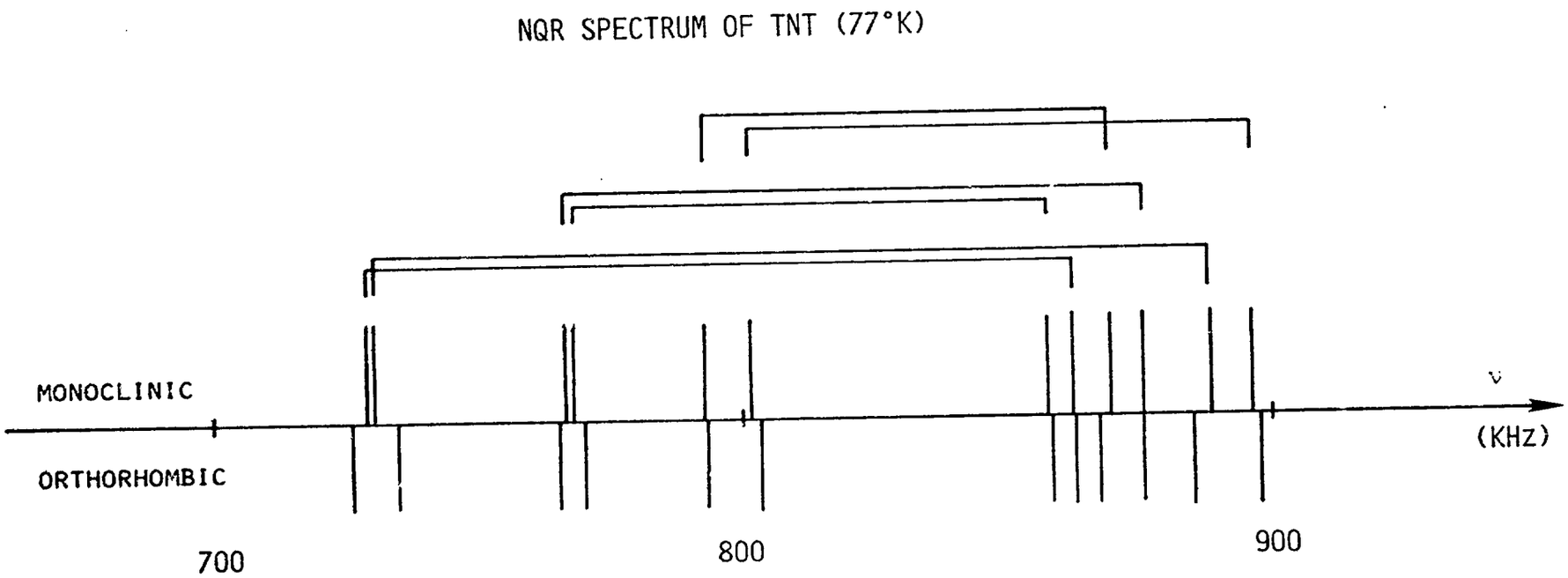

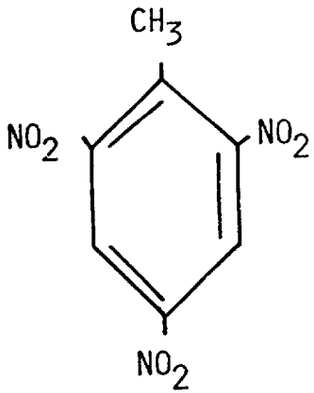

Figure 3.1-1. NQR Spectrum of TNT (77°K). Brackets indicate paired lines.

For each corresponding pair of ν_- and ν_+ lines there also exists a "difference line" ν_d whose value is given by $\nu_d = \nu_+ - \nu_-$. In TNT the frequencies of these transitions fall below the lower operating point of our spectrometer and were not detected. Therefore, in order to compute e^2qQ/h and η for each site it is necessary to "match-up" the corresponding ν_+ and ν_- lines. This was done using a simple double resonance technique described in Section 2.4. Table 3.1-I shows the NQR frequencies matched and assigned to six crystallographic sites for both phases of TNT.

The similarity between the NQR spectra of the two phases of TNT as depicted in Figure 3.1-1 is remarkable. Experience with NQR spectra of other subtances which undergo structural phase transition shows that the NQR frequencies undergo shifts of the order of 10%. Now, these structural phase transition shifts have been interpreted as giving a measure of the contribution of atoms and molecules other than those directly bonded to the resonant site to the total field gradient at that site. An independent measurement of the same effect is the size of "crystal splitting", the difference in NQR frequencies corresponding to sites that are chemically equivalent, but which are made physically inequivalent by the crystal packing. These two measures of crystal field effects have been found generally in good agreement when they could be compared.

In the present case, we observe that the spectra of orthorhombic and monoclinic TNT are nearly identical to one another while at the same time each phase displays considerable physical inequivalence (See Section 3-2). This allows us to conclude with some confidence that the structure and conformation of each molecule in <u>orthorhombic TNT</u> and its relation to its immediate molecular neighbors must be remarkably similar to the case in <u>monoclinic TNT</u>.

BLOCK
ENGINEERING

TABLE 3.1-I

Nitrogen-14 NQR Spectra of Trinitrotoluene at 77°K. The spectral lines are assigned to one para (p) site and two ortho sites (oA,oB) for each of two inequivalent molecules (I and II). Data for the monoclinic phase are listed first, with corresponding lines of the orthorhombic phase shown in parentheses.

MOLECULAR SITE	ν_- kHz	ν_+ kHz
oAI	792.1 (792.4)	869.4 (867.8)
oAII	801.8 (803.2)	895.4 (897.9)
oBI	767.3 (766.5)	875.6 (875.7)
oBII	767.7 (768.5)	857.0 (858.6)
pI	729.7 (727.4)	861.8 (862.3)
pII	730.1 (732.5)	888.1 (885.6)

BLOCK ENGINEERING

Because of this great similarity, our discussion of structure and bonding of α-TNT will focus specifically on the temperature stable (monoclinic) phase of this material.

3.2 Structure and Bonding of TNT - General

For each crystal phase of TNT the observation of six ν_- lines and six ν_+ lines, indicating the presence of six Nitrogen NQR sites is in agreement with the x-ray crystallography work of J.R.C. Duke[24,28]. There are two crystallographically distinct molecules per unit cell, each with physically inequivalent nitro-groups. Figures 3.2-1 and 3.2-2 shows Duke's results for the molecular and crystal structure for the two phases of TNT.

The isolated molecule of trinitrotoluene (2-methyl-1,3,5-trinitrobenezene) has two chemically distinct nitro-groups which we could designate p and o for the groups which are para and ortho, respectively, to the methyl group. If the two ortho sites become physically inequivalent in the solid, and we label them oA and oB respectively, and if we now label the two crystallographically distinct molecules per unit cell I and II, we reach a nomenclature for the six sites which we will use for the remainder of this report. Namely, pI, oAI and oBI for molecule I, and pII, oAII and oBII for molecule II.

BLOCK ENGINEERING

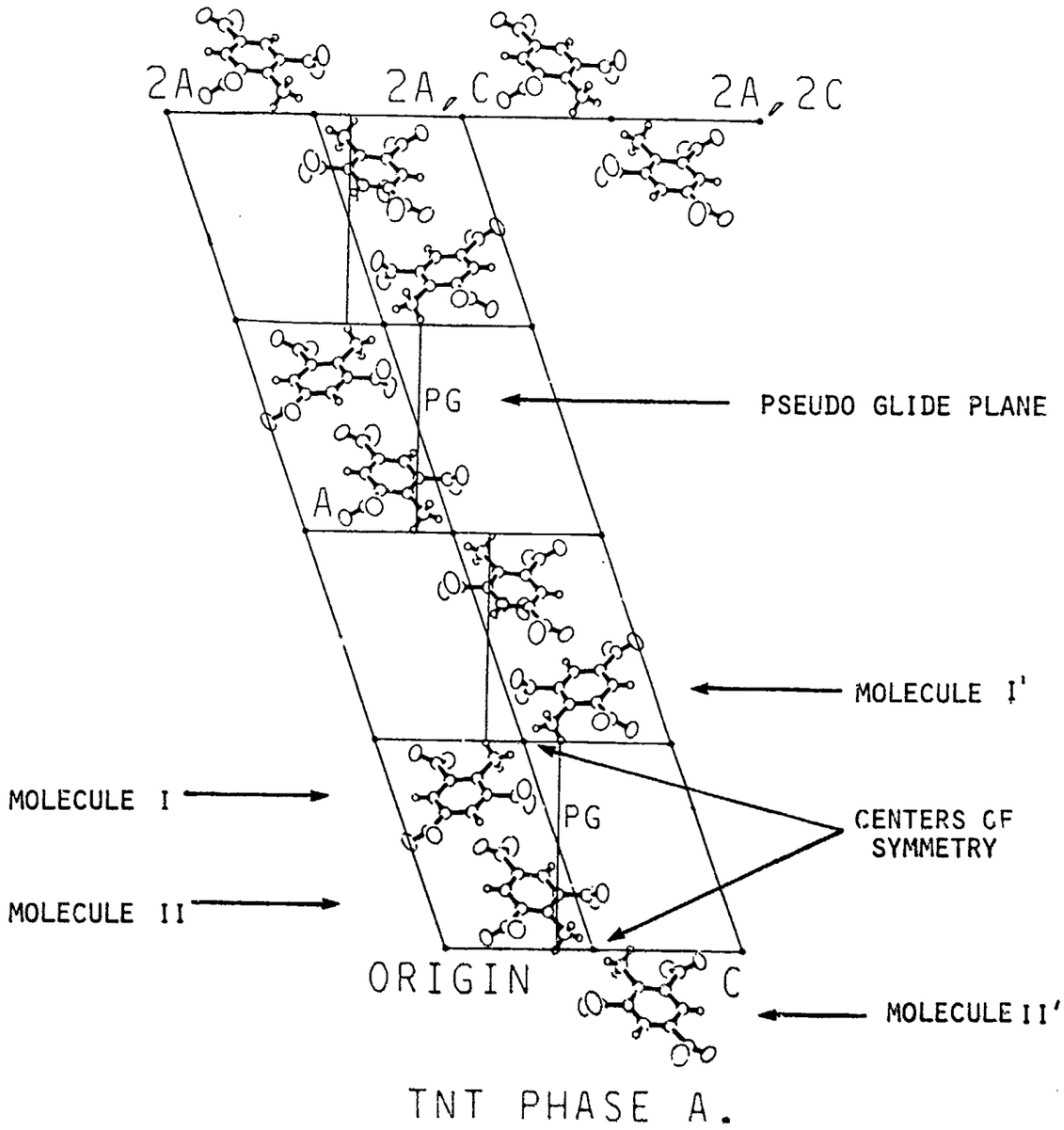

Figure 3.2-1. Projection of the crystal and molecular structure of MONOCLINIC TNT on the a-c crystal plane. Data and figure obtained from J.R.C. Duke (private communication, 1982).

BLOCK ENGINEERING

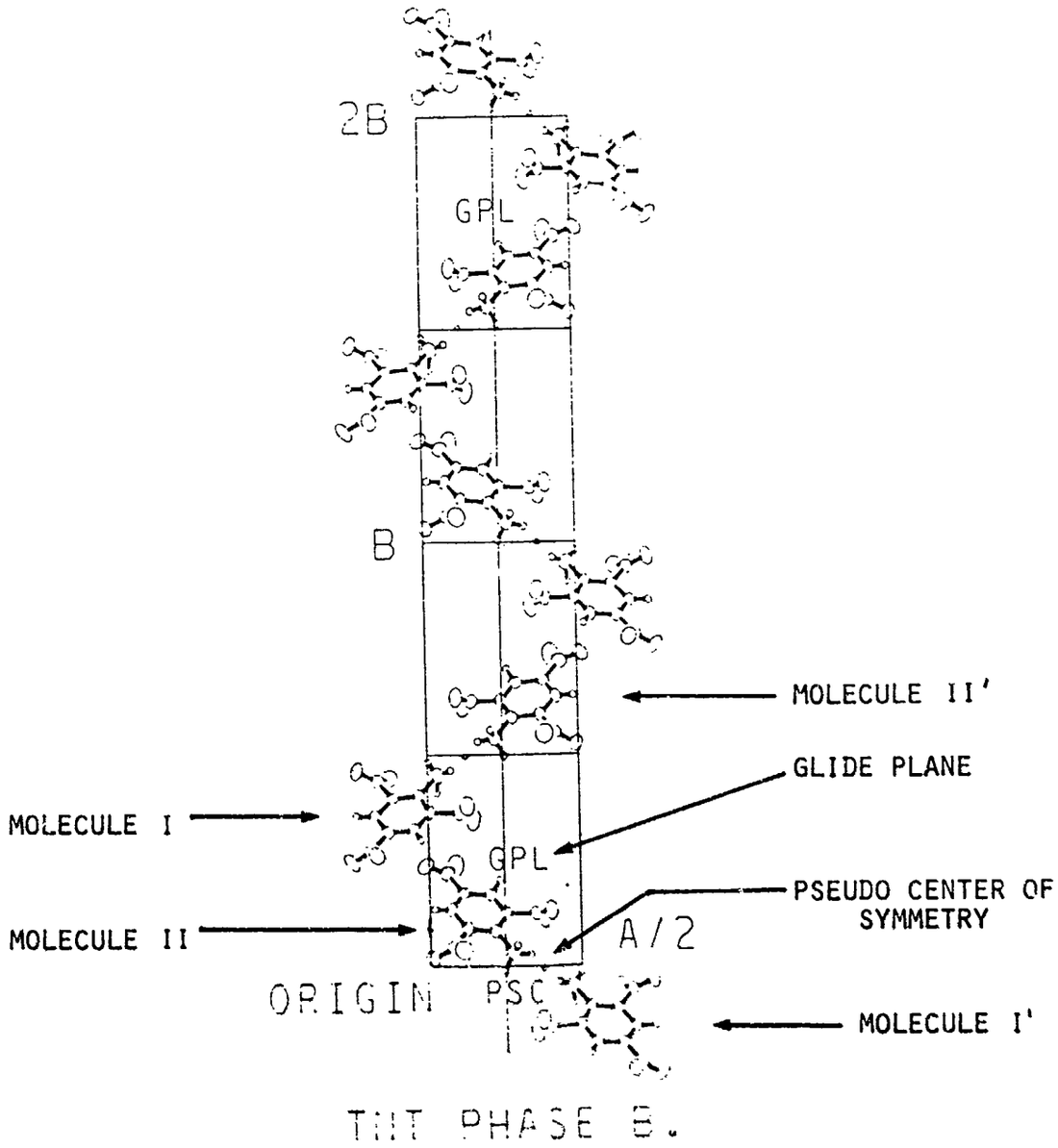

Figure 3.2-2. Projection of the crystal and molecular structure of ORTHORHOMBIC TNT on b-c crystal plane. Data and figure obtained by J.R.C. Duke (private communication, 1982)

BLOCK ENGINEERING

The above considerations about the chemical and physical (in)equivalence of NQR sites is usually extremely useful in comparing these sites to their corresponding crystallographic sites. However, this is not the case in TNT as can be seen by the seemingly incongruous pairing of ν_- and ν_+ lines in Figure 3.1-1. In fact, it will be shown that the chemical inequivalence of "o" and "p" sites are not basically relevant to the interpretation of NQR spectrum of Figure 3.1-1. Rather, the determining factc in explaining the splitting of the NQR lines is the physical inequivalence of the six nitrogen sites in the solid state. Specifically, we will show that the parameter that makes the dominant contribution is the angle of twist of the nitro-group about the C-N bond.

In the following sections, we will first develop a set of equations (Townes-Dailey method) relating the observed NQR parameters to a bonding model of the nitro-group. Then we will use these equations to interpret the TNT data, and show how additional NQR data, much of it new, on molecules similar to TNT supports our interpretation.

3.2.1 Structure and Bonding of TNT:Townes-Dailey Theory

The Townes-Dailey (TD) method[32] of relating measured field gradients to orbital occupation numbers is a first-order theory which works best when comparisons are made among similar molecules[33]. In our case, where we limit our discussion to C-nitro groups, we expect that the analysis will provide useful insights in the variation of structure and electron distribution among the various nitro groups under study.

Figure 3.2.1-1 depicts the coordinate system which is used to analyze the bonding of the nitro group. Because two of the axes are perpendicular to local mirror planes, one is assured that the chosen axes will diagonalize the electric field gradient due to the local electron distribution. The axes are labelled using the convention independently arrived at by Subbarao and Bray[34], and by Cheng and Brown[35]. The nitrogen site is assumed to be in a state of sp^2 hybridization: a sigma bonding orbital of occupation number σ_{NC} forms a bond to the ring carbon atom, while the two remaining hybrids, each with occupation number σ_{NO}, form sigma bonds to the oxygen atoms. A nitrogen p_y orbital, with occupation number π, takes part in the molecular $p\pi$ orbitals. Table 3.2.1-I lists the nitrogen hybrid orbitals and their occupation numbers. The standard sp^2 hybridization is used in these equations even though the angle $\widehat{ONO}$ is known to be larger than 120° by about four to five degrees. Although the TD method can easily accommodate this "refinement" it has been the experience of this and other workers that it does not result in a significant improvement of the final results.

Using the orbitals of Table 3.2.1-I, the Townes-Dailey relations can be written in the following very useful form,

$$\nu_+/q_o = \frac{3}{4}\,(\pi - \sigma_{NO}) \qquad (3.2\text{-}1a)$$

$$\nu_-/q_o = \frac{1}{2}\,(\sigma_{NC} - \sigma_{NO}) \qquad (3.2\text{-}1b)$$

or equivalently as,

$$(\pi - \sigma_{NO}) = \frac{4}{3}\,\nu_+/q_o \qquad (3.2\text{-}2a)$$

$$(\sigma_{NC} - \sigma_{NO}) = 2\,\nu_-/q_o \qquad (3.2\text{-}2b)$$

$$(\sigma_{NC} - \pi) = (2\nu_- - \frac{4}{3}\,\nu_+)/q_o \qquad (3.2\text{-}2c)$$

BLOCK ENGINEERING

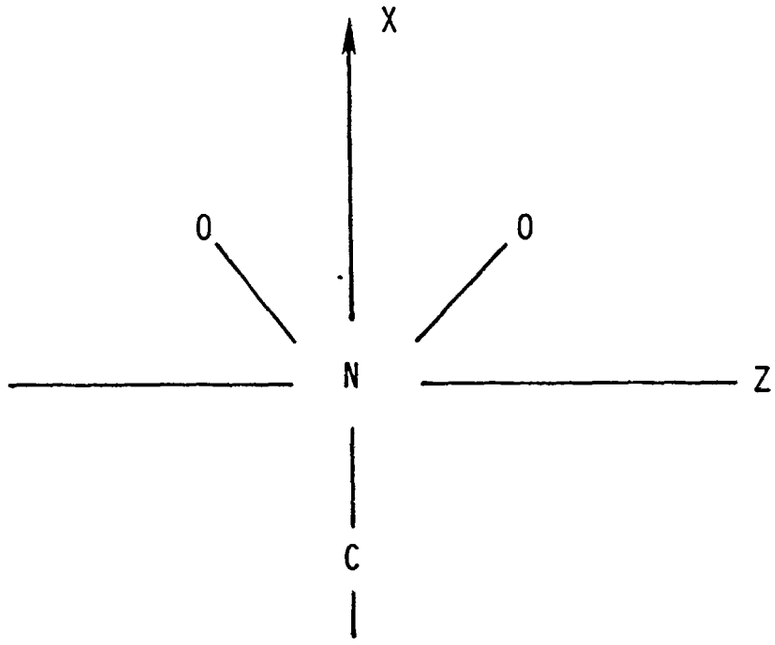

Figure 3.2.1-1. Electric Field Gradient Principal Axes System for the ^{14}N Site in the C-Nitro Group

TABLE 3.2.1-I

sp^2 hybrid orbitals and occupation numbers for the nitrogen site in C-Nitro compounds. The coordinate system of Figure 3.2.1-1 is used.

OCCUPATION NUMBER	NITROGEN ORBITAL
σ_{NO}	$\psi_{NOI} = \sqrt{\frac{1}{3}}\, s + \sqrt{\frac{1}{6}}\, p_x + \sqrt{\frac{1}{2}}\, p_z$
σ_{NO}	$\psi_{NOII} = \sqrt{\frac{1}{3}}\, s + \sqrt{\frac{1}{6}}\, p_x - \sqrt{\frac{1}{2}}\, p_z$
σ_{NC}	$\psi_{NC} = \sqrt{\frac{1}{3}}\, s - \sqrt{\frac{2}{3}}\, p_x$
π	$\psi_{\pi} = p_y$

BLOCK
ENGINEERING

Here q_o is the magnitude of the coupling constant per p-electron, a parameter estimated to be between -8 and -10 MHz. Although most of our conclusions will be insensitive to the particular choice of q_o, we prefer the latter value, and shall use it when necessary. The sign of q_o has been chosen so that all forms in Equations 3.2-2 are positive.

3.2.2 Structure and Bonding of TNT: Nitro Group Conformation

Equations 3.2-2 are the basis for the interpretation of the NQR data of α-TNT in terms of the structure and bonding of this molecule.

The first effect to be considered in the differential effect which the methyl-group will have on nitro-groups ortho and para to it. Fortunately, this general question of substituent effects on NQR parameters has been thoroughly investigated, most notably by Bray and coworkers[33] and is well understood. The main results is that good correlations can be obtained between measured field gradients and Hammet σ constants. The later are a measure of the ability of the substituent to withdraw or supply electrons to a reaction site. It should be noted, however, that these constants are determined in the liquid state. Thus it is not surprising that their correlation with NQR data obtained in solids breaks down when anisotropic interactions are strong.

In the case of α-TNT, considerations of the chemical inequivalence of the ortho and para nitro-groups using the correlations found by Subbarao and Bray[34], lead to expectations of frequency shift less than 10 kHz. Clearly, these shifts are much less than the splittings of actual TNT frequencies. We conclude that chemical inequivalence due to the electron releasing property of the methyl group cannot even begin to explain the observed NQR data in α-TNT.

BLOCK ENGINEERING

We now turn to a consideration of the possibility of strong physical inequivalence of the nitro-groups in nitrobenzenes. In fact crystallographic studies of these substances show that the plane of the NO_2-group can exist in equilibrium in solids at relatively large angles of rotation from the plane of the benzene ring. This rotation occurs mainly about the CN bond, not withstanding the large expected double bond character of this bond. The crystallographic studies, taken together, indicate that this angle of twist generally increases with the number of neighboring substituents on the benzene ring. What is surprising is that even with no neighbors, angles of up to 10° or more are common. One substituent ortho to the nitro-group can lead to twist angles of the order of 30° to 40°, while rotations of up to 60° or 70° are found when both sites ortho to the nitro-group have a bulky substituent. In addition to the effect of steric hindrance from neighboring substituents, the details of crystal packing and of intermolecular interactions are responsible for further variations in the nitro-group twist angles.

When the plane of a nitro-group in a nitro benzene is constrained to be twisted away from the plane of the benezene ring by a rotation about the CN (for any of the reasons outlined above) it follows that at the same time there will be a decrease in the double bond character of the CN bond. Clearly, the overlap integral between the $p\pi$ orbitals of the ring carbon and of the nitrogen atom will show a strong dependence on the nitro-group twist angle. One would expect that this overlap integral would act as a gate which can modulate the otherwise strong electrophilic properties of the nitro-group. Thus, these first order considerations lead us to the expectation that increasing the nitro-group twist angle would result in a decrease in the $p\pi$ electron population of the nitro-group.

BLOCK ENGINEERING

Since quadrupole coupling constants are very sensitive to the electron densities local to the resonant nucleus, one expects that the Nitrogen-14 NQR spectra of nitrobenzenes would provide a good test of these hypotheses.

Analyses of the data reported in previous ^{14}N NQR studies of nitrobenzenes[34,35] dealing mainly with planar molecules, disclose that of the three nitrogen occupation numbers, σ_{NO}, σ_{NC}, and π, variations in the first reflected variations in resonance as well as inductive effects of various substituents. (The occupation numbers were defined on page 3-12.) On the other hand, the occupation number σ_{NC} is found to be insensitive to resonance effects. Thus of the Townes-Dailey relations, Equation 3.2-2c is the one to be used in a study of the nitro-group twist since it best separates resonance from inductive effects at the Nitrogen site.

$$(\sigma_{NC} - \pi) = (2\nu_- - \frac{4}{3}\ \nu_+)/q_o \qquad (3.2\text{-}2c)$$

(repeated for convenience)

Figure 3.2.2-1 is a plot of $(2\nu_- - \frac{4}{3}\nu_+)$ for each of the six Nitrogen-14 NQR sites in monoclinic α-TNT vs. the nitro-group twist angle, θ, as measured by Duke[28]. Note that the figure shows a very suggestive relation between the NQR spectroscopic parameters and the structural parameter, θ. This relation indicates that there is a loss of nitrogen $p\pi$ orbital occupation of the order of 1/3 of a milli-electron per degree of nitro-group twist.

BLOCK ENGINEERING

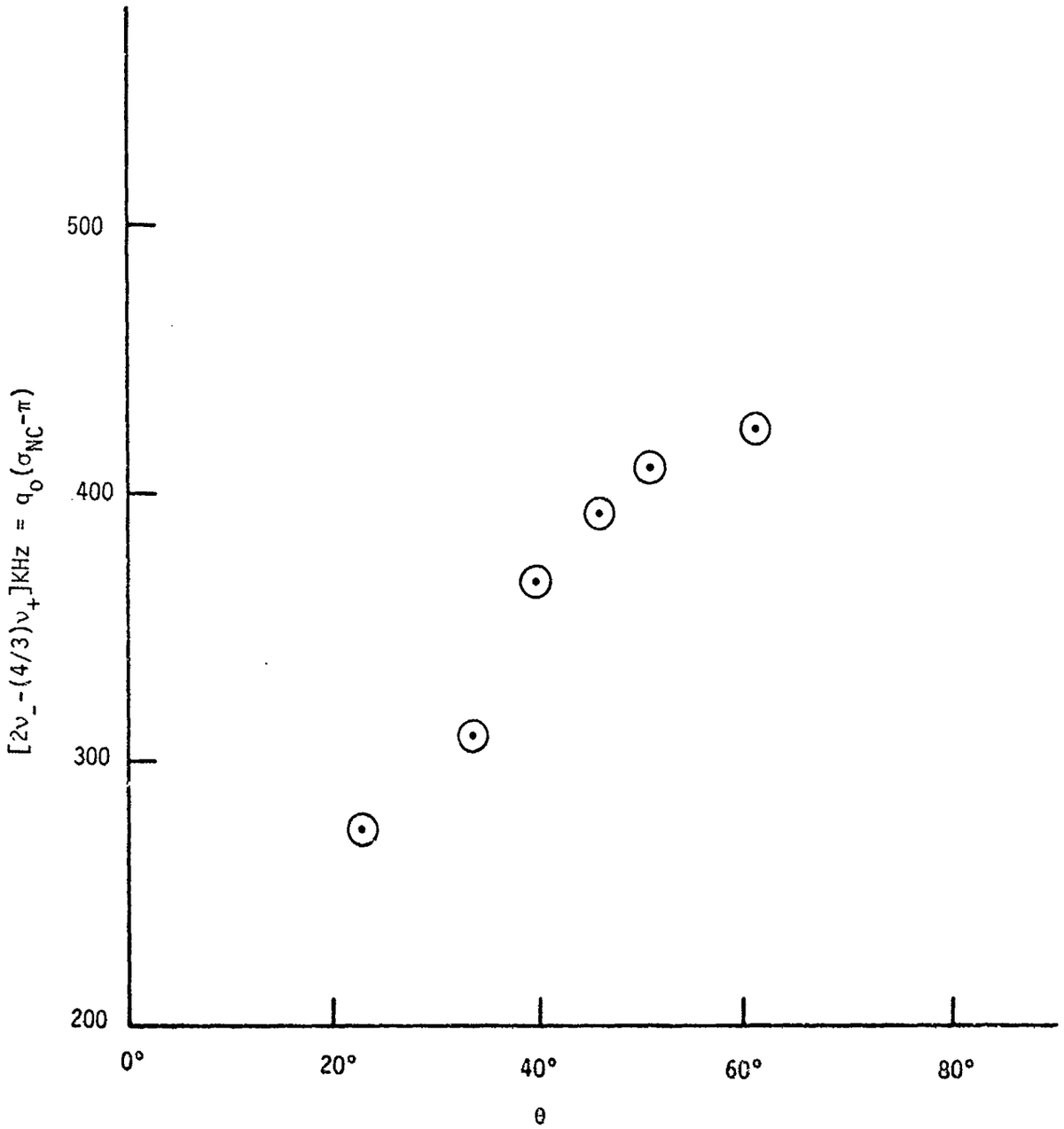

Figure 3.2.2-1. A plot of the expression $(2\nu_- - 4/3\ \nu_+)$ as a function of the Nitrogen-14 lines for each six sites of monoclinic α-TNT at 77°K vs. θ, the angle of twist of the nitro-group about the CN bond axis.

BLOCK ENGINEERING

The NQR data used in Figure 3.2.2-1 were obtained at 77°K; the temperature dependence of the NQR data is discussed in Section 3.3. The assignment of crystallographic sites to NQR sites was done by matching sites with a higher value of the twist angle with sites with lower values of the occupation number π. Of course, this ensures that a curve connecting the points plotted in Figure 3.2.2-1 be monotonic. The argument that the correlation depicted in Figure 3.2.2-1 is real finally rests on the self consistency of the assignment and on its predictive value. The temperature dependence of the NQR lines, discussed in Section 3.3, will provide part of this support. In the next section (3.2.3) we turn to an NQR study of other nitrobenzenes to test the predictive value of the relation discovered in Figure 3.2.2-1.

3.2.3 Structure and Bonding of TNT: Supporting NQR Data

In the previous section we showed how the details of the NQR spectrum of α-TNT could be accounted for by considering the effect on the nitrogen $p\pi$ population due to the rotation of the plane of the nitro-group about the CN bond axis. Here we show how NQR data in other nitrobenzenes support the model we developed. Table 3.2.3-I is a collection of ^{14}N NQR data for nitrobenzenes at 77°K. Each NQR site is given a reference number. Numbers 1 to 12 correspond to the twelve sites observed in the two phases of α-TNT. Numbers 13 to 23 are new data presented here for the first time, and numbers 24 to 28 represent all the nitrobenzenes for which ^{14}N NQR data was previously available and which also satisfy the two following additional requirements,

a) A crystal structure is available[36-40]
b) No hydrogen bonding is possible

BLOCK ENGINEERING

TABLE 3.2.3-I

NITROGEN-14 NQR SPECTRAL DATA FOR SOME NITROBENZENES AT 77°K. ALSO LISTED IS THE ANGLE OF TWIST OF THE NO_2-GROUP RELATIVE TO THE BENZENE RING

#	COMPOUND/SITE	ν_- kHz	ν_+ kHz	e^2qQ/h kHz	η	$\nu_0(\sigma_{NC}-\pi)=(2\nu_- - 4\nu_+/3)$ kHz	ϑ NITRO GROUP TWIST ANGLE (DEGREES)
	α-TNT (Monoclinic)						
1	oAI	792.1	869.4	1107.7	0.1396	425.0	60.06[a]
2	oAII	801.8	895.4	1131.5	0.1654	409.7	50.47
3	oBII	767.7	857.0	1083.1	0.1649	392.7	46.19
4	oBI	767.3	875.6	1095.3	0.1978	367.1	40.48
5	pI	729.7	861.8	1061.0	0.2490	310.3	32.88
6	pII	730.1	888.1	1078.8	0.2929	276.1	22.45
	α-TNT (orthorhombic)						
7	oAI	792.4	867.8	1106.8	0.1362	427.7	59.52[a]
8	oAII	803.2	897.9	1134.1	0.1670	409.2	50.92
9	oBII	768.5	858.6	1084.7	0.1661	392.2	45.70
10	oBI	766.5	875.7	1094.8	0.1995	365.4	41.32
11	pI	727.4	862.3	1059.8	0.2546	305.1	32.80
12	pII	732.5	885.6	1078.7	0.2839	284.2	22.33
13	Trinitrobenzene	758.0	959.4	1144.9	0.3518	236.8	
14	(TNB)	752.6	957.4	1140.0	0.3593	228.7	3-10[b]
15		734.6	931.5	1110.7	0.3545	227.1	
16		717.2	907.	1082.8	0.3506	225.1	
17		668.6	884.	1035.1	0.4162	158.5	8° BEND
18		704.0	832.	1024.0	0.2500	298.7	28
19	m-Dinitrobenzene	811.0	1030.0	1227.3	0.3569	248.7	10.3[c]
20		815.7	1037.8	1235.7	0.3595	247.7	12.4
21	Trinitro-m-Xylene	759.[d]	822.			422.0	75.2[e]
22	(TNX)		886.			336.7	35.7
23	3,4,6-Trinitro-1-t-Butyl-3,5-Dimethyl Benzene (TBDB)	752.8	825.1	1051.9	0.1375	405.5	Not Available
24	Nitrobenzene[f]	925.	121.3	1425.3	0.4041	232.7	0[g]
25	p-Nitrotoluene[h]	911.	119.8	1406.0	0.4083	224.7	3.0[i]
26	p-Dinitrobenzene[j]	834.	103.7	1247.5	0.3259	284.9	11.6[i]
27	p-Nitrobenzonitrile[k]	875	111.6	1277.3	0.3631	262.0	10.3[k]
28	p-Chloronitrobenzene[l]	840.	106.6	1273.7	0.3557	252.7	0[m]

BLOCK ENGINEERING

FOOTNOTES TO TABLE 3.2.3-I

a) Reference 28

b) Reference 41

c) Reference 42

d) Presumed ν_- doublet

e) Reference 43

f) S.N. Subbarao, E.G. Sauer and P.J. Bray, Phys. Letters 42A, 461 (1973)

g) Reference 36

h) Reference 34

i) Reference 37

j) Reference 38

k) Reference 39

l) Reference 35

m) Reference 40

The last requirement is necessary since it has long been known that hydrogen bonding in the solid state contributes its own specific perturbations of NQR spectra. These effects are irrelevant to the present arguments and would unnecessarily complicate our analysis.

The four additional compounds whose NQR data were obtained as part of this study are the following:

a) s-Trinitrobenzene (TNB). Three of these twelve lines were reported by Subbarao and Brady[34]. Six pairs of ν_+ and ν_- lines are reported here, in agreement with the multiplicity expected from the results of a crystal structure study[41].

b) m-Dinitrobenzene (DNB). Subbarao and Brady[34] using single shot spin-echo techniques, are Cheng and Brown[35] using Nuclear Quadrupole Double Resonance techniques, both report only one pair of ^{14}N lines. Available crystal structure studies[42], however, indicate the presence of <u>two</u> inequivalent NO_2 groups in this crystal. Using the sensitivity enhancements and the high resolution capabilities of multiple pulse FT-NQR spectroscopy (see Sections 2.1 and 2.2) we were able to easily resolve the "lines" reported in the literature[34,35] into doublets of spacing 5.7 KHz and 7.8 KHz, respectively for the ν_+ and ν_- resonances.

c) Trinitro-m-xylene (TNX). This compound was synthesized for us by Dr. Prince of Hunter College of CUNY. It was chosen because a crystal structure study[43] reports it to have such large nitro-group twist angles, 35.7° and 75.2°, that it should make a strong test of the correlation introduced in the previous section.

BLOCK ENGINEERING

(d) 2,4,6-Trinitro-1-t-Butyl-3,5-Dimethylbenzene (TBDB). This analogue of α-TNT has correspondingly bulkier substituents surrounding the s-Trinitrobenzene skeleton. In addition, it is commercially available from K&K Laboratories, Plainview, NY.

In addition, to ^{14}N-NQR data for all of the above compounds Table 3.2.3-I also lists the crystallographically determined nitro-group twist angle, θ, when available. Also listed is the NQR parameter $(2\,\nu_- - \frac{4}{3}\,\nu_+)$ which according to Equation 3.2-2c yields a measure of the nitrogen pπ orbital occupation number. Figure 3.2.3-1 is a plot of this NQR parameter vs. the sin θ. Note that we use the sin θ function instead of simply θ as the abscissa of our plot. The sin θ is a more appropriate function here since we wish to display the change of nitrogen pπ orbital occupation, an effect which is zero for θ=0 and maximum when θ=90°.

Figure 3.2.3-1 shows that over a rather large range of the angle of twist, θ, there is an approximately linear variation in the double-bond character of the CN bond, and that this relationship is amply demonstrated by the NQR data.

3.3 TEMPERATURE DEPENDENCE

The temperature dependence of the twenty-four ν_- and ν_+ lines in α-TNT between 77°K and room temperature are listed in Table 3.3-I (monoclinic phase) and Table 3.3-II (orthorhombic phase.) Graph of these data are depicted in Figure 3.3-1 and Figure 3.3-2, respectively.

BLOCK ENGINEERING

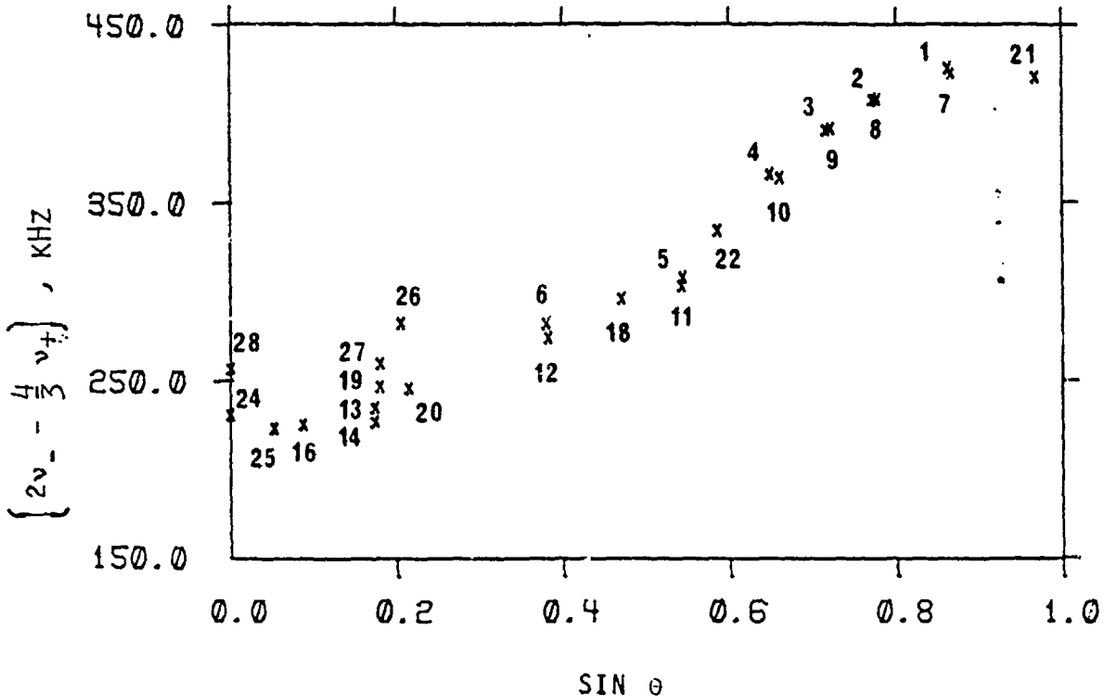

Figure 3.2.3-1 Plot of the parameter $(2\nu_- - \frac{4}{3}\nu_+)$, shown in the text to be proportional to the nitrogen $p\pi$ occupation number of the NO_2 group, vs. the sine of the angle of twist θ, of the NO_2 group away from the plane of the benezene ring.

BLOCK ENGINEERING

TABLE 3.3-I

LIST OF TWELVE NITROGEN-14 NQR SPECTRAL FREQUENCIES FOR MONOCLINIC TNT AS A FUNCTION OF TEMPERATURE FROM 77°K to 321°K

T,°K	ν,kHz	T,°K	ν,kHz	T,°K	ν,kHz	T,°K	ν,kHz
77.0	729.7	77.0	730.1	77.0	767.3	77.0	767.7
97.3	729.4	97.3	729.4	96.1	766.5	96.1	766.5
160.9	726.0	160.9	726.0	166.3	759.2	166.3	759.8
211.7	722.1	211.7	722.1	215.0	752.4	215.0	754.0
249.0	718.9	249.0	718.9	222.0	751.4	222.0	753.2
265.5	717.0	265.5	717.0	234.8	749.6	234.8	751.5
272.2	716.3	272.2	716.3	251.0	746.9	251.0	749.4
288.0	715.1	288.0	715.1	265.5	744.3	272.2	746.9
306.3	713.4	306.3	713.4	272.2	743.0	288.0	744.0
321.4	711.6	321.4	711.6	320.3	735.1	306.3	741.4
						321.4	739.2
77.0	792.1	77.0	801.8	77.0	857.0	77.0	861.8
95.5	790.9	106.8	799.8	109.9	855.8	116.3	860.5
170.7	778.9	174.2	790.2	144.0	852.9	146.5	858.3
217.7	769.5	221.0	782.4	177.4	849.9	180.6	855.7
252.3	761.8	253.6	776.5	195.0	848.2	198.2	854.2
265.5	758.3	265.8	774.1	224.5	845.3	225.8	851.7
272.2	756.7	272.2	772.9	237.4	844.1	240.4	850.3
288.0	753.2	288.0	770.0	265.8	840.6	265.8	847.6
306.3	748.6	306.3	766.5	272.2	839.8	272.2	846.8
321.6	744.6	321.6	763.5	288.0	838.1	288.0	845.1
				306.3	835.8	306.3	842.6
				321.6	833.7	320.6	841.0
77.0	869.4	77.0	875.6	77.0	888.1	77.0	895.4
119.4	867.0	124.9	872.0	130.0	885.8	132.4	889.7
148.9	864.0	151.1	868.9	155.2	884.0	157.2	885.5
182.6	860.9	184.5	864.6	188.0	881.3	188.0	880.6
201.9	857.6	204.9	862.0	209.9	879.3	209.9	876.9
228.5	853.8	229.5	858.4	233.8	877.0	232.8	872.4
240.4	852.2	242.7	856.6	248.3	875.6	246.0	870.1
265.5	847.6	265.5	852.9	266.3	873.4	266.0	865.5
272.2	846.8	272.2	851.9	272.2	872.6	272.2	864.2
288.0	844.1	288.0	849.6	288.0	871.1	288.0	860.9
306.3	840.7	306.1	847.6	306.1	869.2	306.1	856.6
321.6	837.5	321.6	844.0	321.1	867.3	321.1	853.3

TABLE 3.3-II

LIST OF TWELVE NITROGEN-14 NQR SPECTRAL FREQUENCIES FOR ORTHORHOMBIC TNT AS A FUNCTION OF TEMPERATURE FROM 77°K TO 279.6°K

T,°K	ν,kHz	T,°K	ν,kHz	T,°K	ν,kHz	T,°K	ν,kHz
77.0	727.4	77.0	732.5	77.0	766.5	77.0	768.5
81.8	727.3	81.8	732.4	83.2	766.5	83.2	768.5
87.4	727.2	88.8	732.4	90.9	766.2	90.9	768.1
106.8	726.5	106.8	731.8	116.3	763.8	116.3	765.6
127.4	725.3	113.2	731.4	126.6	762.8	126.6	764.8
156.7	723.4	129.3	730.3	144.8	761.0	144.8	762.4
170.0	722.5	141.4	729.6	163.1	758.8	163.1	760.1
187.8	721.4	173.4	727.3	175.6	757.3	175.6	758.5
205.2	720.0	189.5	726.1	179.6	756.9	179.6	758.0
214.0	719.3	206.9	724.8	192.0	755.3	192.0	756.3
225.3	718.4	215.7	724.0	208.7	753.4	208.7	754.1
239.9	717.1	226.5	723.1	217.2	752.1	217.2	752.9
279.6	713.8	236.9	721.9	227.8	750.7	227.8	751.5
		279.6	718.0	240.9	749.4	240.9	749.4
				279.6	743.7	279.6	743.7
77.0	792.4	77.0	803.2	77.0	858.6	77.0	862.3
84.1	792.3	85.7	803.1	81.3	858.3	81.3	862.1
96.1	791.2	101.8	801.4	83.2	858.6	83.2	862.2
119.7	787.3	123.7	798.4	90.9	858.0	90.5	861.9
150.6	782.6	153.5	794.0	104.9	857.3	108.7	861.1
165.3	780.0	165.3	792.6	128.8	855.2	131.9	860.0
182.8	776.9	185.0	789.0	131.7	854.9	138.2	859.5
197.0	774.0	199.2	786.8	153.0	852.9	155.5	858.4
210.7	771.3	212.5	784.4	163.3	852.0	167.7	857.7
220.2	769.1	221.7	782.6	172.4	851.1	175.4	857.1
229.0	767.3	229.0	781.0	183.8	849.7	179.3	856.7
242.7	764.7	244.2	778.6	191.0	849.0	187.5	856.2
279.6	755.6	279.6	771.8	193.5	848.8	196.0	855.7
				204.2	847.7	208.9	854.6
				217.7	846.0	221.0	853.5
				219.0	846.2	235.3	852.3
				220.2	846.0	248.5	851.3
				231.6	844.7	259.9	850.5
				233.1	844.6	279.6	848.0
				246.2	842.9		
				256.1	842.0		
				279.6	839.5		

TABLE 3.3-II (CONCLUDED)

LIST OF TWELVE NITROGEN-14 NQR SPECTRAL FREQUENCIES FOR ORTHORHOMBIC TNT AS A FUNCTION OF TEMPERATURE FROM 77°K TO 279.6°K

T,°K	ν,kHz	T,°K	ν,kHz	T,°K	ν,kHz	T,°K	ν,kHz
77.0	867.8	77.0	875.7	77.0	885.6	77.0	897.9
80.4	867.8	80.1	875.6	80.4	885.5	80.6	897.8
84.3	867.8	85.5	875.6	86.5	885.5	87.6	897.5
91.9	867.5	92.8	875.1	98.7	884.9	119.0	892.5
134.6	864.0	95.2	875.0	103.2	884.8	142.3	890.0
141.4	863.0	137.2	870.5	115.6	884.0	155.2	888.0
157.9	861.0	143.8	869.6	146.2	881.8	165.3	886.4
170.0	860.0	160.6	867.6	163.1	880.5	177.9	884.7
181.8	858.4	177.6	865.6	175.1	879.5	184.5	883.1
189.7	857.6	192.2	863.3	182.6	879.0	198.7	880.6
207.7	855.1	194.0	863.2	196.5	877.8	205.7	879.4
221.5	853.6	200.0	862.3	201.5	877.6	237.6	873.4
248.5	849.5	201.5	861.9	214.2	876.4	253.8	870.2
258.4	848.1	210.0	860.5	224.5	875.6	279.6	864.7
279.6	844.6	222.7	859.1	226.0	857.3		
		224.5	858.9	227.3	875.3		
		229.3	858.3	227.5	875.1		
		236.4	857.1	237.6	874.2		
		250.3	855.1	239.4	874.0		
		262.5	853.4	253.8	872.9		
		279.6	850.5	279.6	870.0		

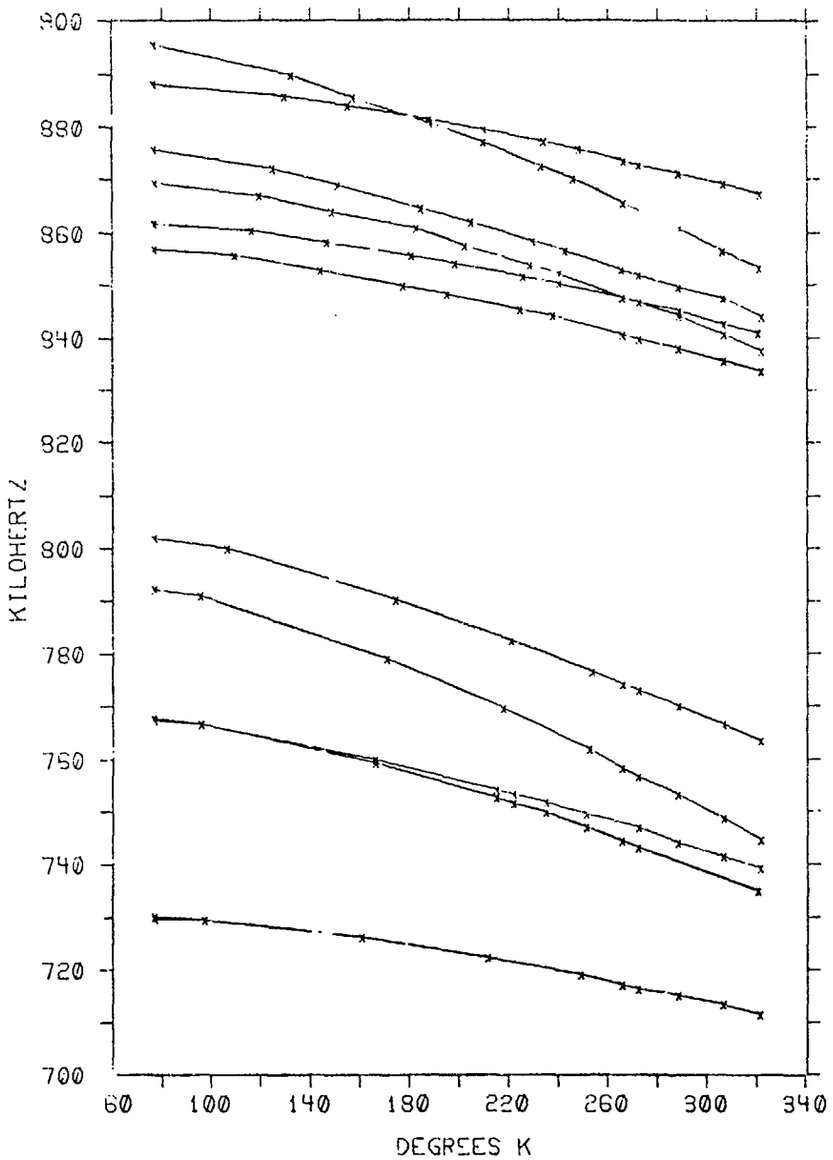

Figure 3.3-1. Temperature Dependence of the Nitrogen-14 NQR Spectrum of MONOCLINIC TNT

BLOCK
ENGINEERING

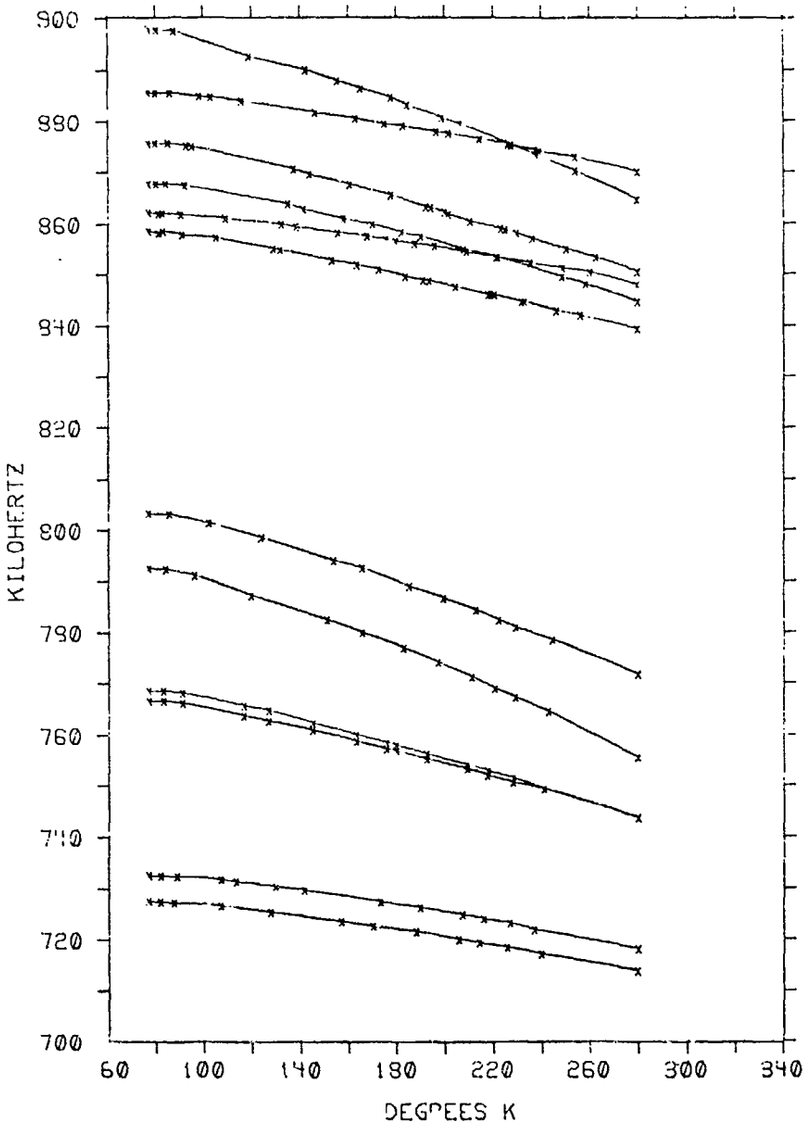

Figure 3.3-2. Temperature Dependence of the Nitrogen-14 NQR Spectrum of ORTHORHOMBIC TNT

BLOCK
ENGINEERING

Thermal motions present in all crystals occur at frequencies that are much greater than NQR transitions, thus the electric field gradients actually measured by NQR techniques are time-averaged over these motions. Larger librational amplitudes are generally more efficient at this averaging process, so that, typically, NQR frequencies are monotonically decreasing functions of the temperature. Figures 3.3-1 and 3.3-2 clearly demonstrate this feature. It is generally a good assumption to describe the torsional motions by an Einstein model, and then the root mean square of the amplitudes about the x,y, and z inertial axes of the nitro-group are given by

$$\langle \Delta\theta_i^2 \rangle = \frac{h}{4\pi^2 I_i \nu_i} \left(\frac{1}{2} + \frac{1}{\exp(h\nu_i/kT)-1} \right) \; ; \; i=x,y,z \qquad (3.3\text{-}1)$$

where I_i is the effective moment of inertia about the ith principal axis and ν_i is the torsional frequency. To the extent that the principal axes of the inertial tensor coincide with the electric field gradient tensor principal axes, the change in the coupling constant and asymmetry parameter can be expressed as[44,45]

$$\frac{(e^2qQ)_T}{(e^2qQ)_{T=0}} = 1 - \frac{3}{2} \left[\langle \Delta\theta_x^2 \rangle + \langle \Delta\theta_y^2 \rangle \right] + \frac{\eta}{2} \left[\langle \Delta\theta_y^2 \rangle - \langle \Delta\theta_x^2 \rangle \right] \qquad (3.3\text{-}2)$$

and

$$\frac{\eta(T)}{\eta(T=0)} = \frac{(e^2qQ)_T}{(e^2qQ)_{T=0}} \left[1 - \frac{1}{2} \left[\langle \Delta\theta_x^2 \rangle + \langle \Delta\theta_y^2 \rangle \right] + \frac{3}{2\eta} \left[\langle \Delta\theta_y^2 \rangle - \langle \Delta\theta_x^2 \rangle \right] - 2 \langle \Delta\theta_z^2 \rangle \right] \qquad (3.3\text{-}3)$$

BLOCK ENGINEERING

An analysis of the temperature dependence of both phases of α-TNT shows that the main features of the data can be explained by considering only the torsional motion of each NO_2 group about the C-N bond, i.e. by considering only the effect of $\langle\Delta\theta_x^2\rangle$ and assuming that $\langle\Delta\theta_y^2\rangle = \langle\Delta\theta_z^2\rangle$ = zero. Here, we are labelling the axes according to the convention given in Figure 3.2.1-1. With these assumptions, Equation 3.3-2 can be rewritten as,

$$\langle\Delta\theta_x^2\rangle = \langle\Delta\theta\rangle^2_{RMS} = \frac{(e^2qQ)_{T=0} - (e^2qQ)_T}{2h\nu_+} \qquad (3.3\text{-}4)$$

Figures 3.3-1 and 3.3-2 show that at 77°K there is little temperature dependence, so we make only a small error by taking the "T=0" values at this temperature. Table 3.3-III shows the components of the electric field gradient (EFG) tensor q_{xx}, q_{yy}, and q_{zz} at both 77°K and 321°K for monoclinic TNT. The EFG tensor components were computed from the frequencies using the relations,

$$q_{zz} = \frac{3}{2}\, h\, (\nu_+ + \nu_-)/(e^2 q_o Q), \qquad (3.3\text{-}5)$$

$$q_{yy} = -\, q_{zz}\, (1 + \eta)/2, \qquad (3.3\text{-}6)$$

$$q_{xx} = -\, q_{zz}\, (1 - \eta)/2. \qquad (3.3\text{-}7)$$

In the fourth column of Table 3.3-III we compute Δq, the change in EFG component due to the rise in temperature. Note that if an average of Δq is taken over molecules I and II, as is done in the fifth column of the Table, it becomes clear that in fact the major change is due solely to changes in q_{zz}. As proof for this assertion, note that the relations $|\Delta q_{xx}| \approx |\Delta q_{yy}| \approx |\frac{1}{2} q_{zz}|$ hold reasonably well, as can be ascertained by comparing the entries joined by the double pointed arrow.

BLOCK ENGINEERING

TABLE 3.3-III

THE COMPONENTS q_{xx}, q_{yy}, and q_{zz} OF THE ELECTRIC FIELD GRADIENT TENSOR OF MONOCLINIC TNT AT 77°K AND AT 321°K.

TNT SITE	T=77°K	T=321°K	Δq	$\frac{\Delta q_I + \Delta q_{II}}{2}$	$q_{zz}/2$
	$-q_{xx}$	$-q_{xx}$			
oAI	476.1	434.4	42.1	32.6 ↔	26.6
oAII	472.2	449.1	23.1		
oBII	452.3	425.8	26.5	24.2 ↔	19.3
oBI	439.3	417.4	21.9		
pI	398.4	388.1	10.3	10.5 ↔	13.1
pII	381.4	370.6	10.8		
	$-q_{yy}$	$-q_{yy}$			
oAI	631.2	620.3	10.9	20.7 ↔	26.6
oAII	659.3	628.8	30.5		
oBII	630.9	622.8	8.1	14.4 ↔	19.3
oBI	656.0	635.3	20.7		
pI	662.6	647.0	15.6	15.5 ↔	13.1
pII	697.4	628.0	15.4		
	q_{zz}	q_{zz}			
oAI	1107.7	1054.7	53.0	53.3	
oAII	1131.5	1077.9	53.6		
oBII	1083.1	1048.6	34.5	38.6	
oBI	1095.3	1052.7	42.6		
pI	1061.0	1035.1	25.9	26.1	
pII	1078.8	1052.6	26.2		

BLOCK ENGINEERING

Table 3.3-IV is analogous to Table 3.3-III in that it lists the EFG components for the orthorhombic phase of TNT for both 77°K and 279.6°K. Here also it is approximately true that $|\Delta q_{xx}| \approx |\Delta q_{yy}| \approx |\frac{1}{2} \Delta q_{zz}|$, validating our assumption that $\Delta\theta_y \approx \Delta\theta_z \approx 0$.

Finally, in Table 3.3-V the root mean square angles of nitro-group libration, $\langle\Delta\theta_x\rangle$ RMS, are computed from Equation 3.3-4 and listed together with R.C.J. Duke's values of the equilibrium angle of nitro-group twist. Note that the angular displacements are considerable in magnitude in all cases, and are larger for larger values of θ. This can be understood as an indication that cases with a larger value of θ, and therefore with a weaker double-bond character, have a correspondingly less stiff torsional spring constant. Thus larger torsional angles are reached at any given temperature. The implications of these considerations to the thermal break up of the α-TNT molecule deserve further study.

TABLE 3.3-IV

THE COMPONENTS q_{xx}, q_{yy}, and q_{zz} OF THE ELECTRIC FIELD GRADIENT TENSOR OF ORTHORHOMBIC TNT AT 77°K AND AT 279.6°K.

	77°K	279.6°K	Δq	$\frac{\Delta q_I + \Delta q_{II}}{2}$	$\frac{1}{2} q_{zz}$
	$-q_{xx}$	$-q_{xx}$			
oAI	478.0	444.4	33.6	26.7 ↔	20.8
oAII	472.3	452.6	19.7		
oBII	452.3	431.9	20.4	17.0 ↔	15.3
oBI	438.2	424.6	13.6		
pI	395.0	386.4	8.6	8.8 ↔	9.7
pII	386.3	377.3	9.0		
	$-q_{yy}$	$-q_{yy}$			
oAI	628.8	622.4	6.4	14.9 ↔	20.8
oAII	661.7	638.4	23.3		
oBII	632.5	623.5	9.0	13.7 ↔	15.3
oBI	656.6	638.2	18.4		
pI	664.8	654.8	10.0	10.6 ↔	9.7
pII	692.5	681.3	11.2		
	q_{zz}	q_{zz}			
oAI	1106.8	1066.8	43.0	41.6	
oAII	1134.1	1091.0	43.1		
oBII	1084.7	1055.5	29.2	30.6	
oBI	1094.8	1062.8	32.0		
pI	1059.8	1041.2	18.6	19.3	
pII	1078.7	1058.7	20.0		

BLOCK ENGINEERING

TABLE 3.3-V

THE ROOT MEAN SQUARE LIBRATIONAL ANGLE $\langle\Delta\theta_x\rangle_{RMS}$ AT ROOM TEMPERATURE FOR MONOCLINIC (44°C) AND ORTHORHOMBIC (2.6°C) TNT. ALSO SHOWN IS THE CRYSTALLOGRAPHIC NITRO GROUP TWIST ANGLE DEFINED IN THE TEXT.

SITE	$\langle\Delta\theta_x\rangle_{RMS}$	θ[a]
MONOCLINIC TNT		
oAI	10.2°	60.06°
oAII	10.2°	50.47°
oBII	8.2	46.19°
oBI	9.1°	40.48°
pI	7.1°	32.88°
pII	7.0°	22.45°
ORTHORHOMBIC TNT		
oAI	8.8°	59.52°
oAII	9.0°	50.92°
oBII	7.6°	45.70°
oBI	7.9°	41.32°
pI	6.0°	32.80°
pII	6.1°	22.33°

a) From R.C.J. Duke, Private Communication (1982)

BLOCK ENGINEERING

4.0 NQR STUDY OF HMX AND RDX[46]

4.1 INTRODUCTION

1,3,5,7- Tetranitro-1,3,5,7-Tetraazacyclooctane (HMX), shown in Figure 4.1-1, has been shown to exist in several crystal phases. For example, T.B. Brill and coworkers have used laser Raman spectroscopy to diagnose polymorphic interconversions as a function of temperature and pressure[47,48,49]. The stable form at room temperature is labelled β-HMX, while δ-HMX is the thermodynamically favorable form under the conditions of high pressure, for example those in a rocket motor[49].

Questions remain about the rate of the β→δ solid-solid transformation and mechanism of the solid phase events up to and including the phase transition. These problems relate directly to modelling of and performance in the combustion environment. While Raman spectroscopy is useful for distinguishing the HMX polymorphs[47] and for specifying some of the events leading to degradation in inorganic materials,[50] it has not proven to be as useful in elucidating the detailed events leading to degradation in HMX. This difficulty appears to result from the ready dissipation of thermal energy among the numerous internal stretching and bending modes of the HMX molecule. The vibrational spectrum of β-HMX shows gradual non-specific changes with temperature up to the phase transition.[47]

BLOCK ENGINEERING

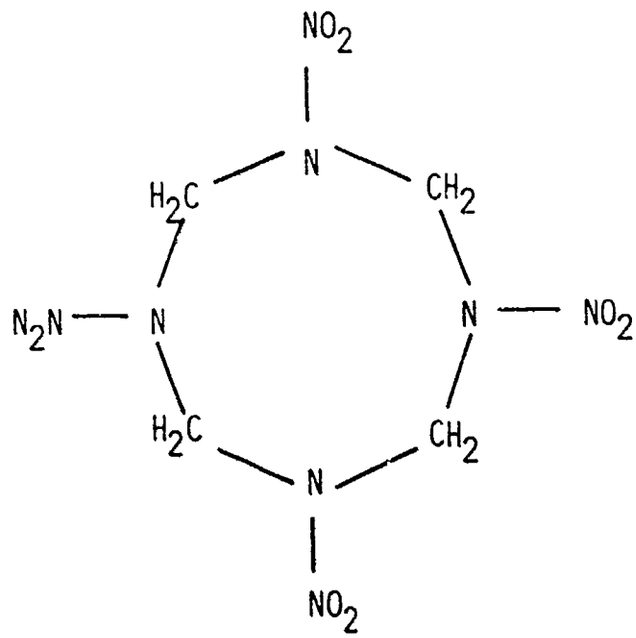

Figure 4.1-1. The HMX Molecule

Information about molecular dynamics in HMX should be obtainable if a spectroscopic technique is chosen which samples on a time scale of molecular rather than atomic motion. The mechanisms of solid phase events should be definable by this approach. Nitrogen-14 nuclear quadrupole resonance spectroscopy is just such a method, and it was employed for these studies. NQR frequencies aid in understanding the electron distribution in molecules,[2] while the temperature dependence of the resonance frequencies has been used to cast light on molecular motion in organic solids.[51,52,53,54]

We report here an analysis of the ^{14}N NQR data for the amine nitrogen atoms of HMX in terms of the electronic structure and librational motions of the molecule. The results are interpreted in light of the intermolecular cohesive forces that exist in the crystal lattice of β-HMX. The ^{14}N NQR data for the amine nitrogen atoms in RDX (hexahydro-1,3,5-trinitro-s-triazine), which is the six membered analog of HMX, are also reported here for purposes of comparison.

4.2 EXPERIMENTAL

Samples of HMX taken from the same batch were used without further purification in these studies. The particle size was 175μm.

BLOCK ENGINEERING

The nuclear quadrupole resonance measurements were made using a pulsed spectrometer whose details have been described elsewhere.[55] Heat-resistant, high-Q, NQR coils were constructed by wrapping Cu wire around a cylindrical sample bottle and coating the coil with high temperature resin to ensure that the coil would retain its geometric integrity throughout the temperature range.

Measurements of the frequency as a function of temperature were obtained by using a strong off-resonance comb of RF pulses (SORC), 2-6 KHz off-resonance.[4] The frequency was determined by directly measuring the period of oscillation from the transient NQR signal produced between pulses after 10^4 coadds on a PAR 4202 signal averager. This frequency measurement requires only about 10 sec. and produces an error of ±1KHz.

Temperature variations below 300° K were achieved by allowing very slow heat loss to occur from the sample. The NQR coil was mounted in a thick-walled Cu can. The can was placed in a bath of liquid N_2. The temperature of the sample was measured with a Fluke digital thermometer and an Omega stainless steel sheathed thermocouple. The thermocouple was wrapped with Teflon tape and placed directly into the HMX sample. The Teflon tape prevented any possible reaction between the sample and the thermocouple. After the temperature equilibrated at 77° K, it was removed from the bath, placed in a Dewar flask, and tightly insulated. The frequency measurements were made every 10°K by allowing the sample to warm slowly <u>via</u> thermal loss. The temperature of the sample was monitored continuously and all mesurements were made while the sample was within 0.5°K of the desired temperature.

BLOCK
ENGINEERING

For the frequency measurements above room temperature, a 2 liter Dewar flask was filled with silicone oil. An Omega model 402 temperature controller coupled to an immersion heater and an iron-constantan thermocouple was used for temperature regulation. A mechanical stirrer prevented temperature gradients in the bath. The temperature of the sample was monitored directly by the method described above. A vial of HMX was placed in the NQR coil and immersed in the silicone oil. The sample was heated in a stepwise fashion through the temperature range of 310°K-430°K. Frequency measurements were taken in approximately 10°K increments by heating at a rate of about one degree per minute to the desired temperature and then equilibrating for 5 min.

The variable temperature experiments were repeated several times, and a fresh sample of HMX was used each time. However, the resonance frequencies were observed to be the same whether the temperature run began at 310°K or 375°K. As long as the temperature was kept below the $\beta \rightarrow \delta$ solid phase transformation at 436°K, the resonance frequencies upon cooling to a specific temperature were the same as those obtained upon heating to that temperature.

4.3 RESULTS AND DISCUSSION

^{14}N nuclei (I=1) yields three NQR signals when $\eta \neq 0$. In order to assign the transitions correctly, ν_d was measured at 77°K and 298°K in HMX. The NQR data for a β-HMX over the temperature range of 77-426°K are compiled in Table 4.3-I. These signals arise from the amine nitrogen atoms of the ring. No attempt was made to obtain data for the much lower-frequency nitro-group nitrogen sites. ^{14}N NQR data at 77°K for the amine nitrogen atoms in RDX are given in Table 4.3-II.

BLOCK ENGINEERING

TABLE 4.3-I

^{14}N NQR DATA FOR THE AMINE NITROGEN ATOMS OF β-HMX

T, °K	ν, KHz		η	e^2Qq, kHz
	ν_+	ν_-		
77[a]	5336	3745	0.5256	6054
	5091	3628	0.5030	5813
83	5336	3745	0.5256	6054
	5090	3628	0.5031	5812
93	5334	3744	0.5254	6053
	5089	3628	0.5028	5811
103	5333	3744	0.5252	6051
	5088	3628	0.5025	5811
113	5331	3744	0.5246	6050
	5087	3628	0.5022	5810
123	5330	3744	0.5244	6049
	5086	3628	0.5020	5809
135	5328	3744	0.5238	6048
	5085	3628	0.5017	5809
143	5328	3744	0.5238	6048
	5085	3628	0.5017	5809
153	5326	3743	0.5237	6046
	5084	3628	0.5014	5808
163	5325	3743	0.5234	6045
	5083	3628	0.5011	5807
173	5324	3742	0.5235	6044
	5082	3627	0.5012	5806
183	5322	3742	0.5229	6043
	5080	3627	0.5006	5085
193	5320	3742	0.5224	6041
	5079	3627	0.5003	5805
203	5318	3742	0.5219	6040
	5078	3627	0.5001	5803
213	5317	3742	0.5216	6039
	5077	3627	0.4998	5802
223	5315	3742	0.5210	6038
	5075	3627	0.4992	5801

BLOCK ENGINEERING

TABLE 4.3-I (CONTINUED)

^{14}N NQR DATA FOR THE AMINE NITROGEN ATOMS OF β-HMX

T, °K	ν, KHz		η	e^2Qq, kHz
	ν_+	ν_-		
233	5313	3740	0.5213	6035
	5073	3627	0.4986	5800
243	5311	3740	0.5207	6034
	5073	3625	0.4994	5799
253	5311	3737	0.5219	6032
	5073	3625	0.4994	5799
263	5308	3737	0.5211	6030
	5071	3625	0.4989	5797
273	5306	3737	0.5205	6029
	5068	3625	0.4980	5795
298[b]	5300	3737	0.5189	6025
	5063	3623	0.4977	5791
315	5297	3736	0.5184	6022
	5060	3623	0.4965	5789
324	5296	3736	0.5182	6021
	5059	3622	0.4966	5787
334	5295	3735	0.5183	6020
	5058	3621	0.4967	5786
344	5293	3735	0.5177	6019
	5055	3620	0.4963	5783
354	5290	3734	0.5173	6016
	5053	3620	0.4957	5782
364	5288	3733	0.5171	6014
	5051	3618	0.4959	5779
375	5285	3731	0.5171	6011
	5049	3618	0.4953	5778
385	5279	3731	0.5154	6007
	5047	3614	0.4964	5774
395	5276	3730	0.5150	6004
	5043	3613	0.4956	5771

TABLE 4.3-I (CONCLUDED)

^{14}N NQR DATA FOR THE AMINE NITROGEN ATOMS OF β-HMX

T, °K	ν, KHz		η	e^2Qq, kHz
	ν_+	ν_-		
405	5273	3730	0.5142	6002
	5040	3611	0.4955	5767
415	5272	3728	0.5147	6000
	5038	3610	0.4954	5765
426	5270	3726	0.5149	5997
	5032	3607	0.4948	5759

a) ν_d observed at 1591, 1462 KHz

b) ν_d observed at 1564, 1441 KHz

TABLE 4.3-II

^{14}N NQR DATA MEASURED IN RDX AT 77°K

ν, kHz				
ν_+	ν_-	ν_d	η	e^2Qq/h, kHz
5118.0	3394.2	1724.2	0.608	5674.8
5256.3	3413.5	1842.8	0.638	5779.9
5319.0	3511.5	1807.3	0.614	5887.0

The nuclear quadrupole coupling constant, e^2Qq/h, and the asymmetry parameter, η, can be calculated from the frequencies of ν_+ and ν_- by using Eqs.4.3-1 and 2.[56]

$$e^2Qq/h = 2/3\ (\nu_- + \nu_+) \tag{4.3-1}$$

$$\eta = 3\ \frac{(\nu_+ - \nu_-)}{(\nu_+ + \nu_-)} \tag{4.3-2}$$

The coupling constant measures the largest component of the electric field gradient (EFG) tensor, while η measures the departure of the EFG from axial symmetry about this component.

The four amine nitrogen atoms reduce to two pairs because of the C_i symmetry in the β-HMX molecule shown in Figure 4.3-1. These two pairs ($N_{2,2'}$ and $N_{3,3'}$) produce NQR signals whose coupling constants differ by 241 kHz at 77°K. This difference is about four percent of the overall EFG and is larger than that usually observed for simple crystallographic inequivalence of sites in organic molecular crystal. However, the difference is smaller than usually arises from chemical inequivalence. For convenience the amine atoms, $N_{3,3'}$ of β-HMX are referred to here as axial amines, while $N_{2,2'}$ are labeled the equatorial amine atoms in reference to the positions of the NO_2 groups bound to these nitrogens with respect to the plane of the ring.

BLOCK ENGINEERING

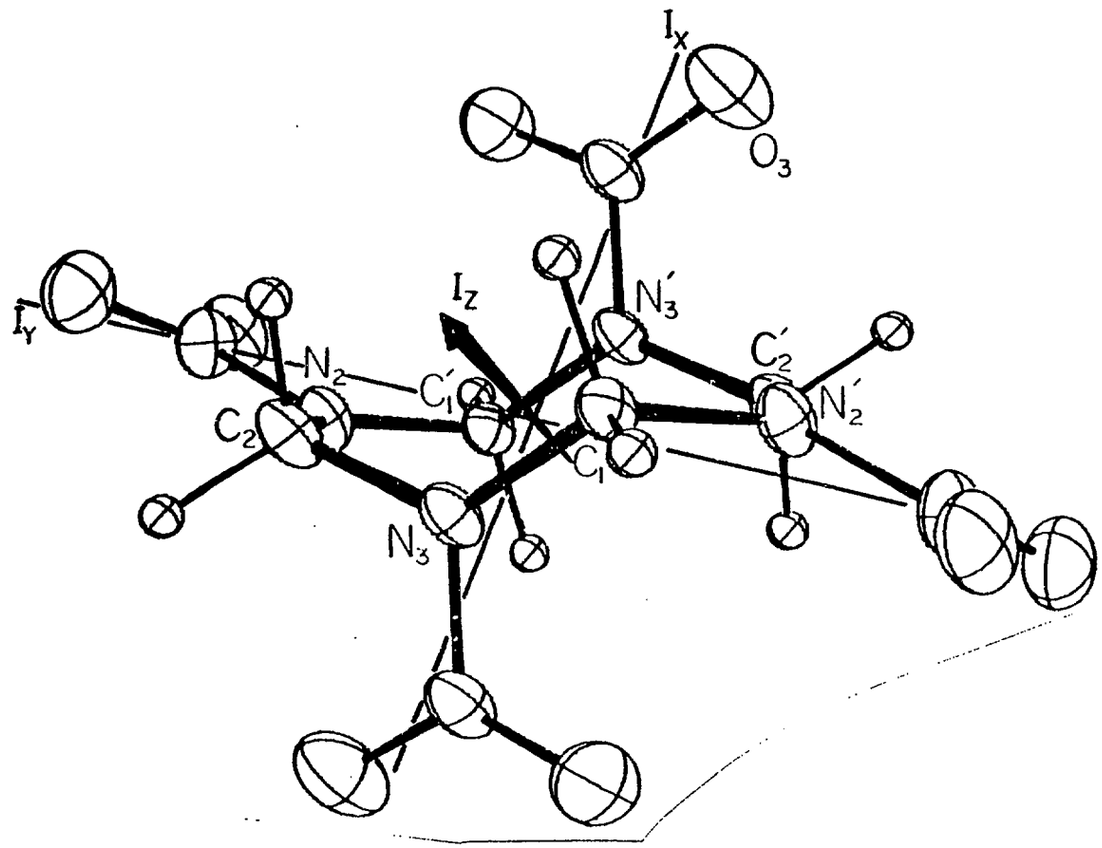

Figure 4.3-1. An ORTEP plot of β-HMX. The equatorial amine atoms are N_2N_2' and the axial amines are N_3N_3'. The orientation of the principal axes of the moment of inertia, I, is shown.

BLOCK ENGINEERING

Electronic Effects: Assignment of the nuclear quadrupole coupling constants to the axial and equatorial sets of the nitrogen atoms can be made by employing the Townes-Dailey formalism[39] and the crystal structure of β-HMX.[57]. In the Townes-Dailey model the diagonal components of the EFG tensor are described in terms of the electron populations of the atomic orbitals on the nitrogen atom.

The molecular structure of HMX reveals that the C_2NNO_2 unit of the molecule is nearly planar.[57] As a result, the σ-bonding orbitals on the amine nitrogen atoms can be constructed assuming sp^2 hybridization. It is helpful to consider the orientation of the EFG principal axes when constructing these hybrids in order that the convention of $|q_{zz}| \geq |q_{yy}| \geq |q_{xx}|$ is followed. The proper coordinate system usually can be chosen on the basis of the relative electronegativities of the atoms or an MO calculation, if available. Unambiguous assignment of the principal axes requires a single crystal Zeeman study or other experiments.[58] However, in the HMX case the orientation of the principal axes can be determined with some confidence without such studies. This is due to the fact that the sp^2 hybridized amine nitrogen atoms contain a pair of elctrons having π-bonding symmetry perpendicular to the C_2NNO_2 plane. Placing the Z axis of the EFG coincident with this electron pair is consistent with other studies involving substituted nitrogen atoms having sp^2 hybridization, [illegible]s urea,[59] thiourea,[60] N-methyl-pyrrole,[33] and hydroxypyrimidines.[illegible] The Y axis coincides with the N-N bond and the X axis is perpendicular to the YZ plane. Figure 4.3-2 pictorializes this axis system which was also used to construct the hybrid atomic orbitals listed in Table 4.3-III.

BLOCK ENGINEERING

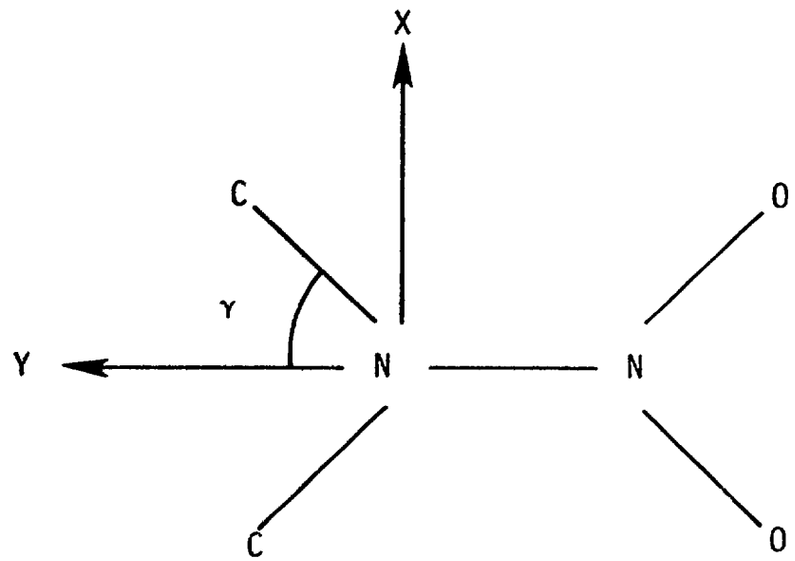

Figure 4.3-2. The approximate orientation of the principal axes of the EFG tensor of the amine atoms. Z is perpendicular to the molecular plane.

TABLE 4.3-III

THE HYBRID ORBITALS* OF THE AMINE NITROGEN ATOMS ACCORDING TO THE AXIS SYSTEM GIVEN IN FIGURE THE ORBITAL OCCUPATION NUMBERS ARE ALSO GIVEN

Wavefunctions	Orbital Occupations
$\psi_1 = \sqrt{[(1-\varepsilon^2)/2]}\ s - \sqrt{1/2}\ p_y + \sqrt{\varepsilon^2/2}\ p_x$	c_{NC}
$\psi_2 = \sqrt{[(1-\varepsilon^2)/2]}\ s + \sqrt{1/2}\ p_y + \sqrt{\varepsilon^2/2}\ p_x$	c_{NC}
$\psi_3 = \varepsilon s - \sqrt{1-\varepsilon^2}\ p_x$	b_{NN}
$\psi_4 = p_z$	

* $\varepsilon = \cot(\gamma)$

*N_π

BLOCK ENGINEERING

The Townes-Dailey Eq. 4.3-3 relates the diagonal components of the EFG tensor, q_{ii}, to the 2p orbital populations on nitrogen, N_p.

$$e^2Qq_{ii}/h = e^2Qq_p/h \left[N_{p_i} - \frac{N_{p_j} + N_{p_k}}{2} \right] ; \; x,y,z = i,j,k \qquad (4.3\text{-}3)$$

e^2Qq_p/h is the coupling constant produced by a single 2p electron on nitrogen. When the wavefunctions in Table 4.3-III are substituted into eq (4.3-3), one obtains Eq.4.3-4 and 4.3-5 which describe the coupling constant and asymmetry parameter, η, for the amine nitrogens in terms of the hybrid orbital populations, a,b, and c. [2]

$$\left(\frac{e^2Qq/h}{e^2Qq_p/h} \right) \eta = \frac{3}{2} \left(c_{NC} - b_{NN} \right) \left(1 - \cot^2\gamma \right) \qquad (4.3\text{-}4)$$

$$\left(\frac{e^2Qq/h}{e^2Qq_p/h} \right) \left(1 - \frac{\eta}{3} \right) = a_{N\pi} - c_{NC} \qquad (4.3\text{-}5)$$

Eq 4.3-4 contains the dependence of the EFG parameters on γ, which is one half the CNC angle in HMX. Inclusion of this refinement in the Townes-Dailey model hardly affects the results in HMX because $\gamma = 61.9°$ at the axial amine and $61.2°$ at the equatorial amine.[57] Thus, eliminating the angle term reduces Eq 4.3-4 to Eq 4.3-6.

$$\left(\frac{e^2Qq/h}{e^2Qq_p/h}\right) \eta = c_{NC} - b_{NN} \qquad (4.3\text{-}6)$$

In Eq. 4.3-6 it is assumed that the population of the orbital involved in the NN bond is less than that in the NC bond. This difference is both chemically reasonable and consistent with ab initio MO calculations on HMX.[62]

The atomic coupling constant for a single p electron on a nitrogen atom, e^2Qq_p/h, has been taken to be 8.4 MHz although the exact value cannot be determined experimentally. Uncertainty in this value is of importance when absolute orbital populations are sought, but is not vital when making relative comparisons as will be done here. Nevertheless, Eqs. (4.3-5) and (4.3-6) still contain three unknowns, $a_{N\pi}$, b_{NN}, and c_{NC} but only two experimental observables, e^2Qq/h and η. An assumption about one of the unknowns must be made. If a value of 1.10e is chosen for c_{NC} based on previous NQR analyses,[33] then an indication of the σ and π character in the N-N bond can be deduced. The resulting values of $a_{N\pi}$ and b_{NN} are compiled in Table 4.3-IV. The higher coupling constant in HMX can be seen to be associated with a slightly higher population for the amine p_z orbital involved in the πNN bond, (i.e., less π character) and slightly lower population in the σ_{NN} bond, while the reverse is true of the lower coupling constant. The neutron diffraction data for β-HMX reveal[57] that the N-N bond is longer for the axial amines [1.373(5) Å] than the equatorial amines [1.354(5) Å]. Therefore, the larger coupling constant arises from the axial amines and the smaller value is due to the equatorial amines.

BLOCK ENGINEERING

TABLE 4.3-IV

THE HYBRID ORBITAL OCCUPATIONS OF THE AMINE NITROGEN ATOMS ASSUMING A POPULATION FOR THE N-C BOND OF 1.10 ELECTRONS AND THE NQR DATA AT 77°K

	$a_{N\pi}$	b_{NN}	c_{NC}
HMX			
$N_{2,2}$ (equatorial)	1.675	0.76	(1.10)
$N_{3,3}$ (axial)	1.69	0.73	(1.10)
RDX			
(average)	1.65	0.67	(1.10)

The difference in the axial and equatorial amine coupling constants may originate in the intermolecular interactions of the β-HMX lattice. An examination of the difference between the amine sites reveals that the axial $C_1N_3C_2$ fragment is engaged in a close interaction with an oxygen atom, O_3, of an axial NO_2 group in the neighboring molecule (Figure 4.3-3).[57,63] The carbon atoms C_1 and C_2 are electrostatically attracted to the neighboring O_3 atom while the amine nitrogen N_3 is repelled by it. This repulsion occurs in the electron region of N_3 and could be responsible for the slight lengthening of the axial NN bond relative to the equatorial NN bond, where no such intermolecular interactions takes place.

The six membered ring analog of HMX, known as RDX, has the stoichiometry $C_3H_6N_3(NO_2)_3$. The crystal contains three crystallographically inequivalent nitrogen atoms [64] which give rise to the NQR data in Table 4.3-II. The average of the coupling constants and asymmetry parameters may be used in conjunction with Eqs. 4.3-4 to 4.3-6 to calculate orbital populations assuming the same EFG axes as in HMX. If c_{NC} is held constant at 1.10e, the values of $a_{N\pi}$ and b_{NN} shown in Table 4.3-IV are obtained. $a_{N\pi}$ is slightly smaller in RDX than in HMX indicating that the amount of NN π-character is slightly greater in RDX. This conclusion is consistent with the larger value found for the ^{15}N ^{15}N coupling constant in RDX compound to HMX.[64] However, the value of b_{NN} is found to be less in RDX than HMX which is consistent with the slightly longer average N-N bond in RDX (1.38 Å)[65] compared to β-HMX (1.36 Å). Therefore, the trend in $a_{N\pi}$ compared to b_{NN} seems to be contradictory in RDX, yet each value finds support in the results of other experiments. It is certainly possible that the limits of the Townes-Dailey model have been reached as far as the NQR data are concerned. Additional work on this problem is planned.

BLOCK

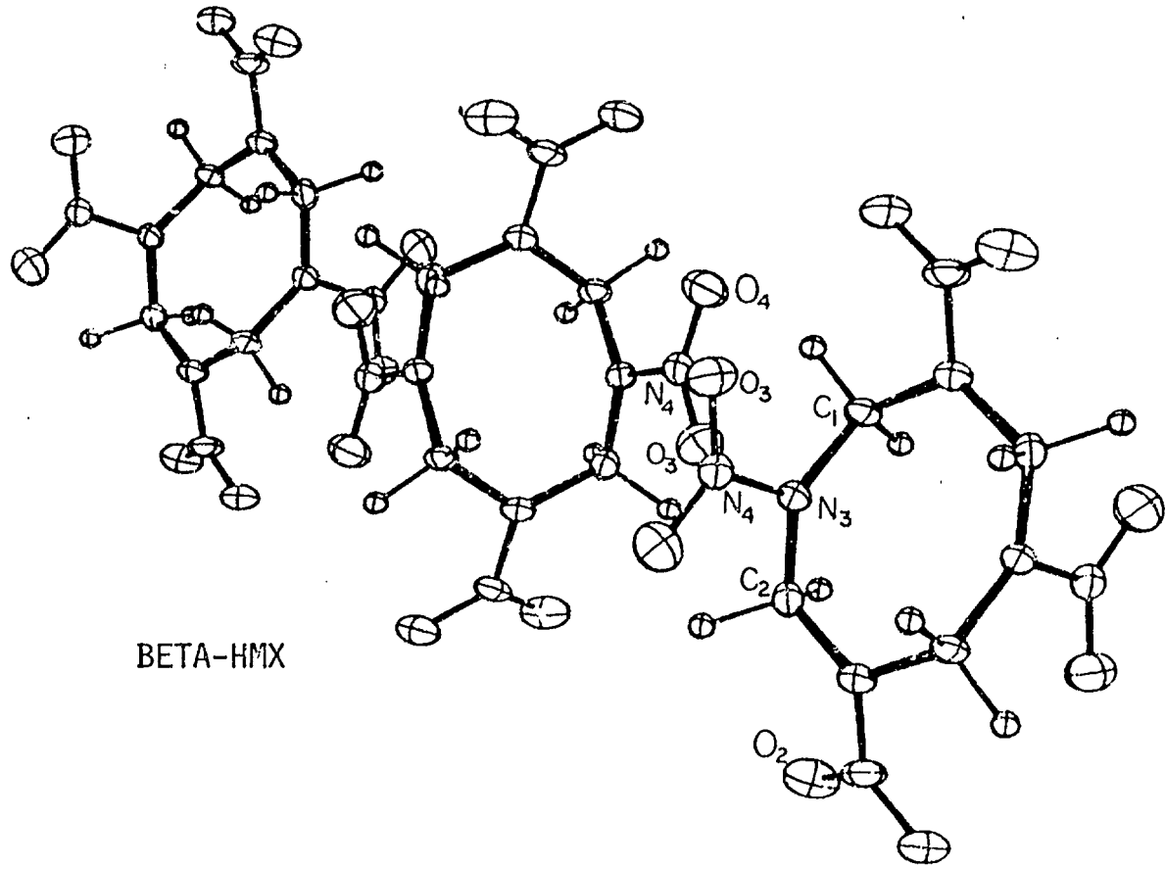

Figure 4.3-3. The primary intermolecular interaction in β-HMX. The O_3 atom of the axial NO_2 groups engages in an electrostatic attraction with C_1 and C_2 and a repulsive interaction with N_3 of a neighboring molecule.

BLOCK ENGINEERING

Molecular Motion: From the temperature dependence of the coupling constant for the axial and equatorial amine nitrogen atoms, one can deduce information about the nature of motion in HMX. The change in e^2Qq/h with temperature is shown in Figure 4.3-4. The often found slow decrease in the EFG with increasing temperature occurs in HMX. However, the temperature coefficients, $d(e^2Qq/h)/dT$, for the axial and equatorial amine sites are different. Three temperature regions exist where the coefficients at each site are reasonably constant. These are the 77-270°K, 270-370°K, and 370-420°K regions. Table 4.3-V gives the temperature coefficient values. Figure 4.3-5 graphically illustrates the much more rapid decrease in $d(e^2Qq/h)/dT$ at the equatorial amine sites compared with the axial site with increase in temperature. No first order phase transitions occur in HMX over this temperature range.

The temperature dependence of e^2Qq/h as well as its difference for the axial and equatorial amines originates in the temperature dependence of the librational motions of the molecule. These motions occur about the X,Y and Z EFG axes for each amine site.[66] When the torsional motions are described by an Einstein model, the root mean square of the amplitudes about the x, y and z inertial axes of HMX are expressed as a function of temperature according to eq.(4.3-7).

$$\langle\theta_i^2\rangle = \frac{h}{4\pi^2 I_i \nu_i}\left[1/2 + \frac{1}{\exp(h\nu_i/kT) - 1}\right] \; ; \; i = x,y,z \qquad (4.3\text{-}7)$$

BLOCK ENGINEERING

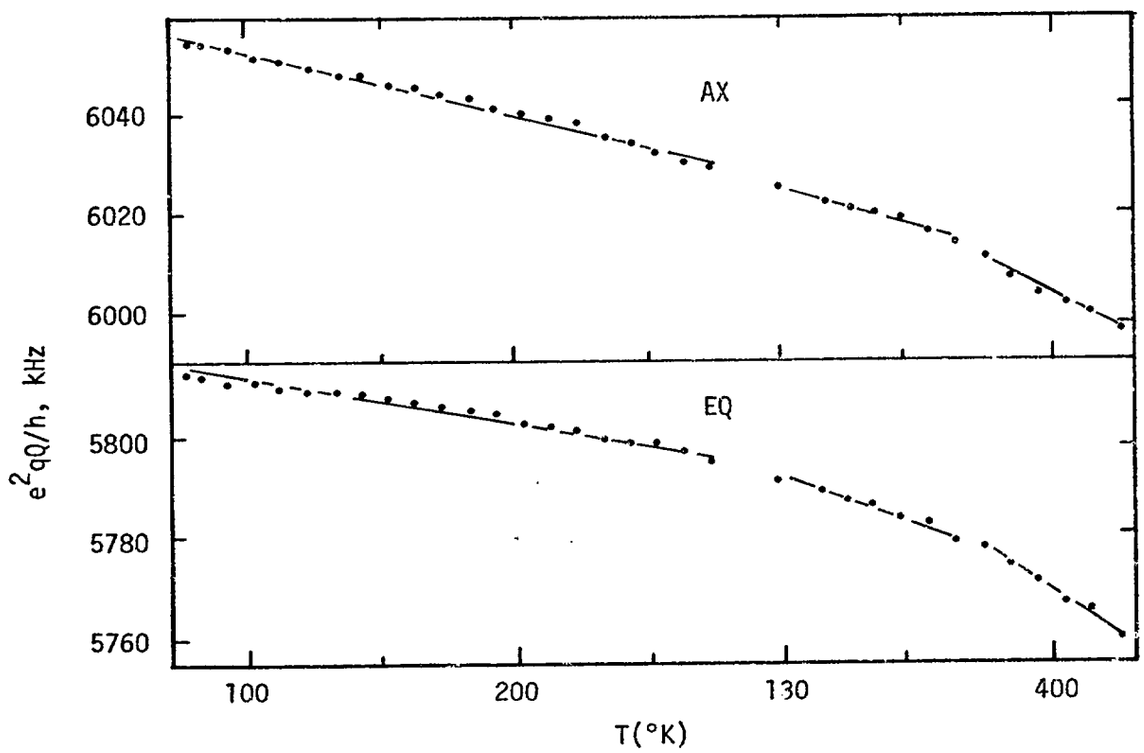

Figure 4.3-4. The Temperature Dependence of e^2Qq/h for the axial and equatorial amines of HMX. The three temperature regions where $d(e^2Qq/h)/dT$ is constant are indicated with the lines

TABLE 4.3-V

THE TEMPERATURE COEFFICIENTS FOR THE AXIAL AND EQUATORIAL AMINE ATOMS OF HMX. THE PARENTHETICAL NUMBERS ARE THE COEFFICIENTS OF CORRELATION OVER THE TEMPERATURE REGION GIVEN

Temperature Range, °K	$d(e^2Qq/h)/dT$, Hz/°K	
	Equatorial	Axial
77-270	-0.085(-0.988)	-0.127(-0.993)
270-370	-0.181(-0.990)	-0.158(-0.985)
370-426	-0.365(-0.992)	-0.262(-0.994)

BLOCK ENGINEERING

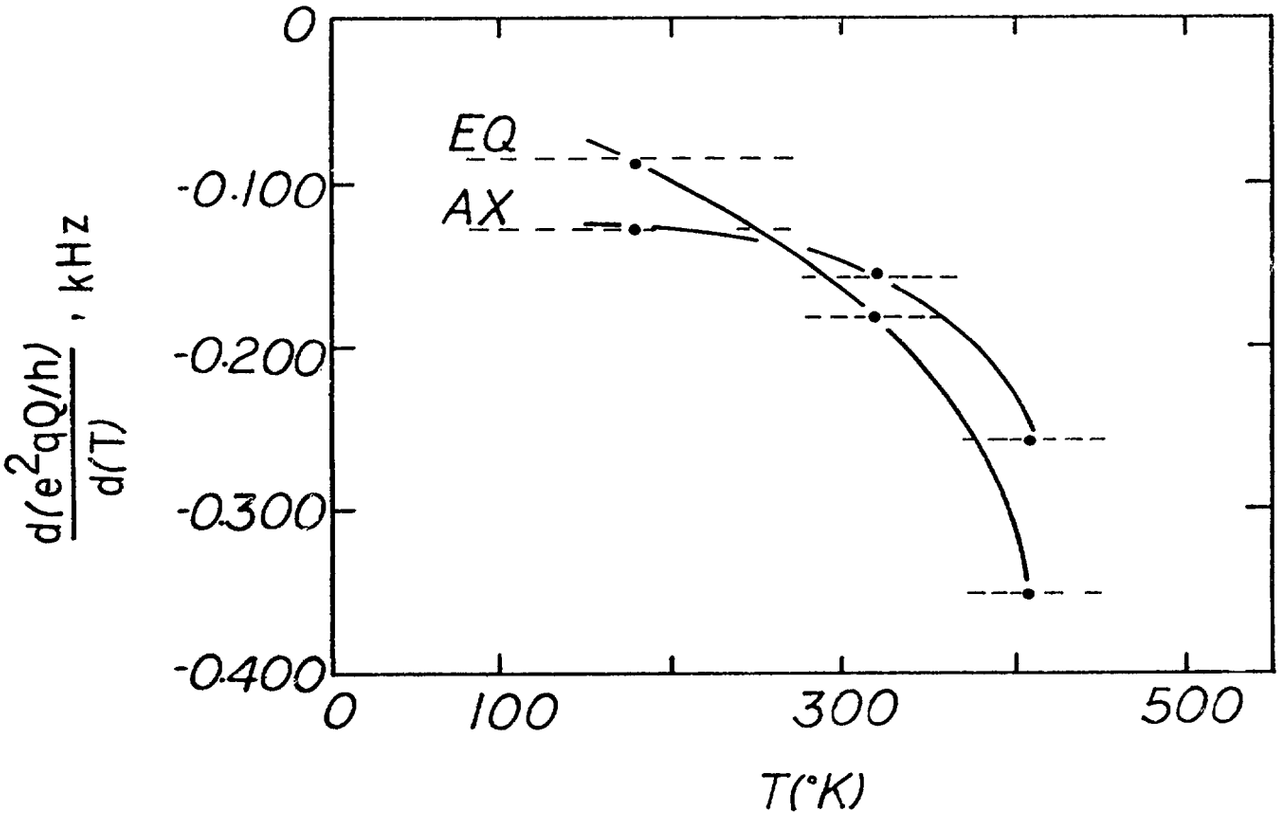

Figure 4.3-5. $d(e^2Qq/h)/dT$ for each HMX site shows greater temperature sensitivity at the Equatorial site than at the Axial site

I_i is the effective moment of inertia about the ith axis and ν_i is the librational frequency. To the extent that the principal axes of the inertial moment coincide with the EFG tensor principal axes, the change in the coupling constant and asymmetry parameter with temperature can be expressed in Eqs. 4.3-8 and 4.3-9.[44,45]

$$e^2Qq/h = e^2Qq_o/h \left[1 - \frac{3}{2}\left(\langle\theta_x^2\rangle + \langle\theta_y^2\rangle\right) + \frac{\eta}{2}\left(\langle\theta_y^2\rangle - \langle\theta_x^2\rangle\right)\right] \tag{4.3-8}$$

$$\eta = \eta_o \frac{e^2Qq/h}{e^2Qq_o/h}\left[1 - 1/2\left(\langle\theta_x^2\rangle + \langle\theta_y^2\rangle\right) + \frac{3}{2\eta}\left(\langle\theta_y^2\rangle - \langle\theta_x^2\rangle\right) - 2\langle\theta_z^2\rangle\right] \tag{4.3-9}$$

It can be seen from Eq 4.3-8 that librational oscillations about the Z axis will hardly affect the coupling constant. Therefore, e^2Qq/h is mostly a function of librational motion about all three EFG axes. The inertial moment axes in HMX can be calculated by using the atomic coordinates taken from neutron diffration data [57] based on the convention: $I_z > I_y > I_x$. The values of I in HMX are found to be $I_x = 149.7$, $I_y \doteq 277.9$, and $I_z = 374.2$ in units of amu $Å^2$. The origin of I lies at the molecular inversion center. The EFG axes deduced in the preceding section do not precisely coincide with these inertial axes, but there is qualitative coincidence between the two axis systems shown in Figures 4.3-1 and 4.3-2.

BLOCK ENGINEERING

One can consider the z inertial axis in order to illustrate the effect on the EFG of motion about an inertial axes. For the axial amines, the Z axis of the EFG is approximately parallel to the z inertial axis, while the X and Y EFG axes are approximately perpendicular to it. For the equatorial amines, the Y EFG axis approximately coincides with the z inertial axis while the X and Z EFG axes are perpendicular to it. Therefore, motion about the z inertial axis causes θ_x and θ_y to be larger than θ_z for the axial amines, while θ_y and θ_z are larger than θ_x for the equatorial amines. θ_x, θ_y, and θ_z refer here to librational motion about the X, Y, and Z EFG axes. By using Eqs. (4.3-8) and (4.3-9) one can reason that motion about the z inertial axis makes $d(e^2Qq/h)/dT$ larger for the axial site than for the equatorial site. Similar reasoning suggests that motion about the y inertial axis affects the temperature coefficient of the axial and equatorial sites in approximately the same way while motion about the x inertial axis should lead to $[d(e^2Qq/h)/dT]_{Equatorial} > [d(e^2Qq/h)/dT]_{Axial}$.

A scheme for the motion in HMX as the temperature increases toward the phase transition to δ-HMX at 436°K can be extracted from these data. In the low temperature domain (70-270°K) the lattice is quite rigid but some librational oscillation about the z inertial axis is consistent with the observed relative values of the temperature coefficients. This motion does not represent rotation of the molecule, but only libration. However, it is worthy of note that motion about this axis occurs in flat molecules like benezene[67] and s-triazine[68] which bear a resemblance in shape to β-HMX.

BLOCK ENGINEERING

As the molecule passes through the room temperature region, the importance of motion about the x (and perhaps y) inertial axes appears to become increasingly important and causes the temperature coefficient of the equatorial amines gradually to surpass that of the axial amines. In the higher temperature domain approaching the β→δ-HMX phase transition, oscillations about the x inertial axis appear to dominate.

The motion about both the x and y axes represents oscillation about the pivot formed by the most important intermolecular electrostatic interaction in crystalline β-HMX: the contact between an oxygen atom of a neighboring molecule and the $C_1N_2C_2$ fragment in the axial portion of the molecule shown in Figure 4.3-2. This interaction leads to a chain-like structure in the β-HMX lattice (Figure 4.3-6)[63] which occurs approximately along the z inertial axis of the HMX molecule. Pivoting of the molecule about this axis interaction would yield a larger temperature coefficient in the low temperature region for the axial amines compared to the equatorial amines. As the lattice approaches the phase transition to δ-HMX, libration about the x inertial axis takes place. Like the z axis libration, this motion involves a type of pivoting about the interaction but is more disruptive of the interaction. Such an analysis does not preclude the possiblity that other motions in HMX are important as well, particularly because the ring conformation must also change during the phase transition. However, disruption of the most important cohesive interactions is a prerequisite to the β→δ transition in HMX and this is found to take place.

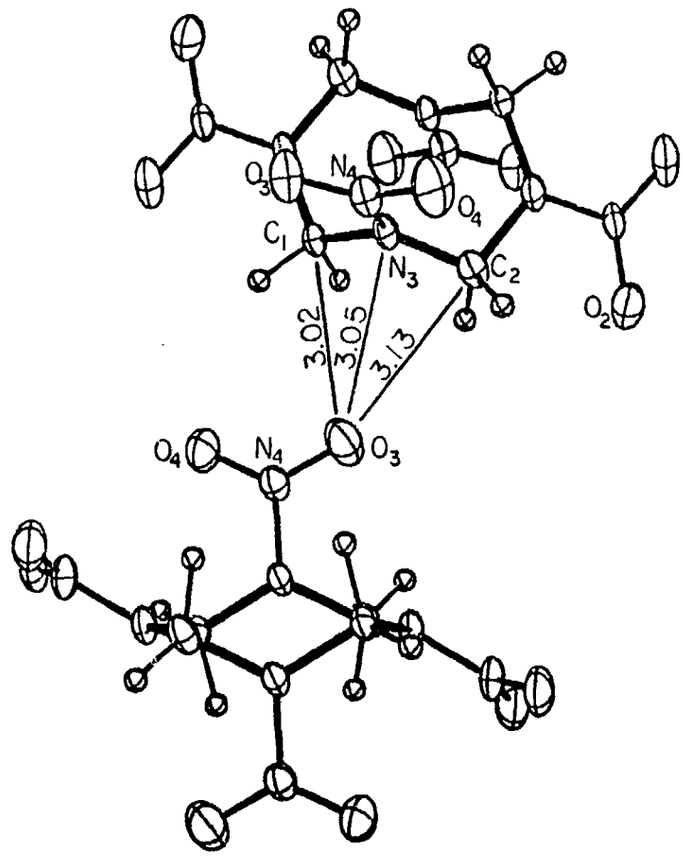

BETA-HMX

Figure 4.3-6. A view along the "chains" of ß-HMX molecules which form as a result of the interaction shown in Figure 4.3-3. Oscillations of the molecules along this chain are primarily responsible for the changes in $d(e^2Qq/h)/dT$ with temperature.

BLOCK
ENGINEERING

The results presented here leave little doubt that the most important crystal stablizing interaction in β-HMX both in terms of electrostatic energy[63] and molecular dynamic motion is the O...CNC interaction between the axial NO_2 groups in neighboring HMX molecules.

5.0 CONCLUSIONS AND RECOMMENDATIONS

A summary of the specific results obtained during this program is given in Section 1.2. Here we list some additional conclusions we reached as a result of this work:

a) Fourier transform and pulse NQR techniques proved to be sufficiently sensitive to detect, with adequate resolution, the ^{14}N NQR spectrum of TNT at all temperatures of interest.

b) Efforts to detect the very weak TNT lines over the last five years resulted in the development of new excitation sequences, i.e. the multiple pulse SLSE and SORC sequences, and in improved FT methods.

c) It has become possible to detect the presence or absence, as well as the relative abundance of orthorhombic and monoclinic TNT in a given volume of space.

Although this program enjoyed considerable success, further work along the following lines would still be useful to a more nearly complete understanding of the structure and bonding of TNT:

a) Measurement of the TNT spectrum at liquid helium temperatures would give a firmer foundation to the determination of the librational motions of the TNT nitro groups. Similarly, to study the spectrum and the relaxation times up to the melting point might be very useful in understanding the thermal decomposition of the molecule.

b) The complex $(TNT)_2 \cdot HNS$ which has been identified as the nucleating agent for growth of the stable (monoclinic) phase of TNT from the melt, is currently of unknown structure and conformation. An NQR study of structure and bonding in this system would be invaluable, and would complement any eventual x-ray structure determination.

BLOCK ENGINEERING

6.0 ACKNOWLEDGEMENTS

The authors would like to thank our technical monitor Dr. Charles Boghosian, for his support during the tenure of this project and Dr. Frank Owens for his continued interest and encouragement during the course of this work. Dr. Stanley M. Klainer is acknowledged as the man without whose efforts the original proposal would never have been written.

Finally, one of us (RAM) would like to thank the management and staff of Block Engineering for the warm hospitality they extended to him while he served as principal investigator for this project.

APPENDIX A
NQR THEORY

A.1 INTRODUCTION

The technique of NQR developed as an outgrowth of the discovery of NMR in the late forties. The theory of nuclear quadrupole interaction in solids was first given by R.V. Pound at Harvard in 1950, and later that year Dehmelt and Kruger in Germany observed the NQR signal from the chlorine-35 (Cl^{35}) nucleus in transdichloroethylene. In the following year Watkins and Pound detected the first quadrupole resonance from Nitrogen-14 (^{14}N) in HMT (hexamethylenetetramine), BrCN and ICN. Experimental difficulties delayed the utilization of the NQR and until the late sixties only a few compounds were studied. Two chief difficulties arise in ^{14}N:

(1) the low frequency range of the resonance lines (0.5 to 5 MHz) which makes them weak and hard to detect, and

(2) the unusually strong intermolecular interactions which are characteristic in nitrogen-containing compounds preclude on one hand the proper transfer of radio-frequency energy to the crystalline lattice, and on the other hand make the electric field gradient very sensitive to the purity and crystallinity of the material.

This results in transitions which are easily saturated and lines which are too broad to be detected with conventional (cw) spectrometers. With the development of pulsed methods and more sensitive spectrometers these difficulties can be overcome. At the present time ^{14}N NQR is successfully being applied using the Block Engineering, NQR/FFT Spectrometer.

A.2 BASIC CONCEPTS OF NQR

In order to understand the origin of nuclear quadrupole resonance, we may visualize a nucleus as a classical distribution of positive charges, $\rho_N(\vec{r})$, over a volume of characteristic linear dimensions of the order of nuclear radii: 10^{-13}cm (Figure A-1). A charge cloud extending over a volume of linear dimensions of the order of several Angstroms generates an electrostatic potential $\phi(\vec{r})$ which can be considered as varying slowly over the region occupied by the nucleus. The electrostatic energy of the system expressed as

$$W = \int \rho_N(\vec{r})\phi(\vec{r})d\vec{r} \qquad \text{(A-1)}$$

can then be expanded in terms of the moments of the nuclear charge distribution:

$$W = \phi(0)q_N + \vec{p}\cdot\vec{E}(0) - \frac{1}{6}\sum_{ij} q_{ij}Q_{ij} + \ldots \qquad \text{(A-2)}$$

where

q_N	$= \int \rho_N(\vec{r})d\vec{r}$	nuclear charge
$\vec{P}$	$= \int \rho_N(\vec{r})\vec{r}\, d\vec{r}$	dipole moment vector
Q_{ij}	$= \int \rho_N(\vec{r})x_i x_j d\vec{r}$	quadrupole moment vector
E	$= -\vec{\nabla}\phi$	electric field vector
q_{ij}	$= \partial E_i/\partial x_j$	electric field gradient tensor

BLOCK
ENGINEERING

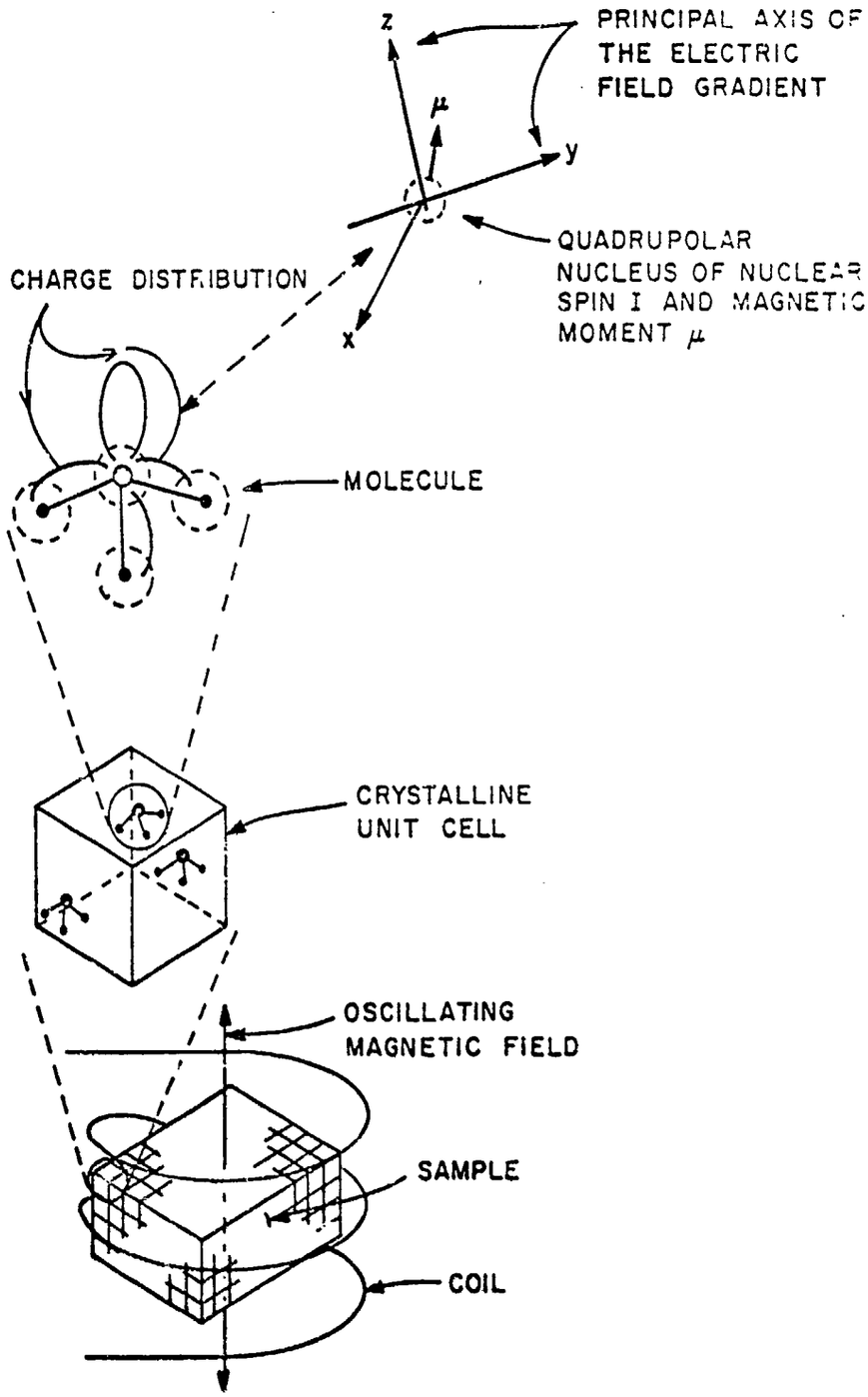

Figure A-1
Origin of the NQR Interaction.

From quantum mechanical considerations it can be proven that the only non-vanishing terms in (2) are the first and third ones. Then, if the energy of the system is referred to the constant first term:

$$W_Q = -\left[W + \phi(0) q_N\right] = \frac{1}{6} \sum_{ij} q_{ij} Q_{ij} \qquad \text{(A-3)}$$

Q_{ij} is diagonal and is related to the components of the nuclear spin I_i according to

$$Q_{ij} = \frac{eQ}{I(2I-1)} \left[3I_i^{\,2} - I(I+1)\right] \qquad \text{(A-4)}$$

where $I = \left(\sum I_i^{\,2}\right)^{\frac{1}{2}}$ and eQ is defined as the nuclear quadrupole moment. Since

$$\sum_i q_{ij} = 0 \text{ (Laplace equation: } \Delta\phi = 0)$$

the quantum mechanical expression of the quadrupole energy (the Hamiltonian) takes the particular simple form:

$$H_Q = \frac{eQ}{2I(2I-1)} \sum_i q_{ij} I_i^{\,2} \qquad \text{(A-5)}$$

which can also be expressed in the following way:

$$H_Q = \frac{e^2qQ}{4I(2I-1)} \left[(3I_z^{\,2} - I^2) + \eta(I_x^{\,2} - I_y^{\,2})\right] \qquad \text{(A-6)}$$

where e^2qQ is defined as the quadrupole coupling constant of the system and η is defined as the asymmetry parameter of the electric field gradient (EFG):

BLOCK ENGINEERING

$$\eta = \frac{q_{xx} - q_{yy}}{q_{zz}}$$

$$e^2qQ = (eQ)(eq_{zz}) \qquad \text{(A-7)}$$

where

$|q_{zz}| > |q_{yy}| > |q_{xx}|$ by convention.

For nitrogen-14, of nuclear spin I = 1, the solution of the Schroedinger equation $H_Q \psi_N = E\psi_N$, where ψ_N is the nuclear wave function can be shown to lead to a three level system of energies given by

$$E_z = e^2qQ/2$$

$$E_x = E_z(1-\eta)/2 \qquad \text{(A-8)}$$

$$E_y = E_z(1+\eta)/2$$

Transitions between these levels can be induced with oscillating magnetic fields of the proper (resonant) frequencies. The frequencies of these transitions are (see Figure A-2)

$$\nu_+ = \frac{e^2qQ}{4h}(3+\eta)$$

$$\nu_- = \frac{e^2qQ}{4h}(3-\eta) \qquad \text{(A-9)}$$

$$\nu_d = \frac{e^2qQ}{2h} \quad \nu_+ - \nu_-$$

BLOCK ENGINEERING

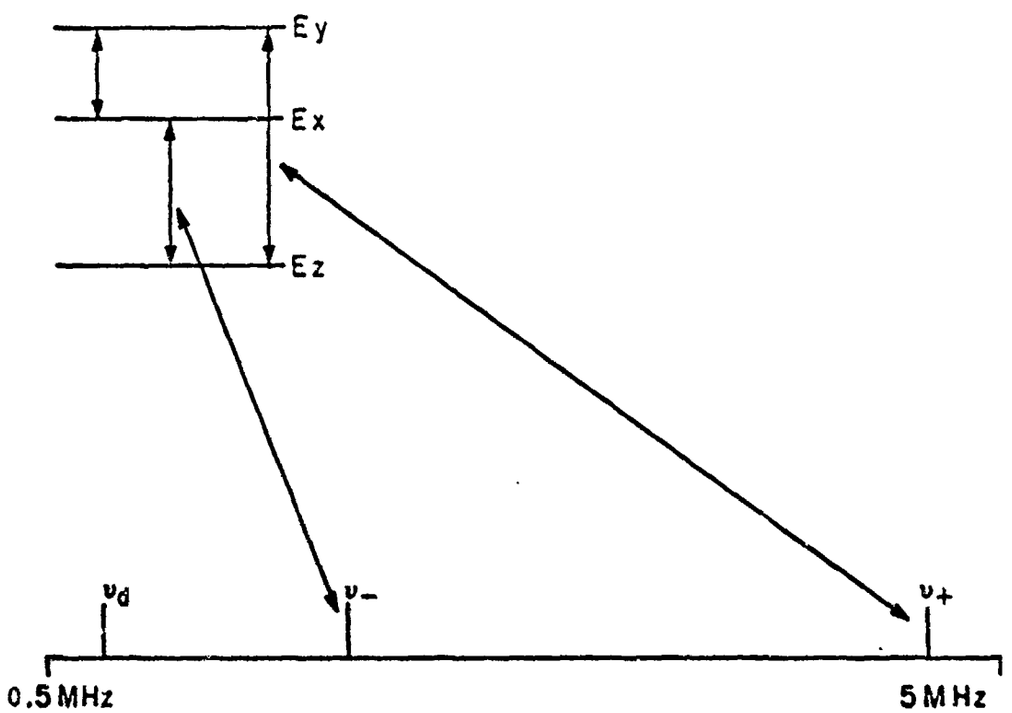

Figure A-2

Energy Level Diagram for ^{14}N NQR.

Conversely, determining any two of the three NQR frequencies completely describes the EFG in the vicinity of the nitrogen nucleus:

$$e^2qQ = \frac{2}{3}(\nu_+ + \nu_-) = \frac{2(\nu_+ - \nu_-)}{e^2qQ} \qquad \text{(A-10)}$$

Experimental techniques for the determination of NQR spectra can be divided into three categories:

(a) Continuous-wave (cw) methods
(b) Transient methods
(c) Double resonance techniques

CW methods have enjoyed great popularity for they are simple and inexpensive. The limitations of these techniques are so severe, however, that at least in the Nitrogen-14 NQR field they are rarely used any more. Transient methods include the superregenerative technique, which, for Nitrogen-14 is bad and rarely used, and pulsed methods that monitor the resonance of one type of nuclear species while another is being perturbed. Even though transient methods are extremely sensitive they do not have as high a resolution as pulsed FT methods, and are not the method of choice for this particular study.

The Nitrogen-14, pulsed techniques that operate in the so called spin-echo mode are particularly good (for other nuclei the reverse holds true, and CW or superregenerative methods are better).

To understand the reasons for this advantage let us begin by defining some basic magnitudes that describe an NQR line. In the frequency domain an NQR line is fully described by its frequency and by a normalized shape function S(w). For example:

$$S(w) = \frac{2}{\pi \Delta w} \frac{1}{1 + \left(\frac{w - wo}{\Delta w}\right)^2} \qquad \text{(A-11)}$$

Spin-echo techniques operate in the time domain, there are three parameters that fully describe an NQR absorption line

(a) Spin-lattice relaxation time(T_1). A magnitude which establishes the typical "waiting" time to observe a resonance a second time.

(b) Spin-spin relaxation time. (T_2). A magnitude which establishes the time scale for the observation of spin-echoes.

(c) A spin-echo shape function G(t). The "width" of this function is defined as $2T_2^*$. G(t) is the fourier transform of the line shape function S(w), thus $T_2^* \alpha \frac{1}{\Delta w}$.

CW and superregenerative methods are poor techniques for Nitrogen-14 because of the generally large T_1 and large Δw values associated with an NQR line (to avoid saturation in CW the level has to be reduced to very small values). Broad lines, a very common occurrence with Nitrogen-14, are weak since their areas are constant. Spin-echo methods are, on the other hand, unaffected by long T_1 values and since G(t) and S(w) are related by a Fourier transformation the equality

BLOCI
ENGINEERING

$$G_{MAX} = \int_{0}^{\infty} S(w)\ dw = 1 \qquad \text{(A-12)}$$

holds (Figure A-3). Thus, broad lines in the frequency domain do not affect the maximum intensity of the echo signal. In addition, pulsed methods for Nitrogen-14 are particularly advantageous because T_2 times are generally long (of the order of milliseconds). This is a result of the "spin-quenching" effect for $\eta \neq 0$ which substantially reduces spin-spin interactions.

The Nitrogen-14 NQR spectrum of a molecular system is determined by placing about 25 grams of sample inside the inductor of a resonant circuit which is then subjected to a series of radio frequency pulses of frequency, f. Whenever the frequency of these pulses satisfies the resonance condition $f = \nu_Q$ (where ν_Q is one of the quadrupole frequencies) absorption of energy takes place and is retransmitted as a series of signals as is shown schematically in Figure A-4. Therefore, by monitoring and detecting the transmitted signals as a function of the frequency of the pulses, the energy levels of the quadrupole nucleus are completely determined.

Since a narrow RF pulse has a Fourier spectrum of finite width, the pulse frequencies can be varied in discrete steps (5-10 kHz) so as to cover a larger frequency range for a given observation time. In this manner the total frequency range is only limited by the "waiting period" between successive observations. This waiting period depends on the spin lattice relaxation time (T_1) of the particular compound which is being investigated. This can be quite long (5-10 min.) for Nitrogen-14 NQR.

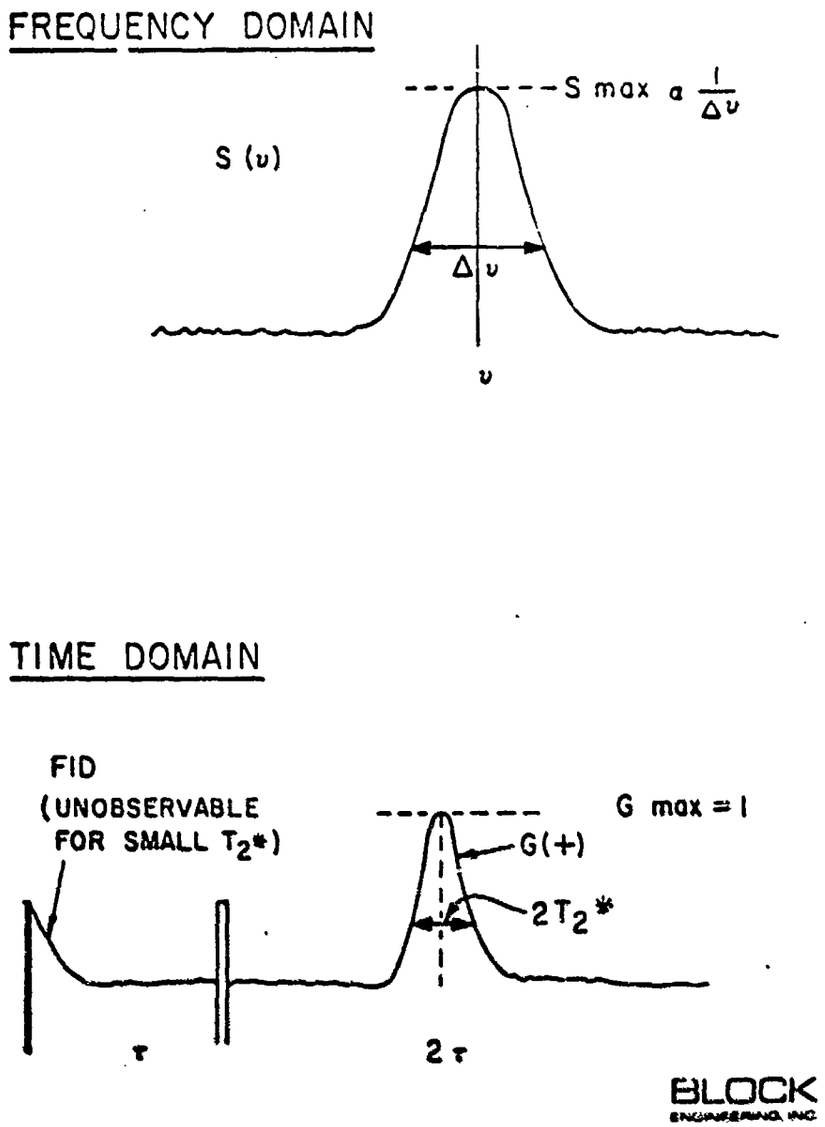

Figure A-3

Pulsed NQR Signals and Nomenclature

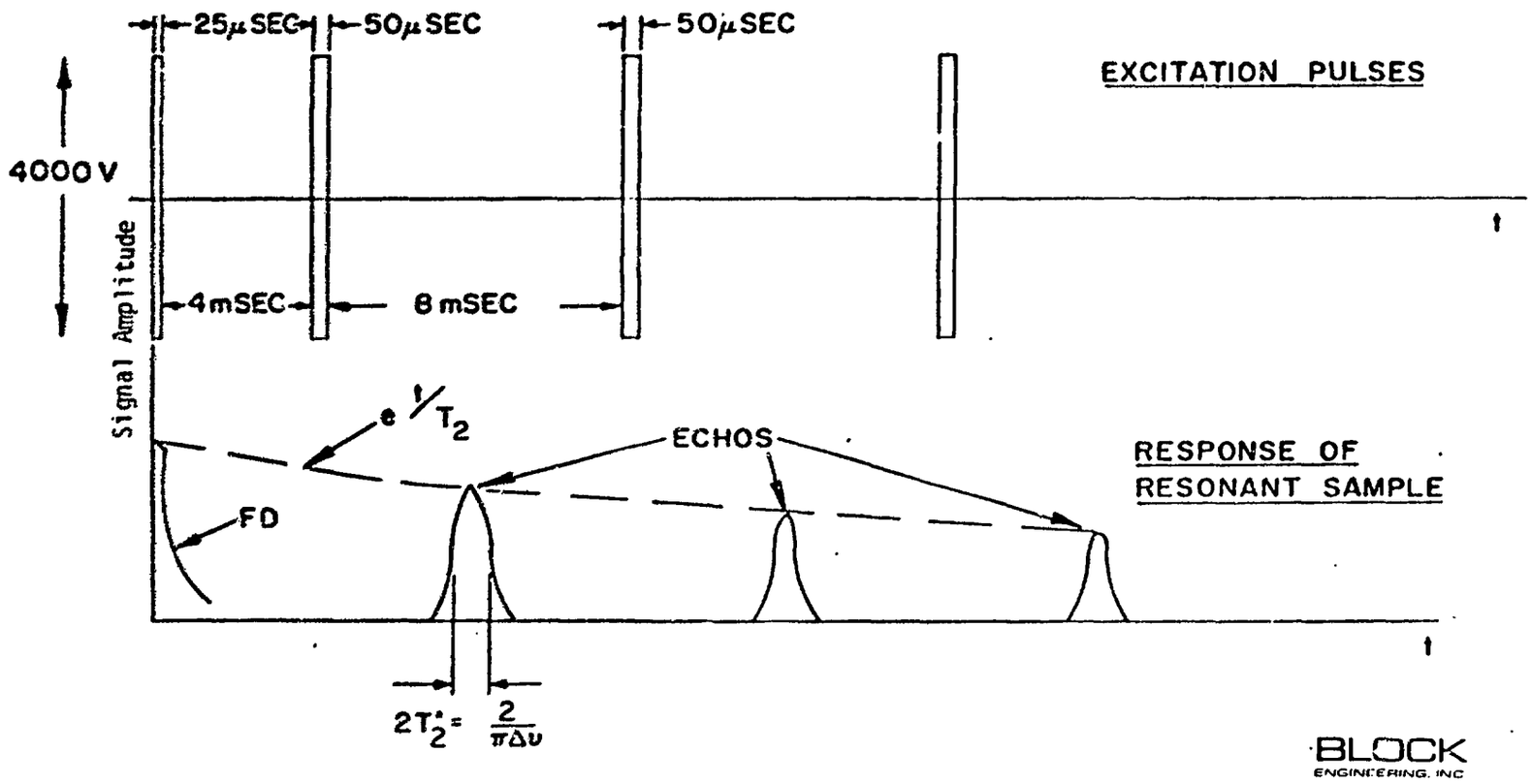

Figure A-4

Typical ^{14}N Pulse Sequence

APPENDIX B

TNT SPECTRA

B. 1 LIBRARY OF TNT SPECTRA

In this section we collect a library of TNT spectra to provide a record of the Nitrogen-14 NQR lineshapes. The legend of each plot gives the crystal phase of the TNT sample, the temperature (77°K) and the number of coherently added echo signals obtained in spin-locked spin-echo (SLSE) experiment.

Each plot consists of the time-domain NQR signal displayed at the top, and the modulus Fourier transform of the echo signal displayed at the bottom. Before computation of the transform, SORC-type signals seen at the beginning and end of the time=domain data (see Section 2.1) were apodized by multiplication with a "box car" function. Thus, only the center signal (the spin-echo) was transformed.

The caption under each graph lists:

a) The date on which the plot was made and a plot sequence number

b) The TNT phase

c) The reference frequency (zero on the plot scale)

d) Sample temperature

e) The number of echos coadded.

BLOCK ENGINEERING

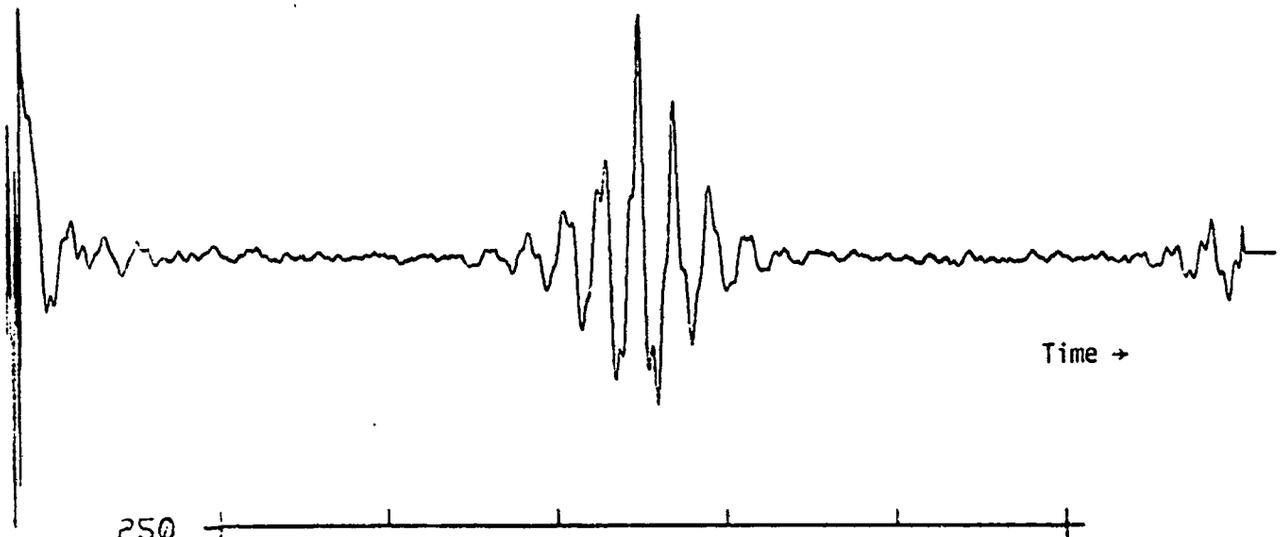

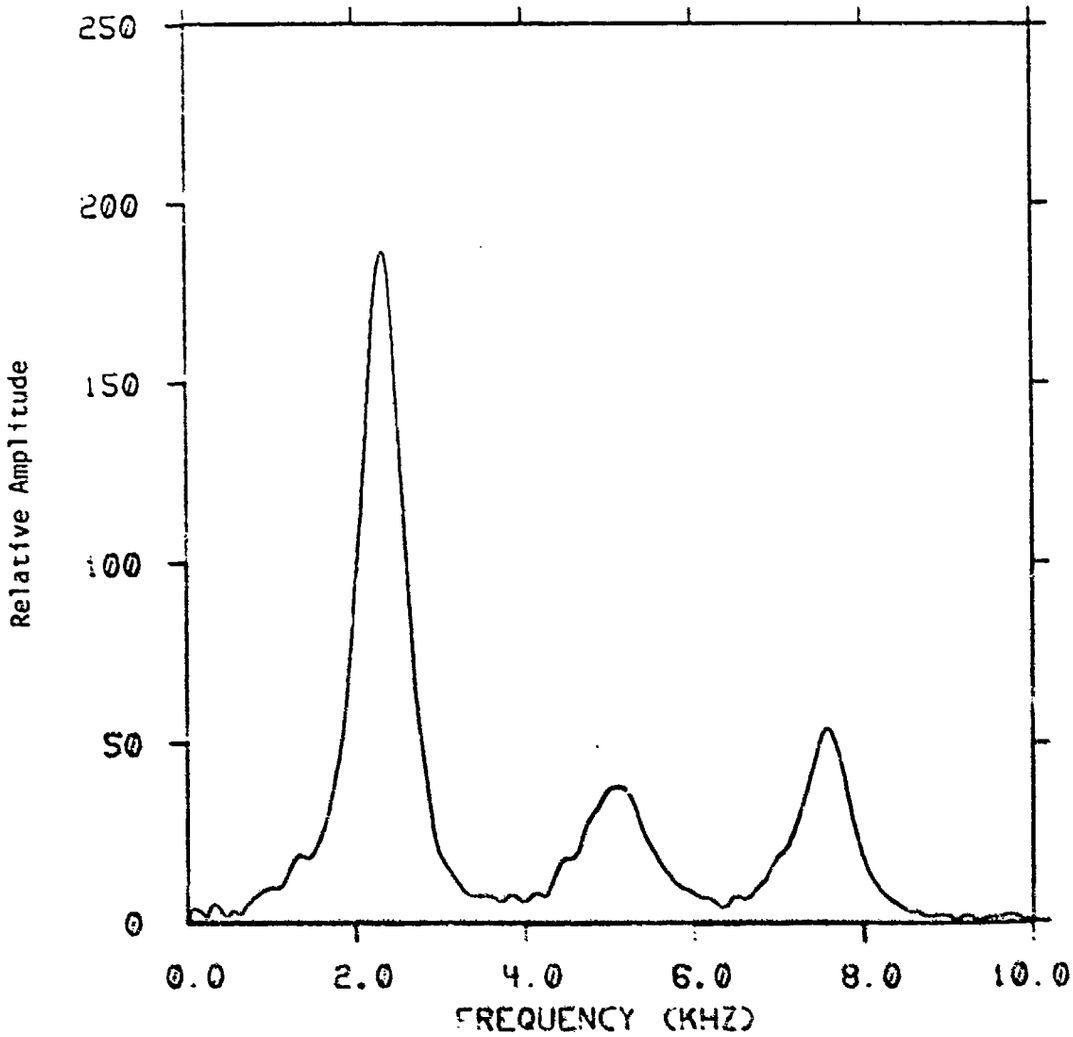

9-5/1 ORTHO 725.0KHZ 77K NSS=24000

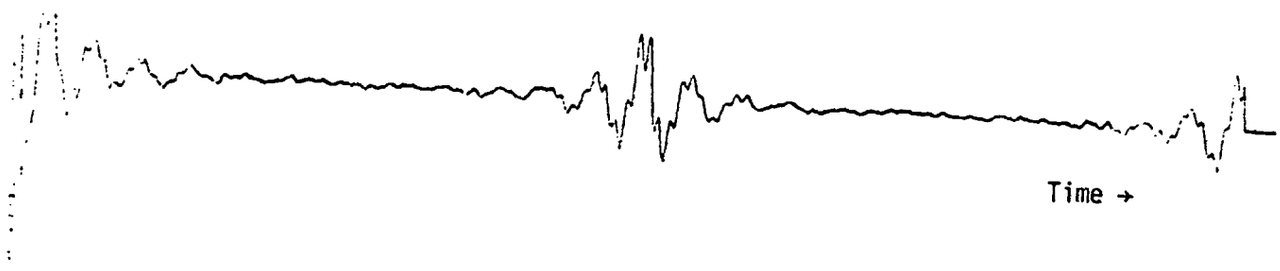

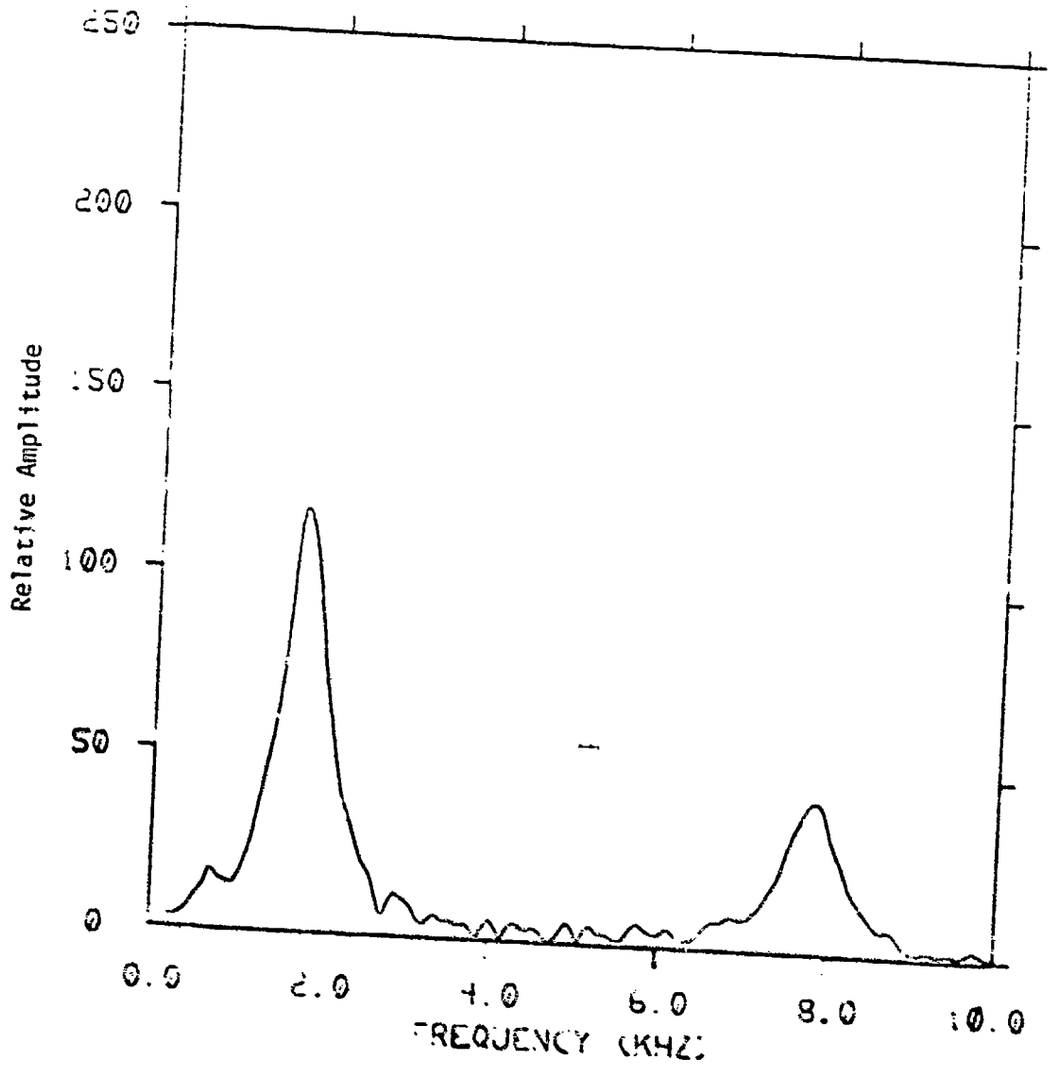

9-5/17 4040 900.0KHZ 77K NSS-24000

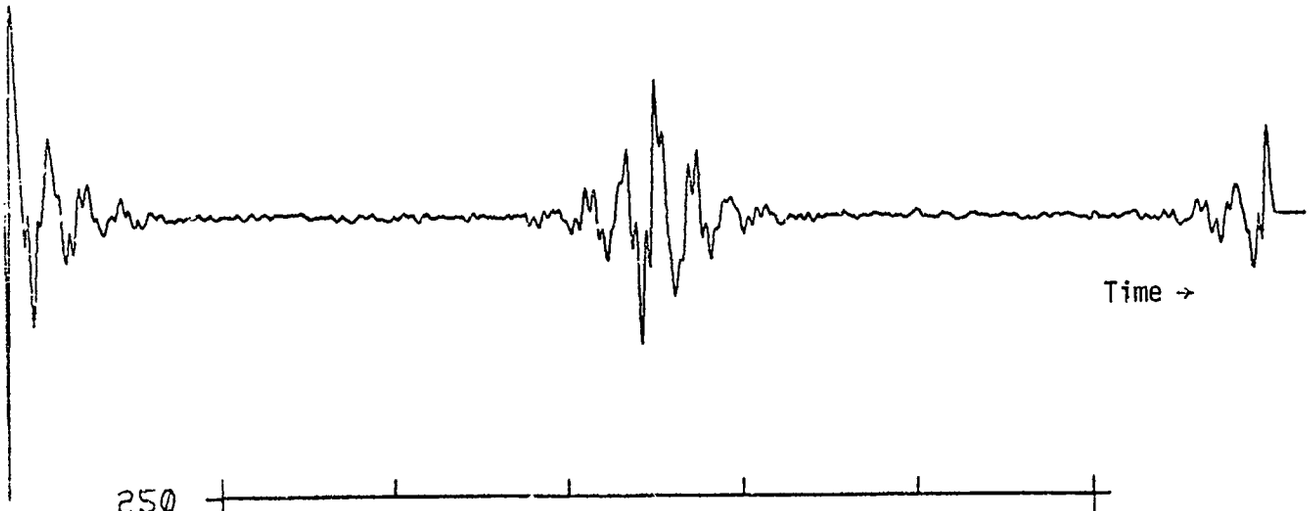

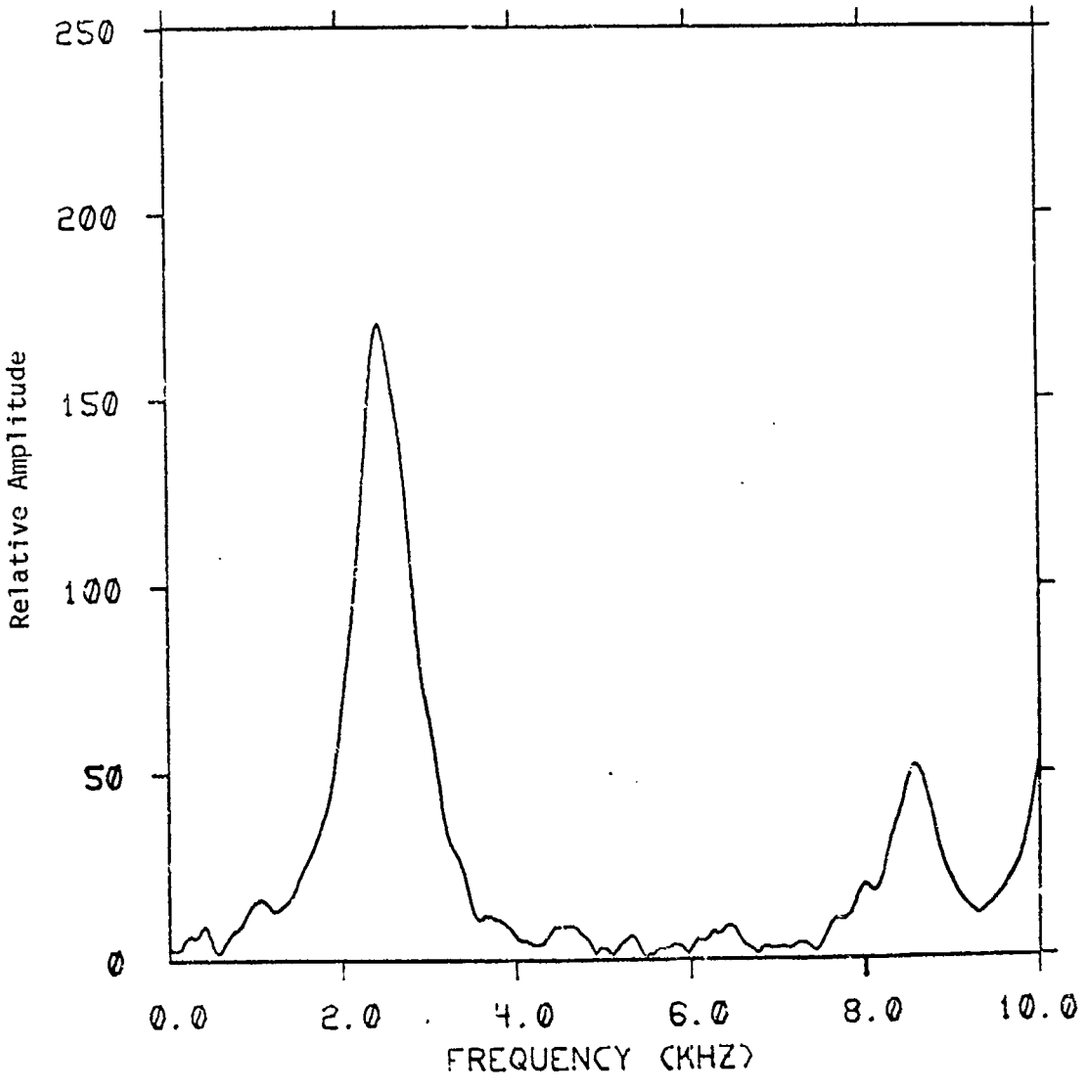

9-5/16 MONO 878.0KHZ 77K NSS=24000

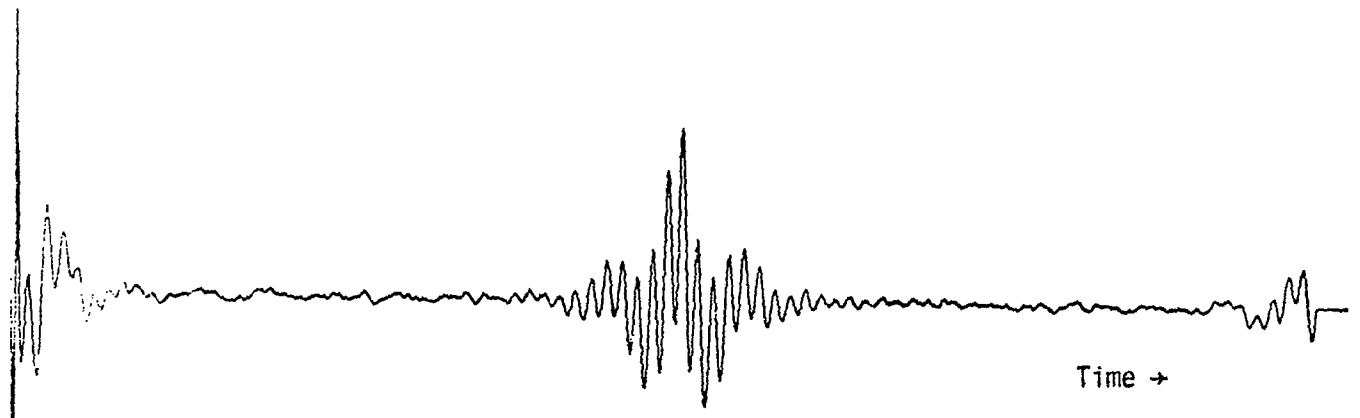

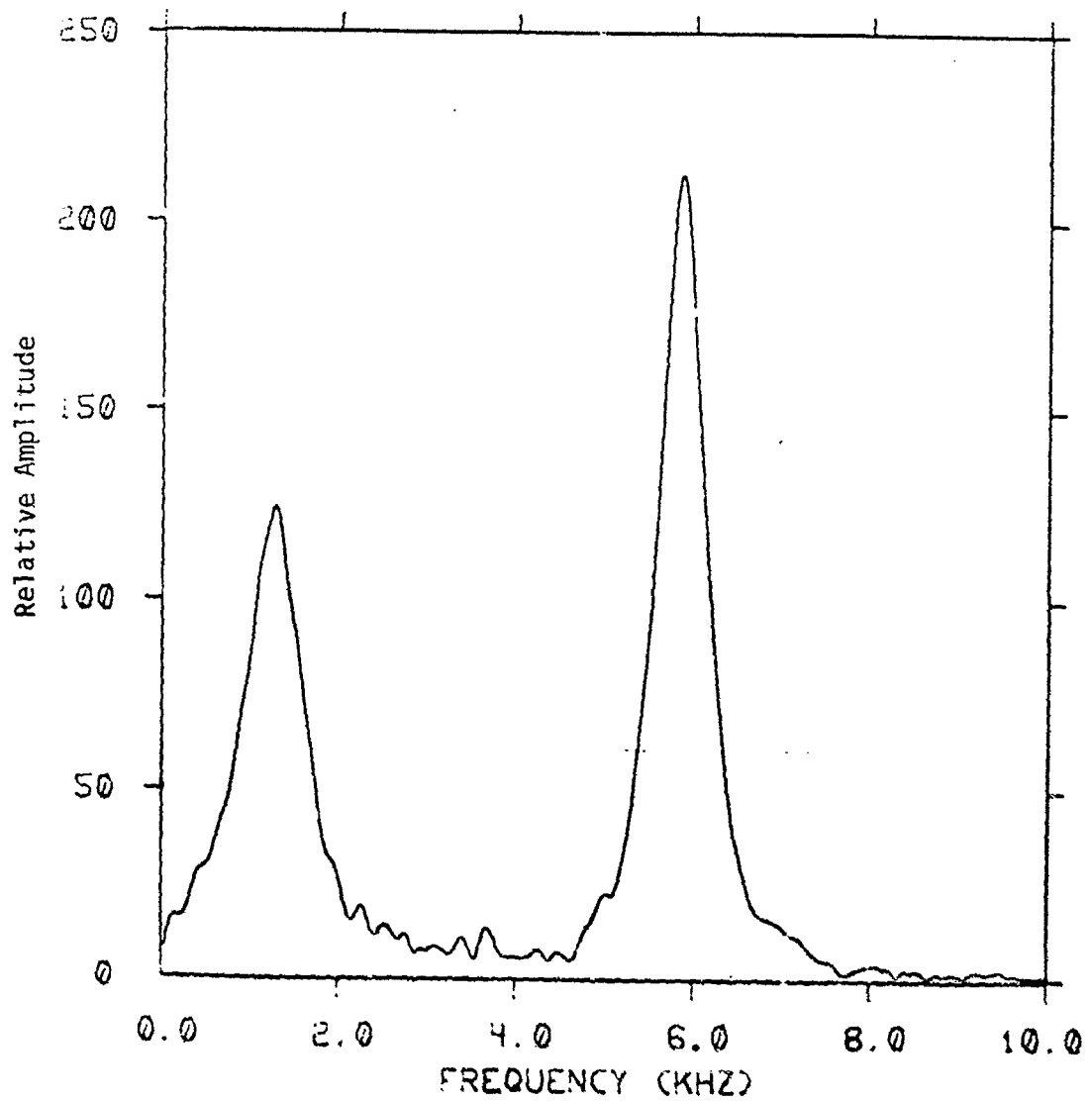

9-5/15 MONO 894.0KHZ 77K NSS=24000

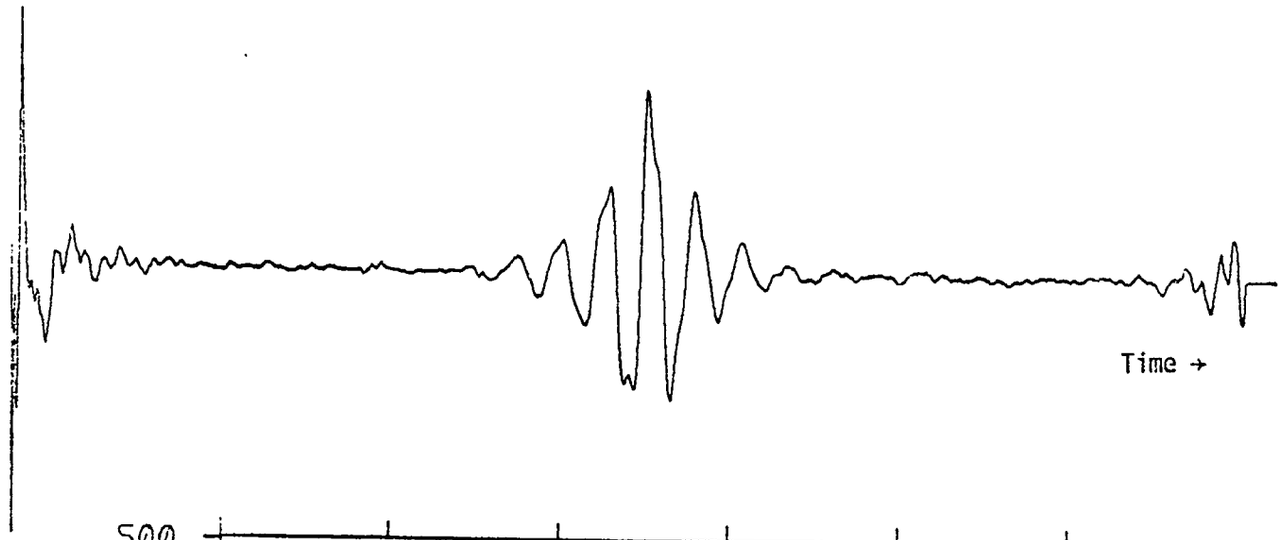

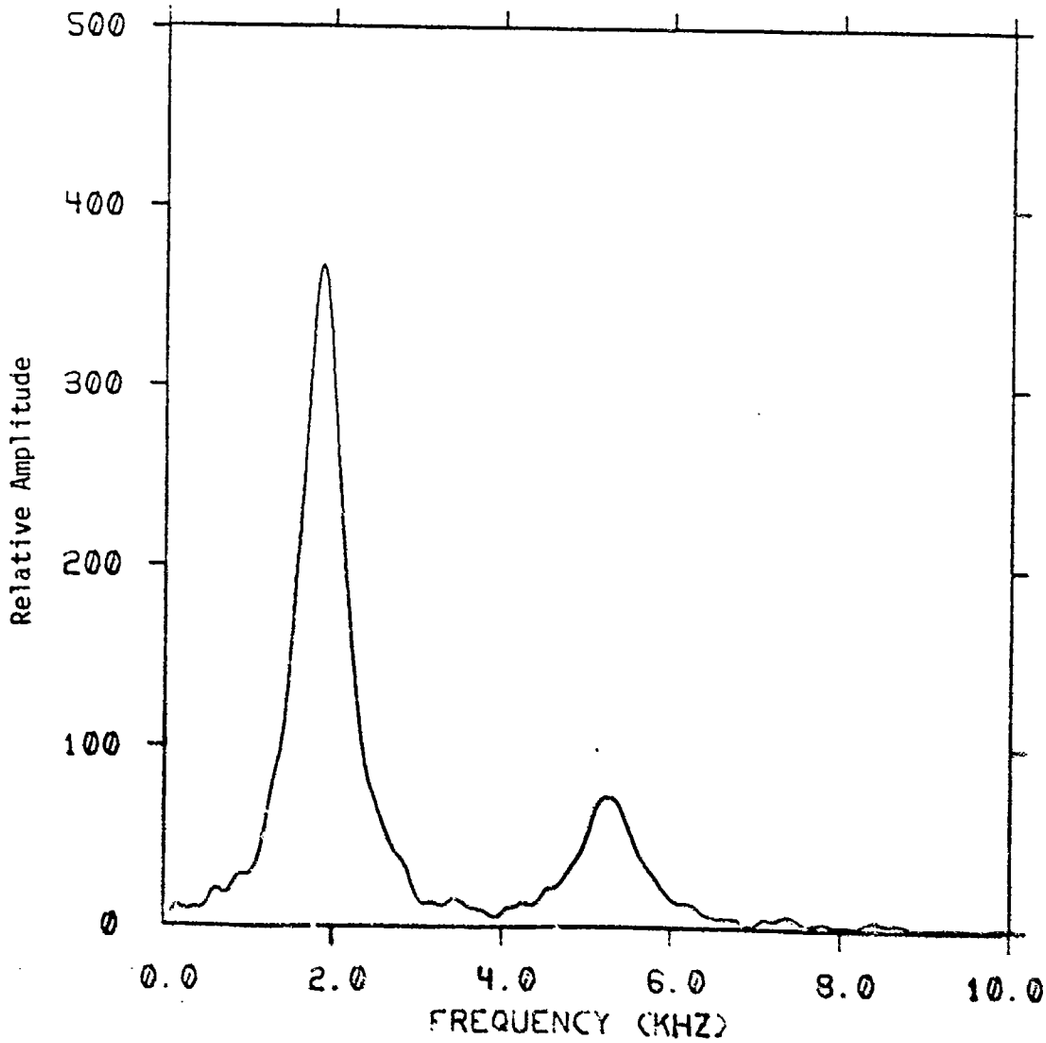

9-5/14 MONO 890.0KHZ 77K NSS=24000

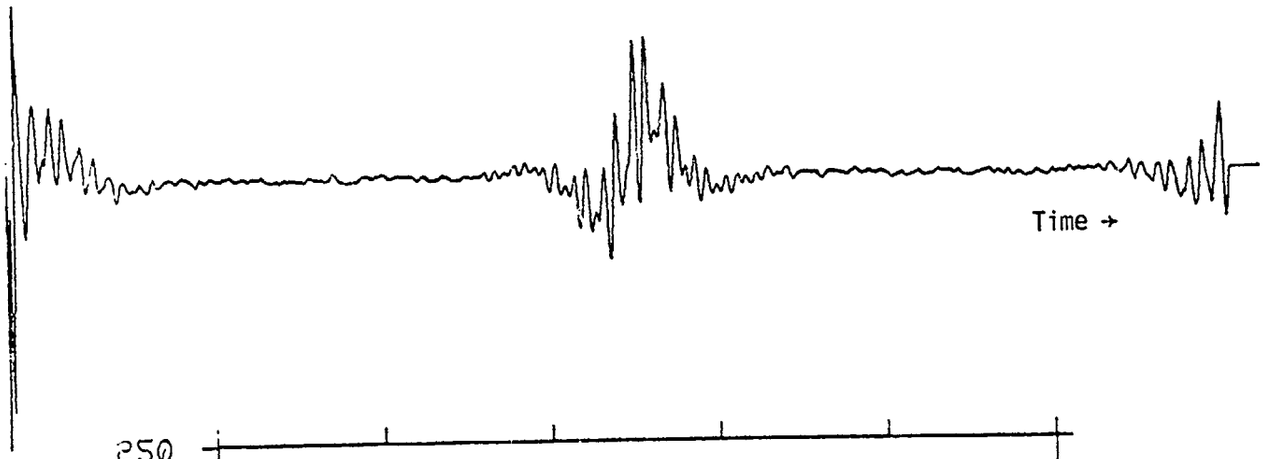

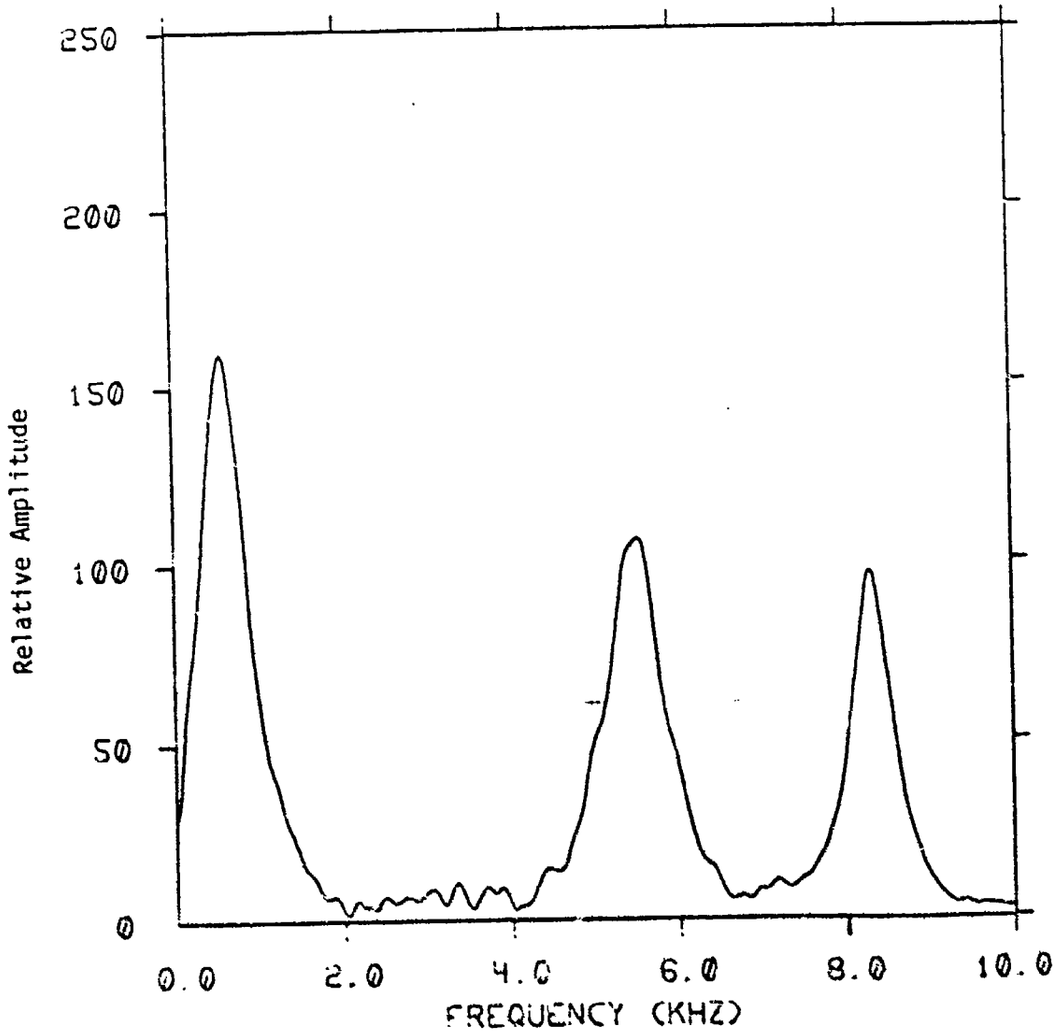

9-5/13 MONO 870.0KHZ 77K NSS=24000

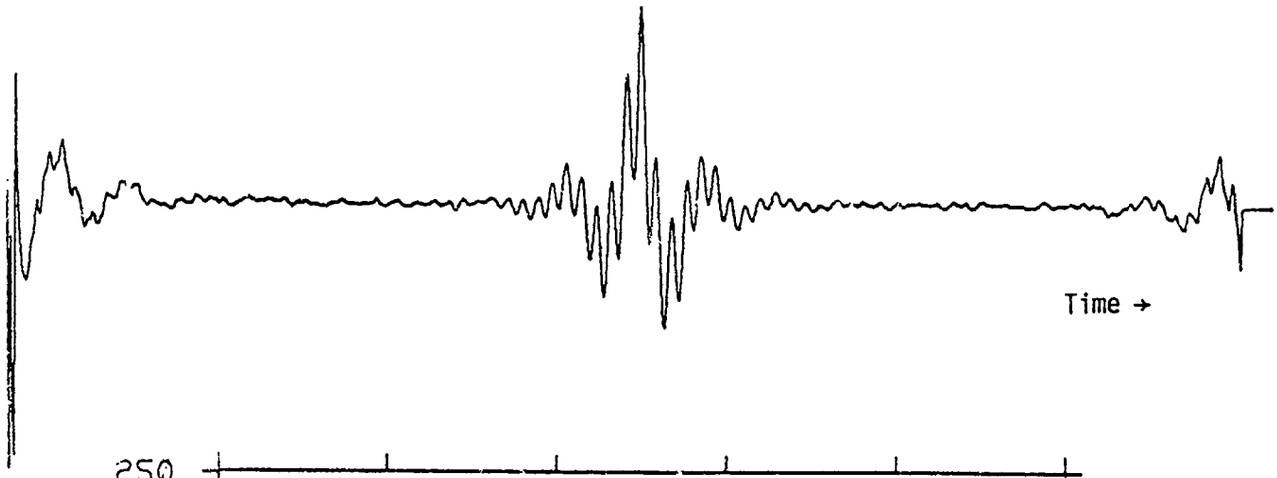

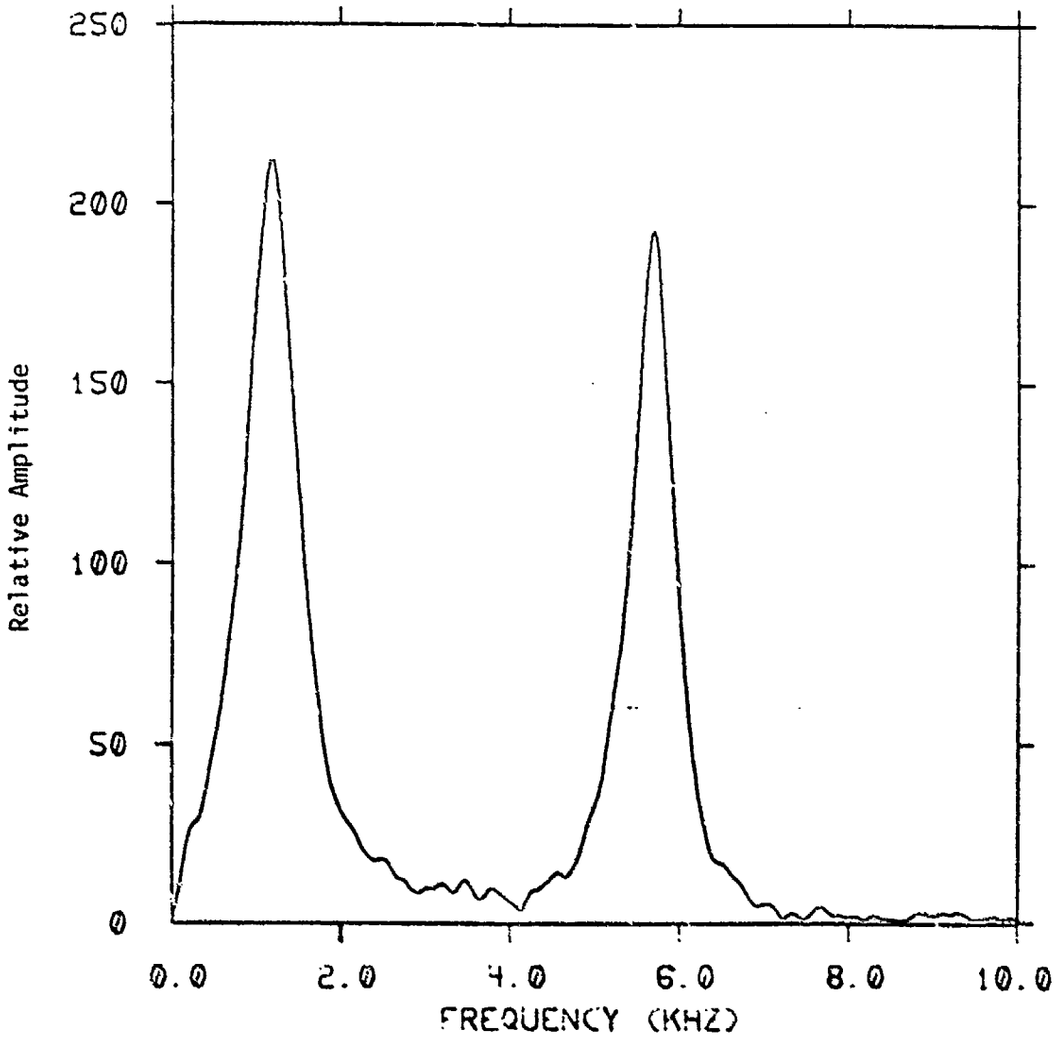

9-5/12 MONO 856.0KHZ 77K NSS=24000

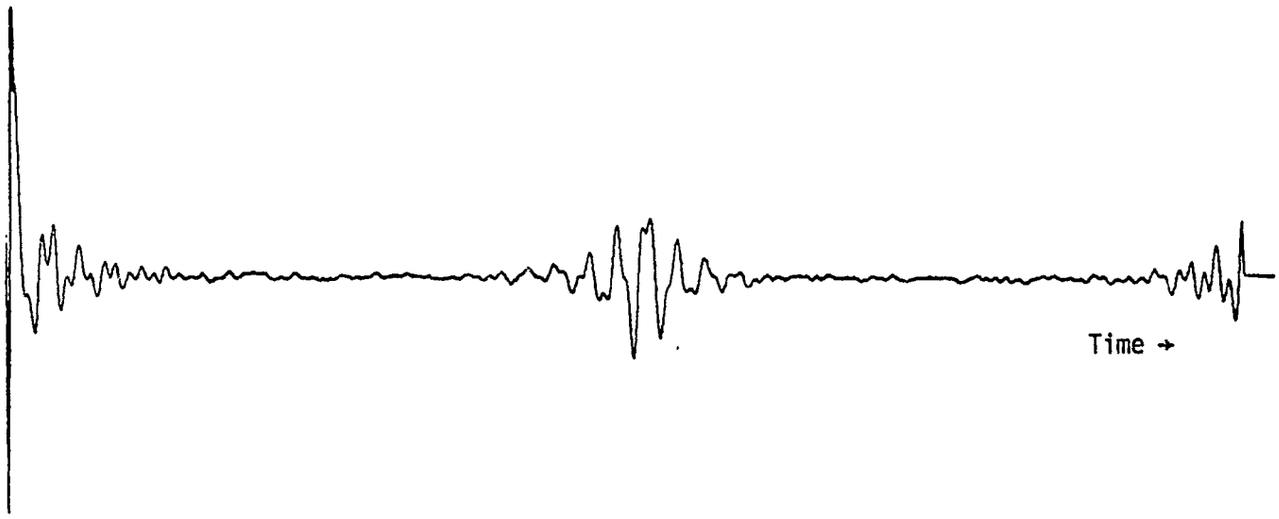

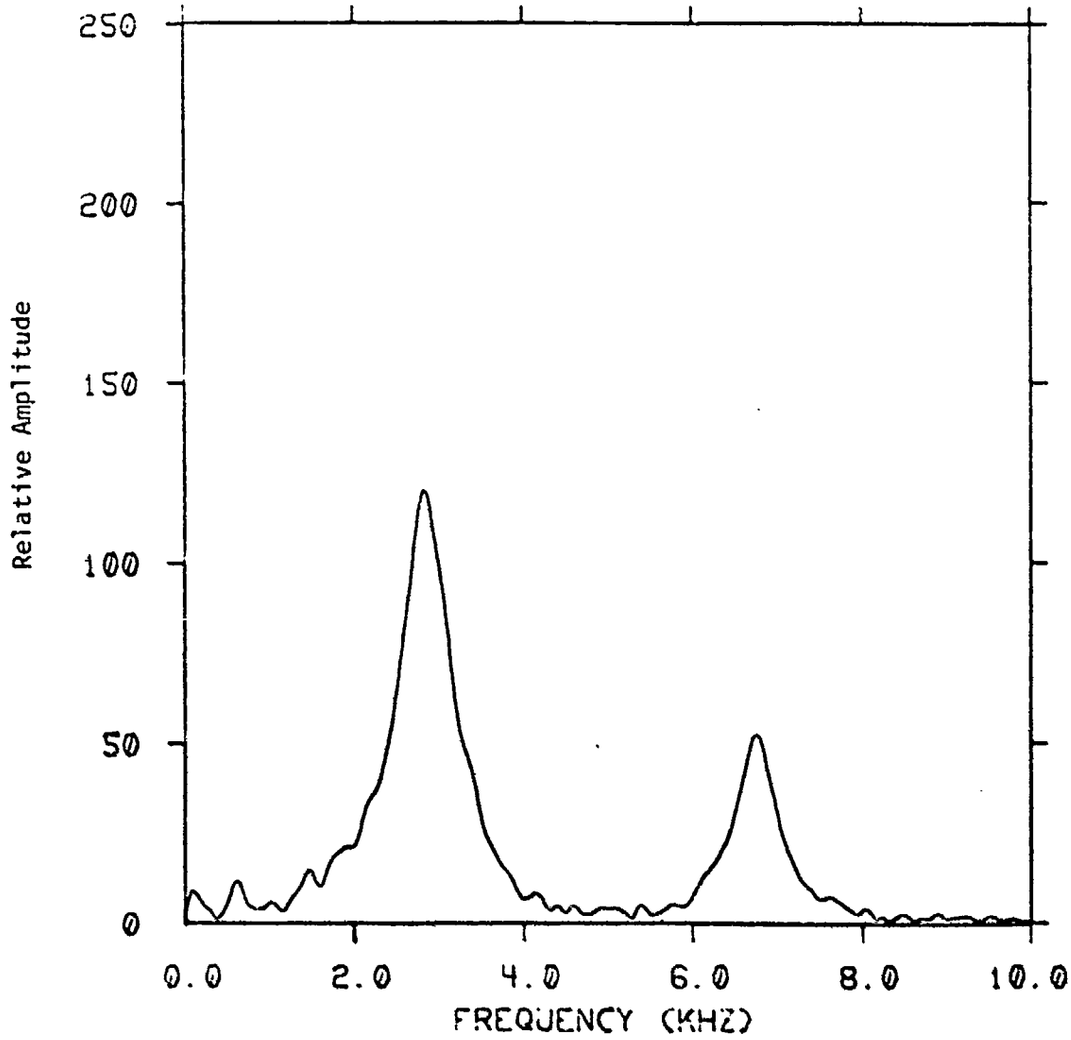

9-S/11 MONO 795.0KHZ 77K NSS=24000

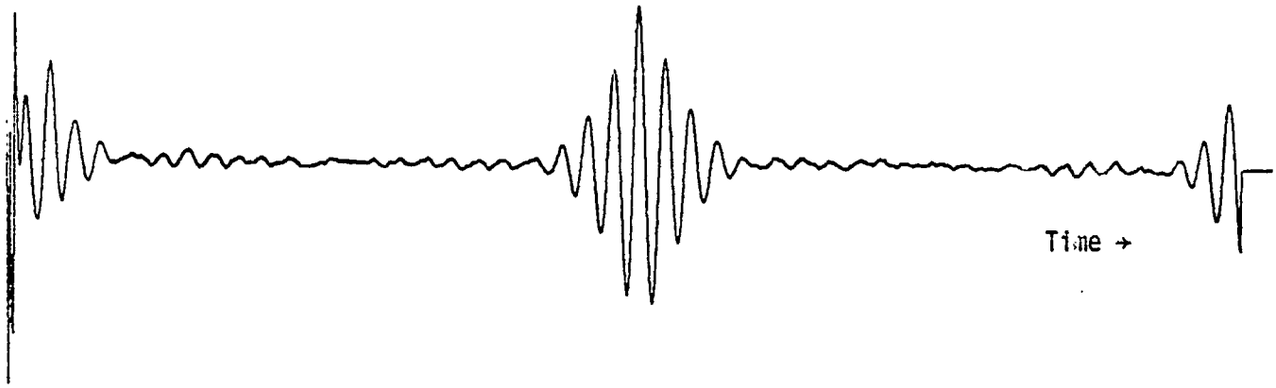

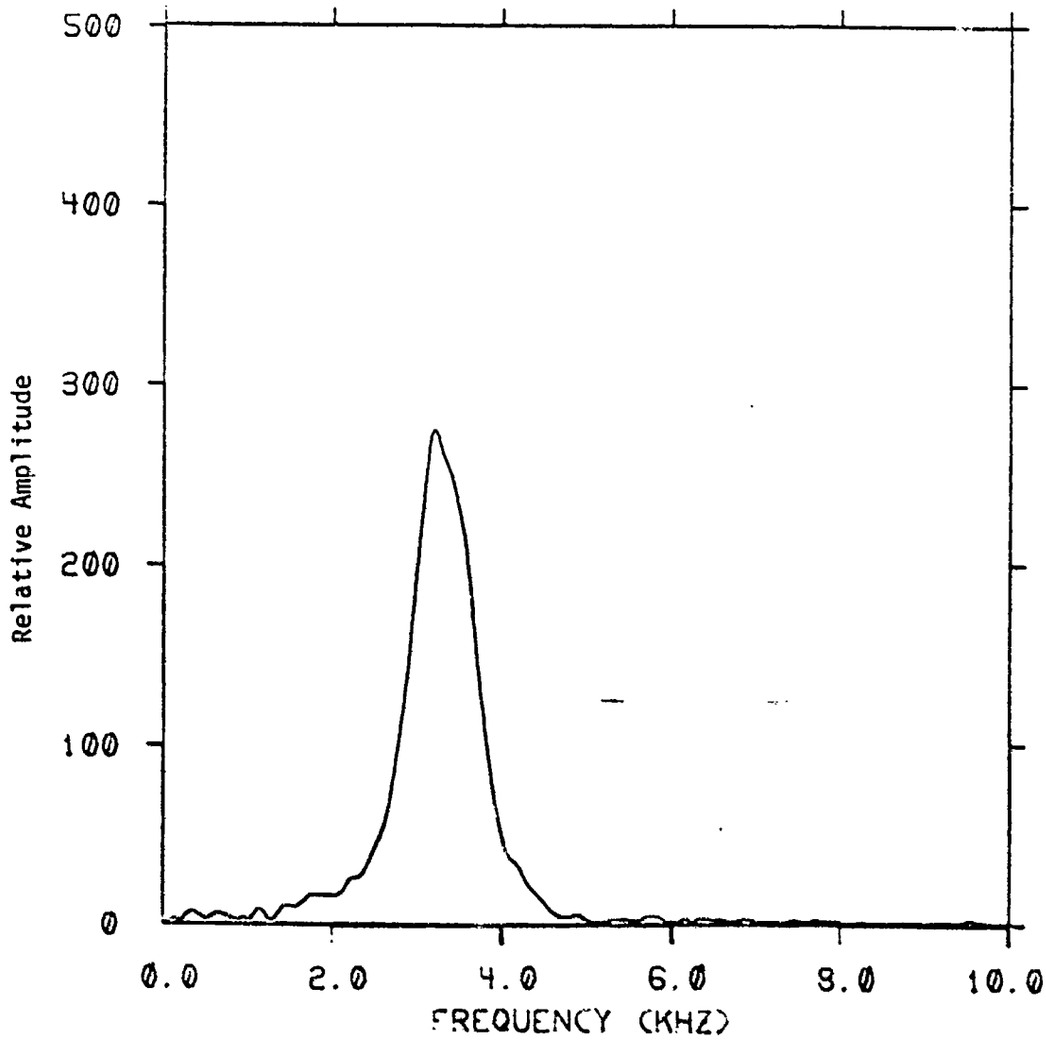

9-5/10 MONO 764.0KHZ 77K NSS=24000

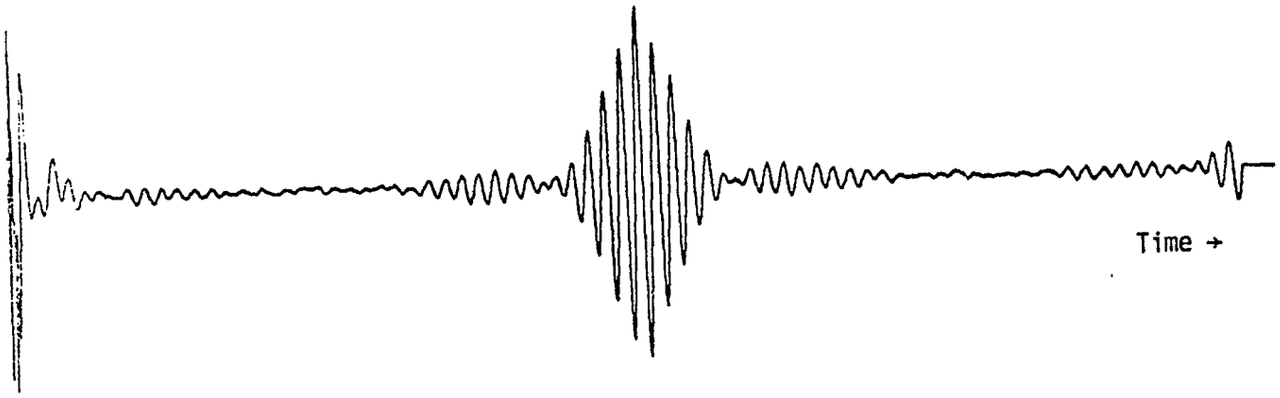

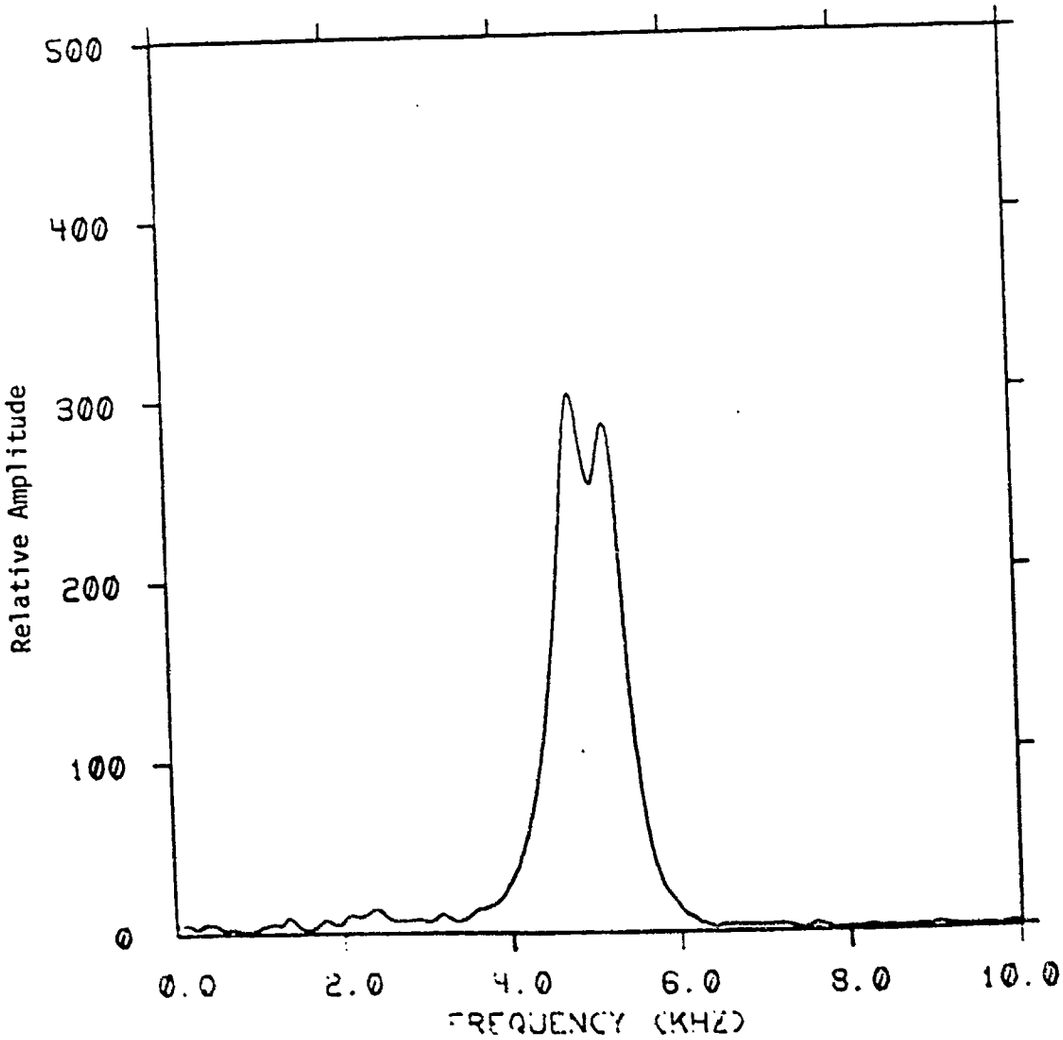

MONO 125.0KHZ 77K NSS=24000

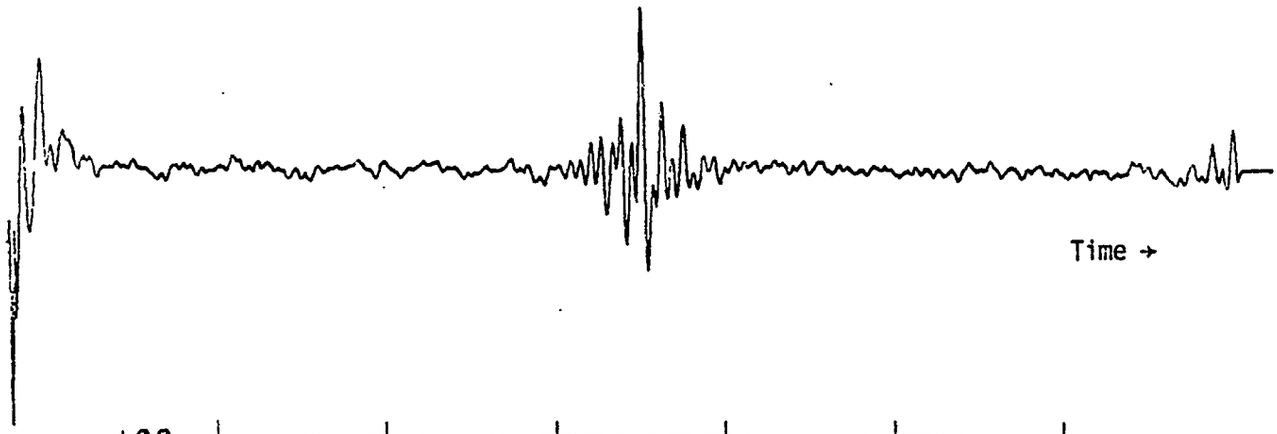

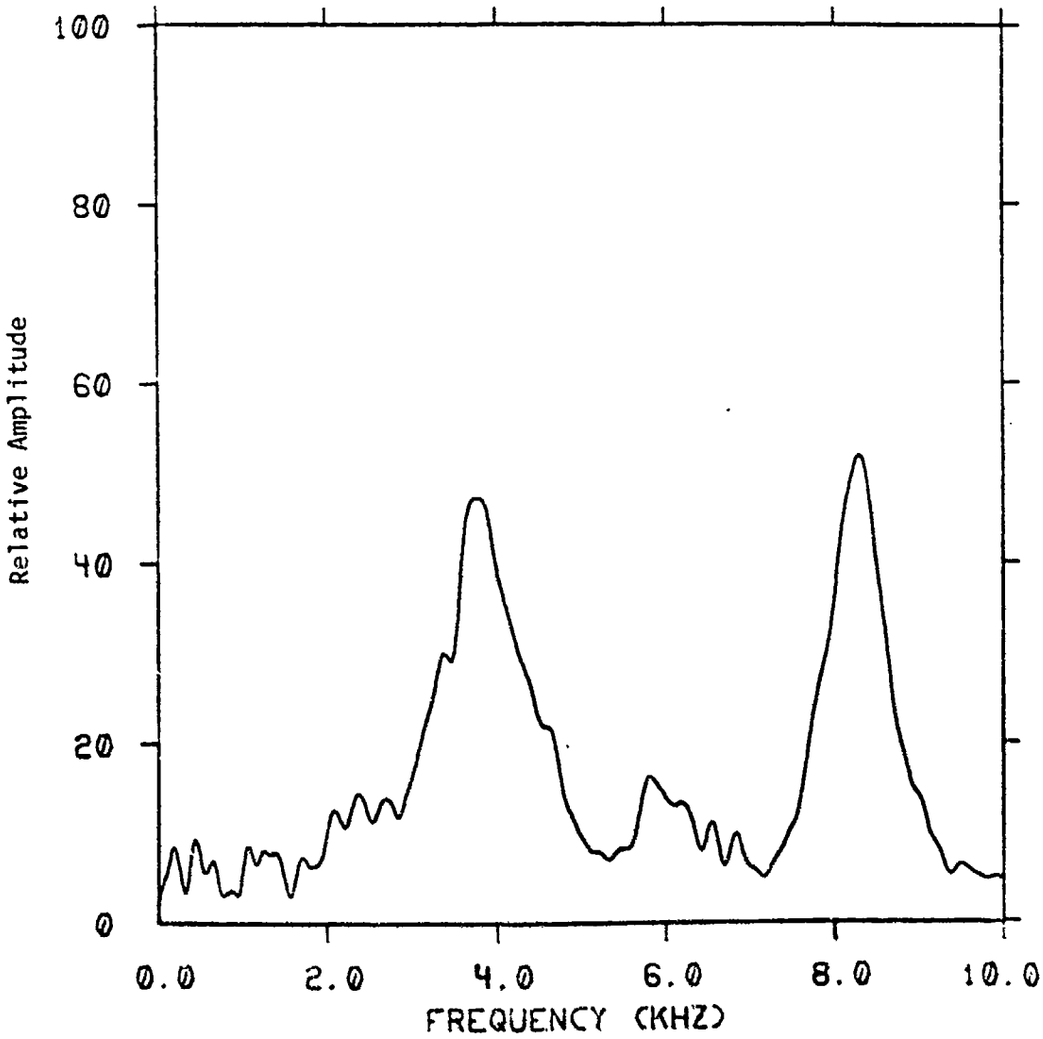

9-5/7 ORTHO 894.0KHZ 77K NSS=24000

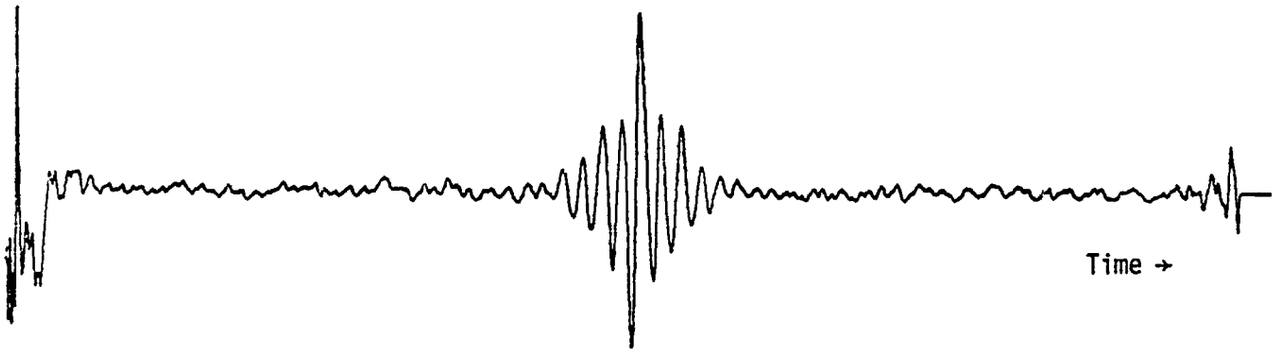

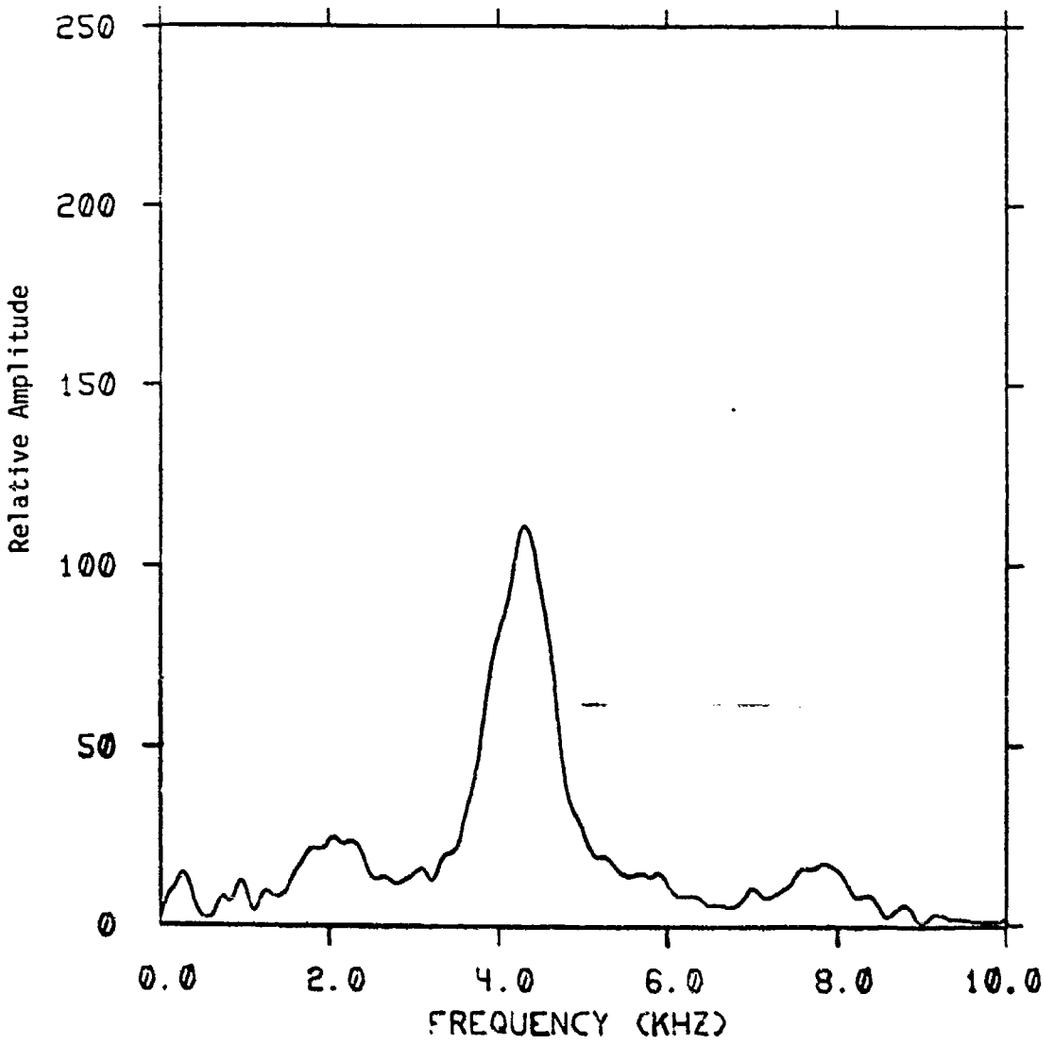

9-5/6 ORTHO 890.0KHZ 77K NSS=24000

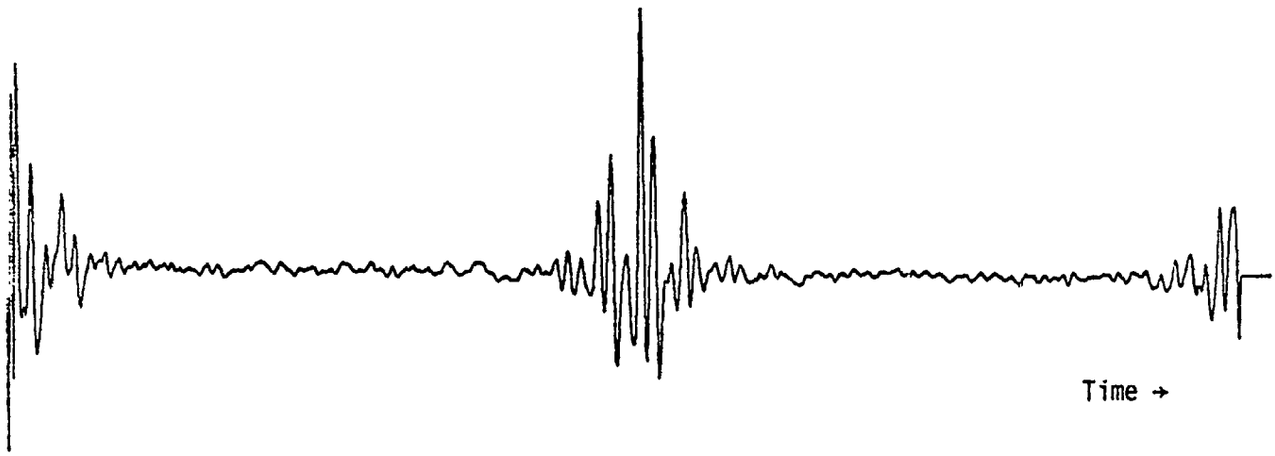

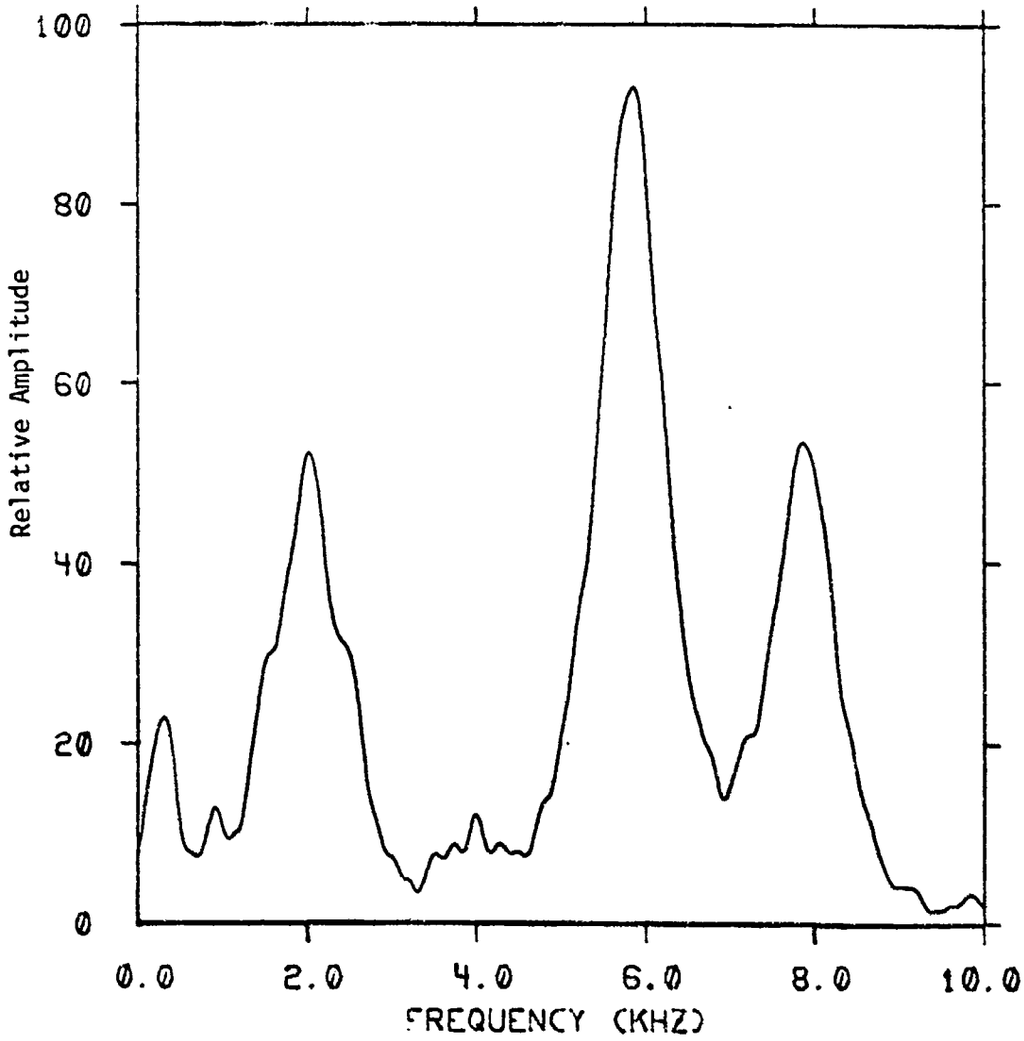

9-S/S ORTHO 870.0KHZ 77K NSS=24000

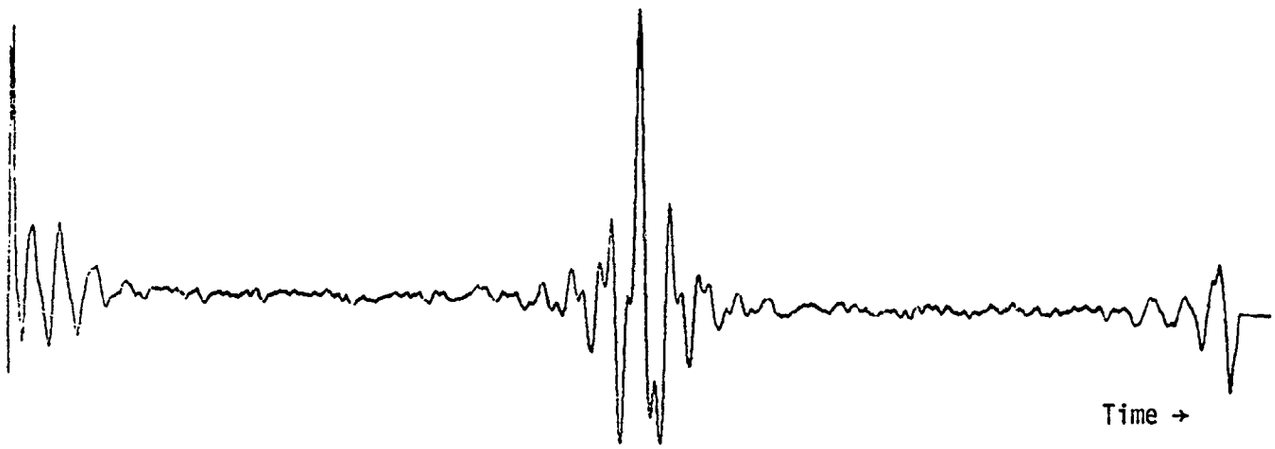

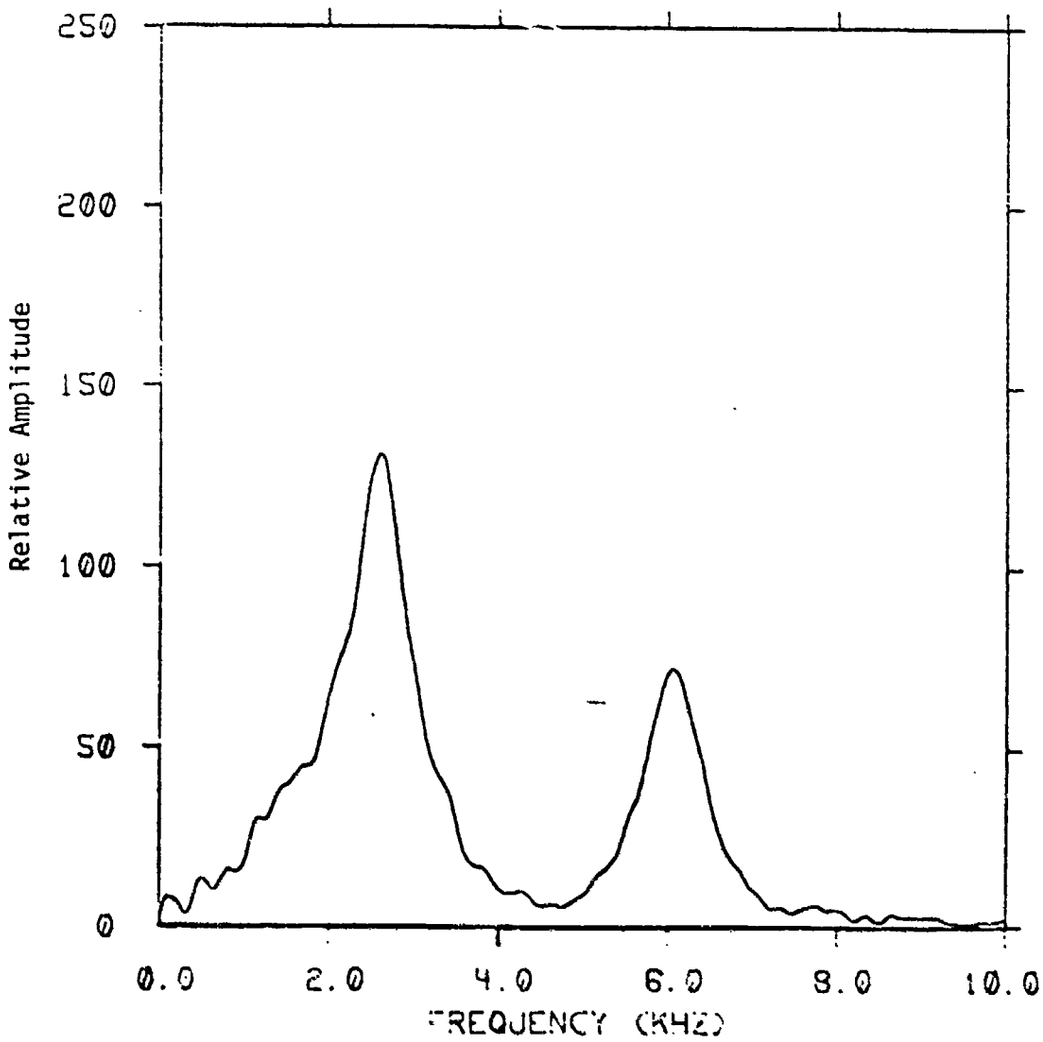

9-S/4 ORTHO 856.0KHZ 77K NSS=24000

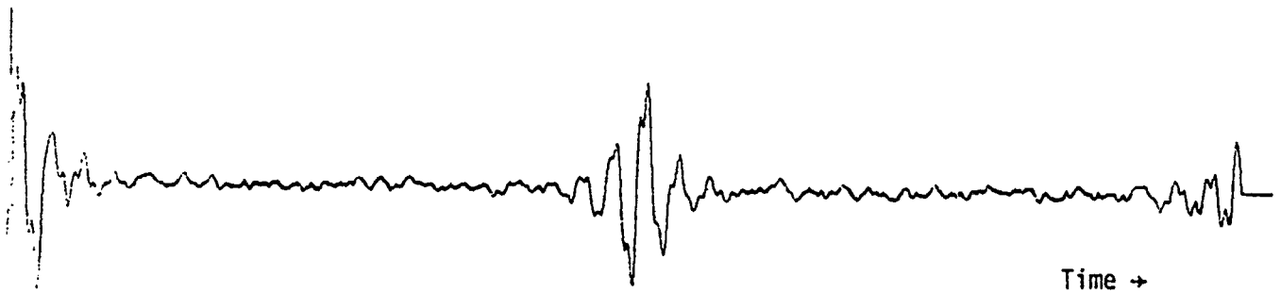

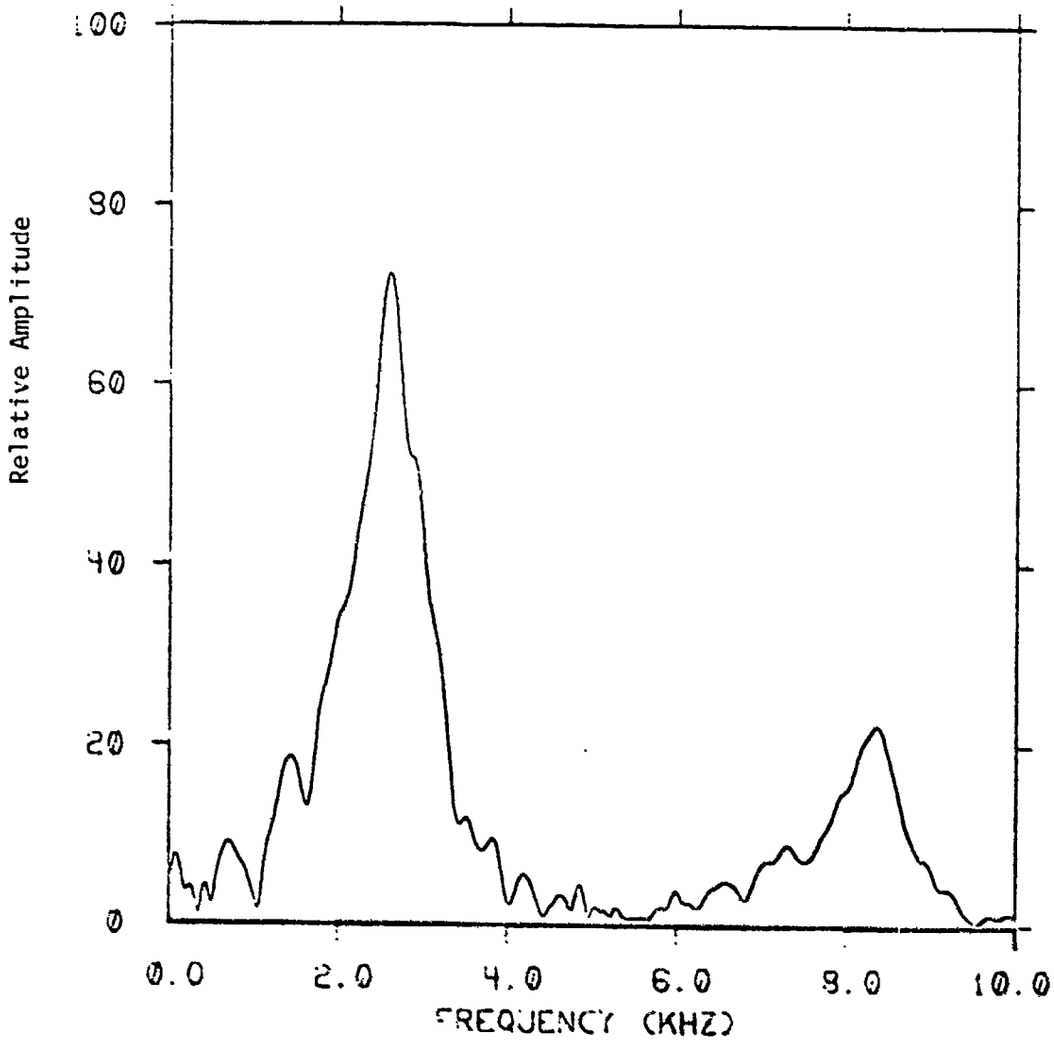

9-5/3 ORTHO 795.0KHZ 77K NSS=24000

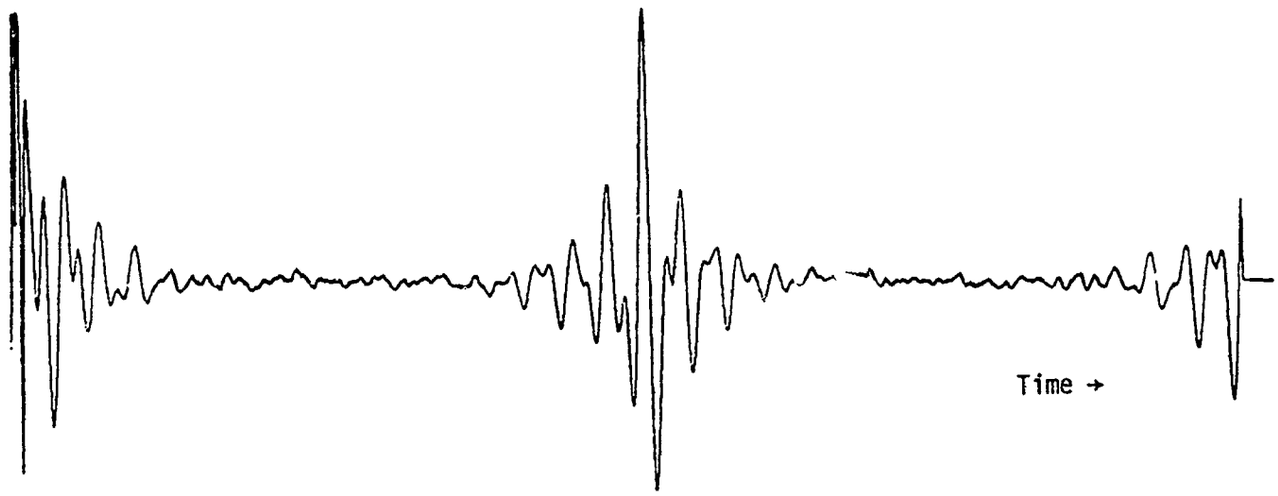

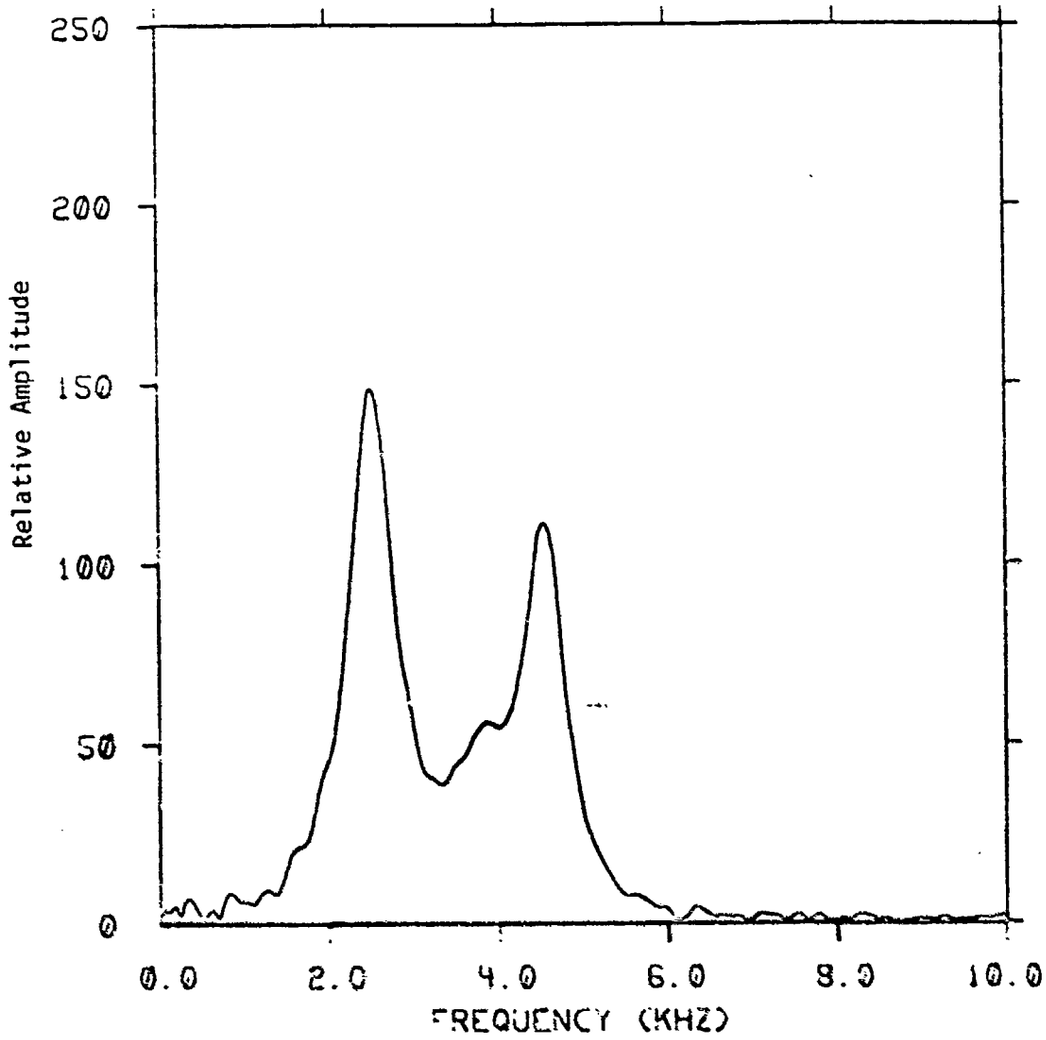

9-5/2 ORTHO 164.0KHZ 77K NSS=24000

APPENDIX C

BROADBAND FT SPECTRUM OF
EXCEPTIONALLY WIDE NQR LINES

C.1 BROADBAND FT SPECTRUM OF EXCEPTIONALLY WIDE NQR LINES

In Appendix C we collect the broadband FT spectrum of the three lines in the hydrogen-bonded complex Hexamethylenetetramine Hexahydrate, $HMT \cdot 6H_2O$. The experiment methods are described in Section 2.2.1. We shall limit the discussion in this Appendix to the actual data obtained; an analysis of the lineshape is beyond the scope of this work.

Figures C-1, C-2, and C-3 are the line-shapes of the three NQR lines in $HMT \cdot 6H_2O$, respectively called the ν_+, ν_- and ν_o lines. These spectra were obtained by adding together two "normalized" spectra obtained by setting the spectrometer frequency above and then below the average resonance frequency. The normalization was done by dividing the raw spectrum by the frequency response of the sample coil and receiver, and is not explicitly shown here. Figures C-4, C-5, and C-6 are composites showing the raw and normalized spectra from which Figures C-1, C-2 and C-3 were obtained.

BLOCK ENGINEERING

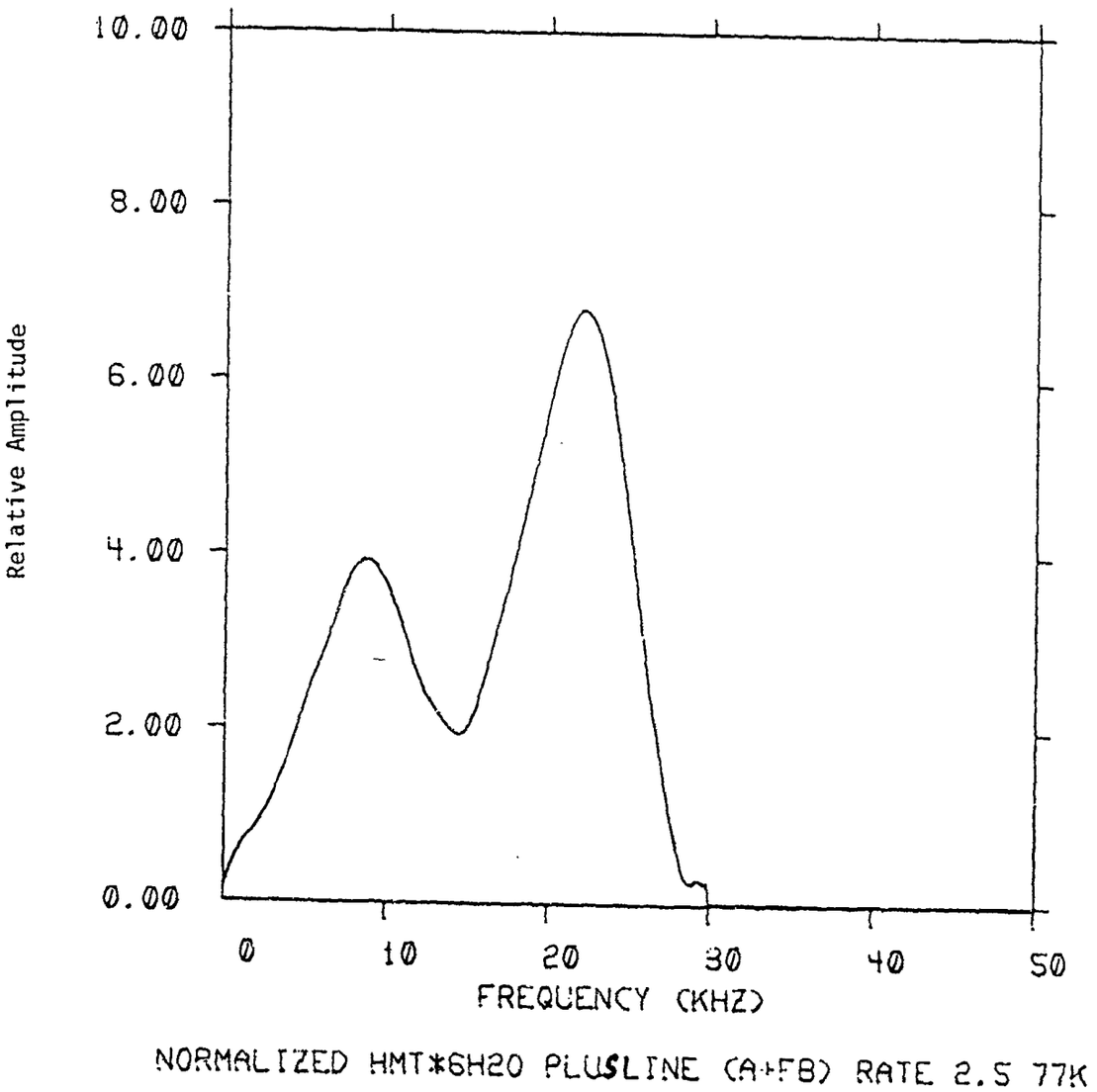

Figure C-1. Line Shape for the ν_+ line in HMT·$6H_2O$ at 77°K. The abscissa shows increasing frequency from 3235.0 kHz.

BLOCK
ENGINEERING

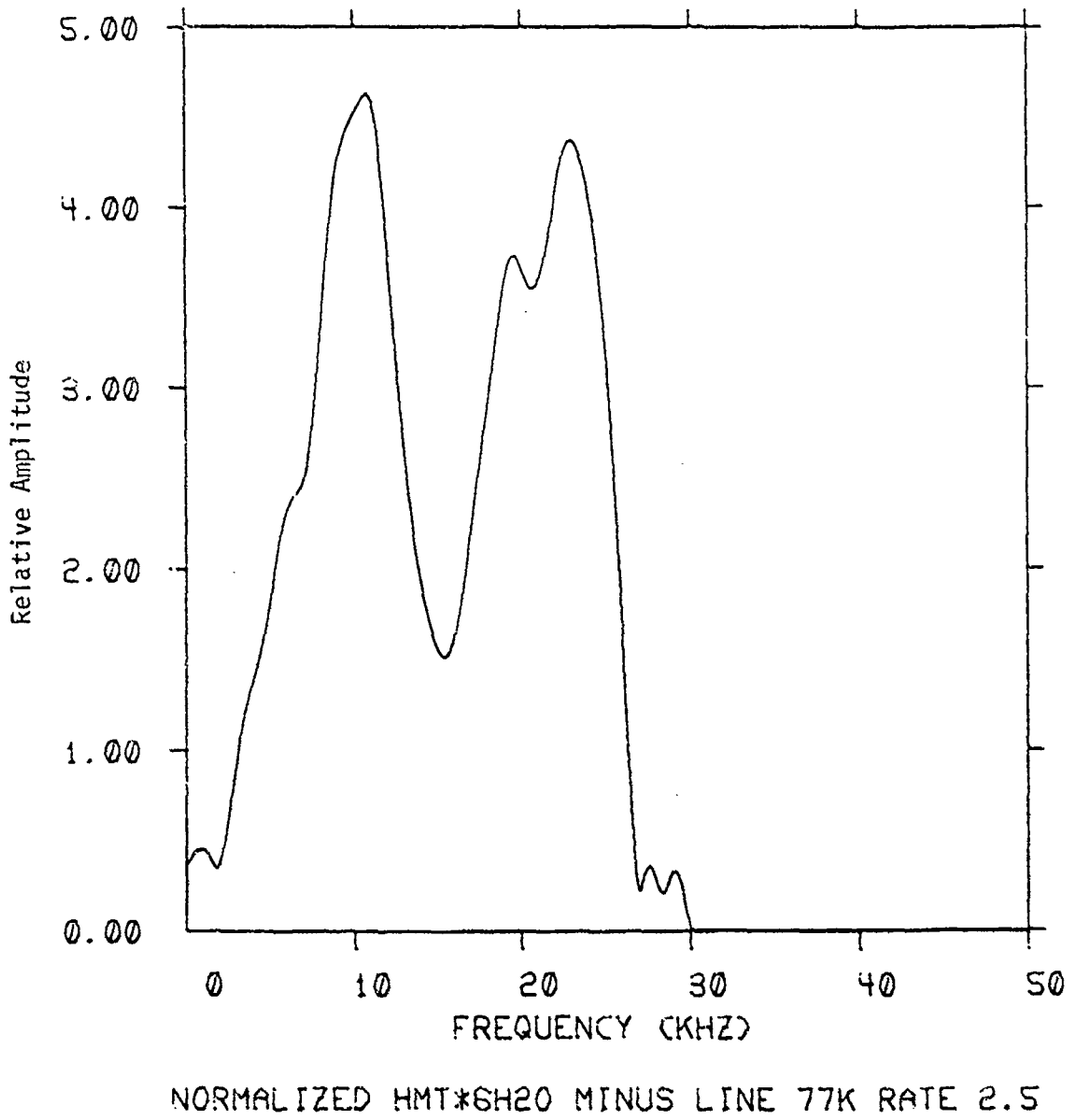

Figure C-2. Line Shape for the ν_- Line in $HMT \cdot 6H_2O$ at 77°K. The abscissa shows increasing frequency from 3140.0 kHz.

BLOCK ENGINEERING

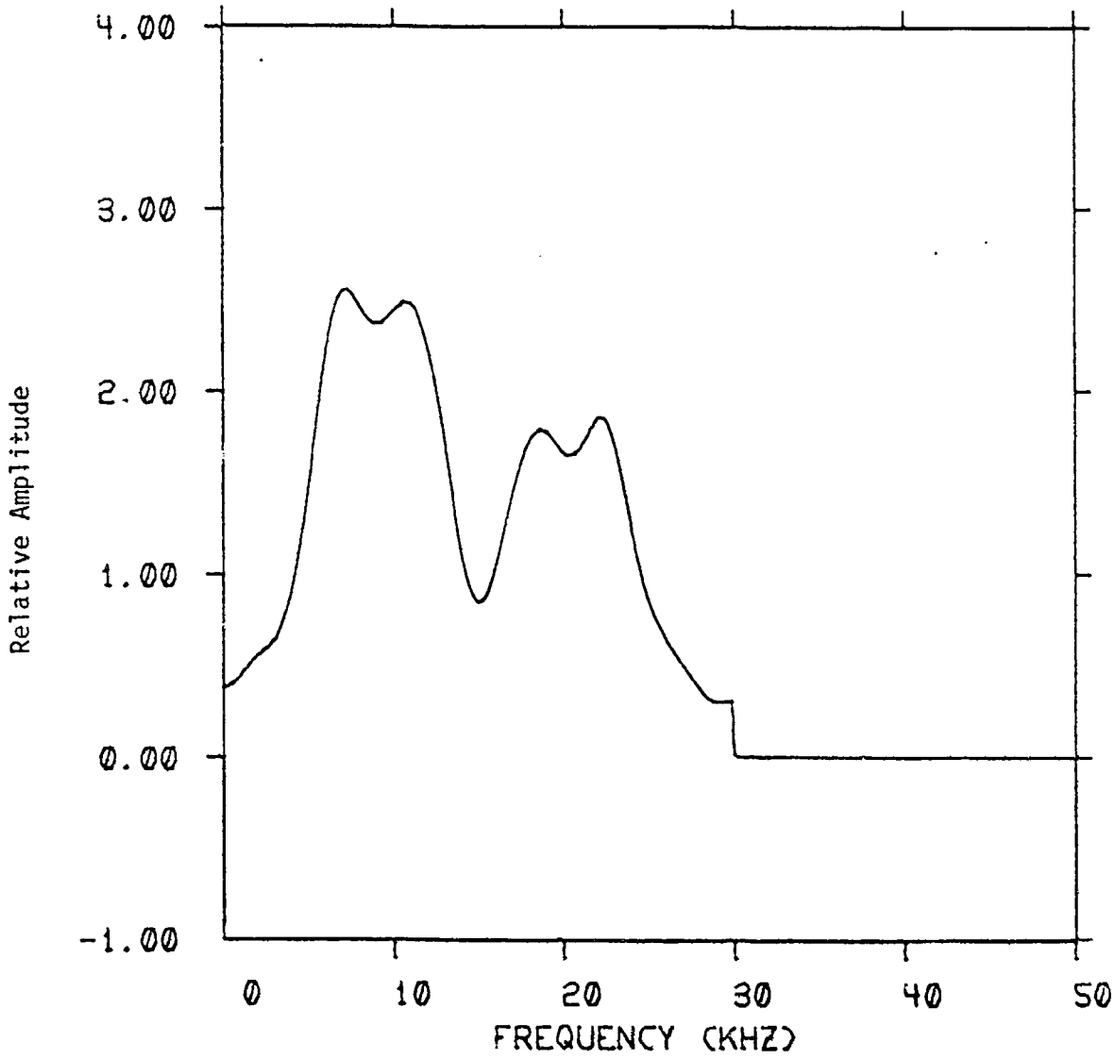

NORMALIZED HMT*6H2O ZERO LINE (A+FB) RATE 1.5 77K

Figure C-3. Line Shape for the ν_o line in $HMT \cdot 6H_2O$ at 77°K. The abscissa shows increasing frequency from 3560.0 kHz.

BLOCK ENGINEERING

Figure C-4

a) Time-domain spin-echo signal and modulus Fourier transform for the ν_+ line of HMT·$6H_2O$ at 77°K. The abscissa shows frequency increasing from the transmitter frequency at 3225 kHz.

b) Spectrum in (a) corrected for sample coil Q and receiver response.

c) Same as (a) but abscissa shows frequency decreasing from the transmitter frequency at 3255 kHz.

d) Spectrum in (c) corrected for sample coil Q and receiver response.

BLOCK
ENGINEERING

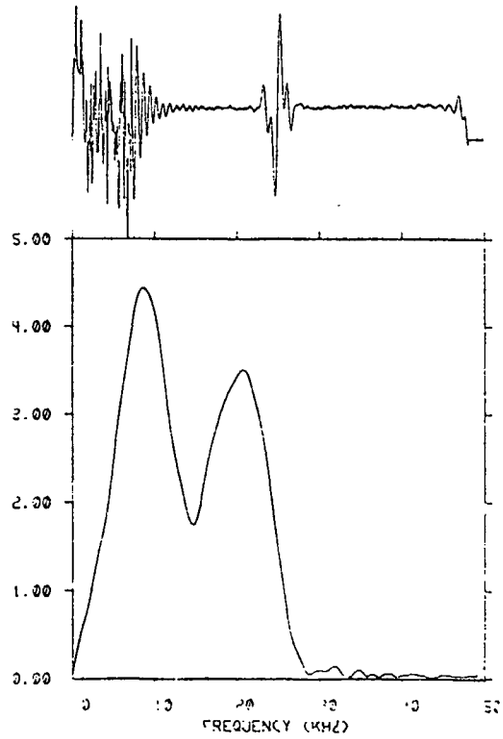

(a)

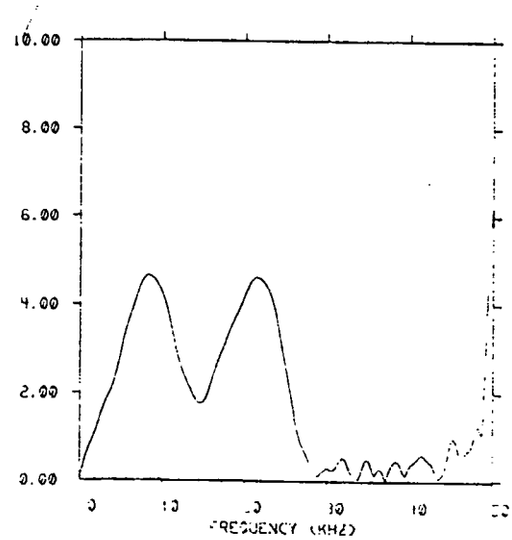

(b)

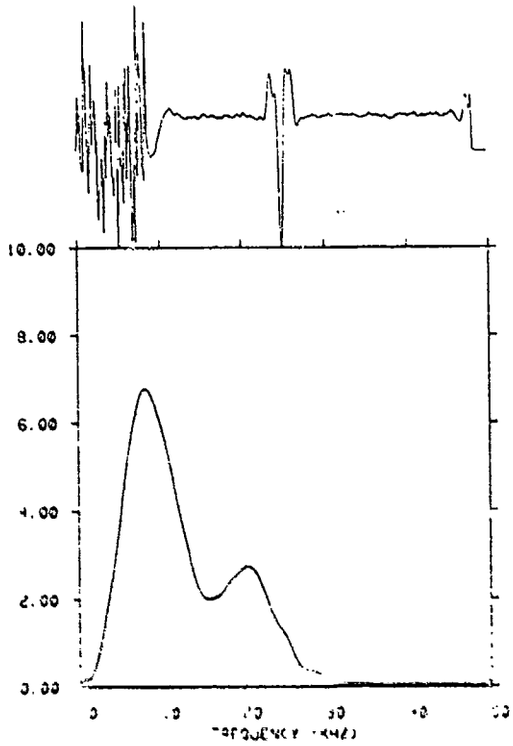

(c)

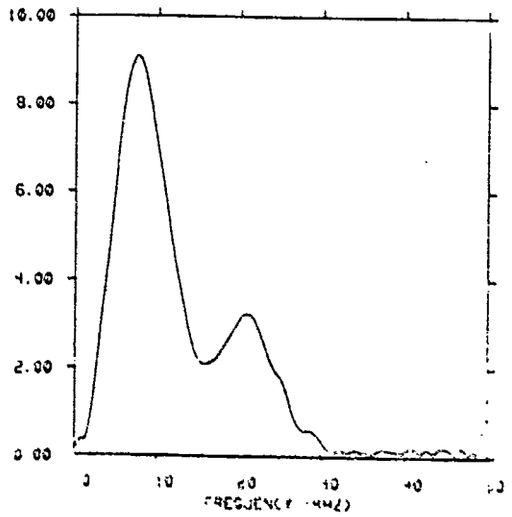

(d)

BLOCK ENGINEERING

Figure C-5

a) Time-domain spin-echo signal and modulus Fourier transform for the ν_- line of HMT·$6H_2O$ at 77°K. The abscissa shows frequency increasing to the right from the transmitter frequency at 3560 kHz.

b) Spectrum in (a) corrected for sample coil Q and receiver response.

c) Same as (a) but abscissa shows frequency decreasing from the transmitter frequency at 3590 kHz.

d) Spectrum in (c) corrected for the sample coil Q and receiver response.

BLOCK
ENGINEERING

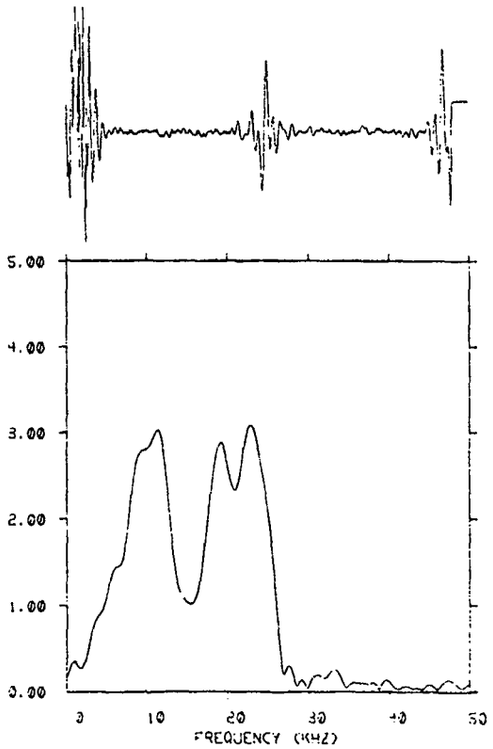

9-14/9 HMT6H20 3140.0KHZ 77K RATE 2.5

(a)

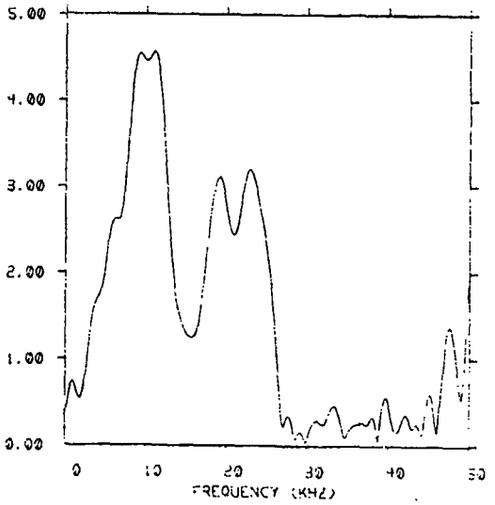

9-14/9 NORMALIZED HMT6H20 3140.0KHZ 77K RATE 2.5

(b)

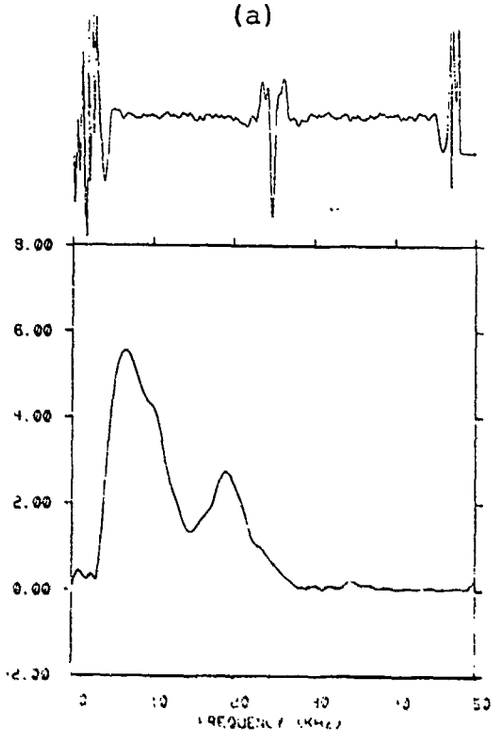

(c)

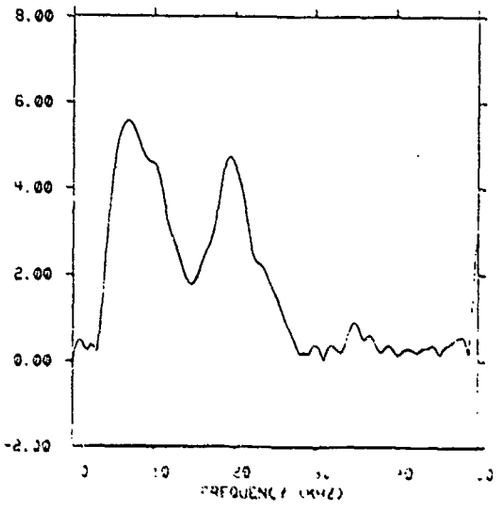

(d)

BLOCK
ENGINEERING

Figure C-6

a) Time-domain spin-echo signal and modulus Fourier transform for the ν_0 line of $HMT \cdot 6H_2O$ at 77°K. The abscissa shows frequency increasing from the transmitter frequency at 3560 kHz.

b) Spectrum in (a) corrected for sample coil Q and receiver response.

c) Same as (a) but abscissa shows frequency decreasing from the transmitter frequency at 3590 kHz.

d) Spectrum in (c) corrected for sample coil Q and receiver response.

BLOCK
ENGINEERING

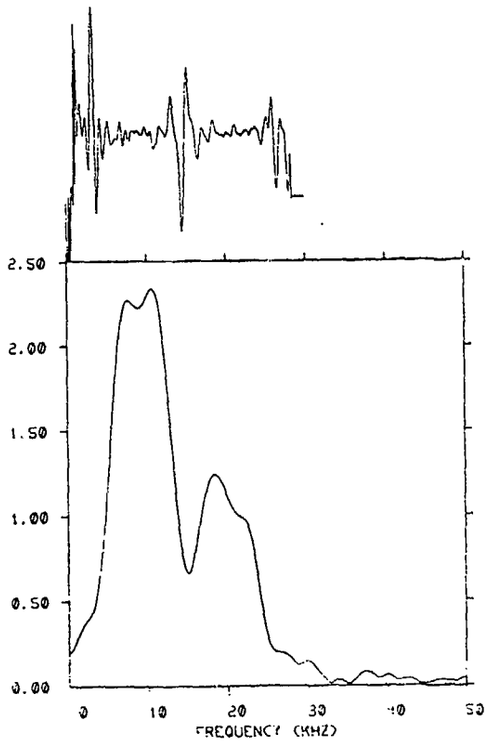

9-14/31 HMT*6H20 3560.0KHZ 77K RATE 1.5

(a)

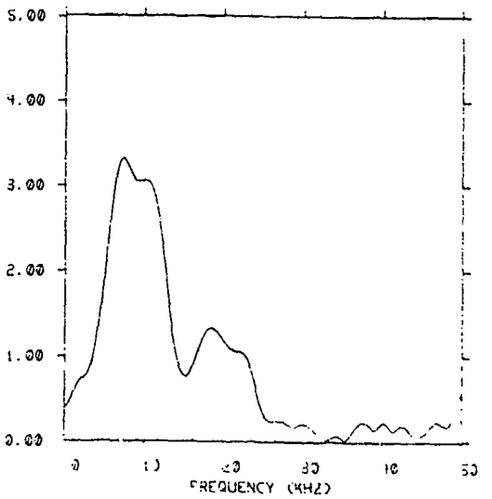

9-14/31 NORMALIZED HMT*6H20 3560.0KHZ 77K RATE 1.5

(b)

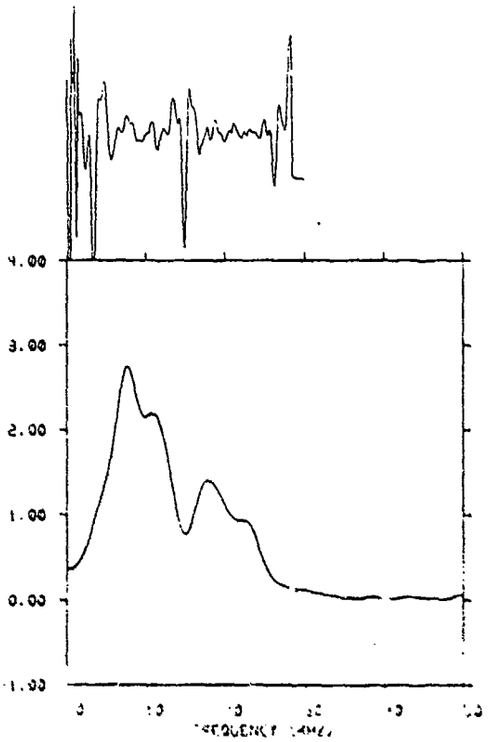

(c)

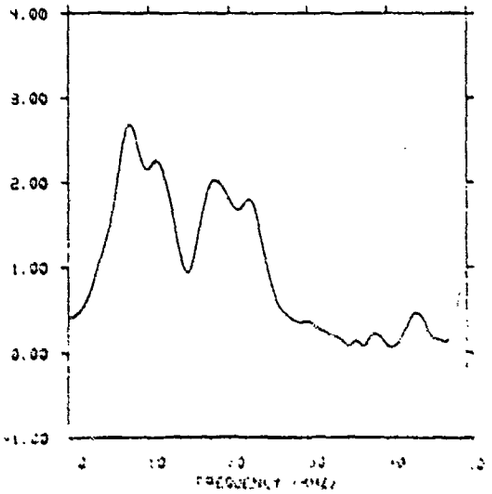

(d)

BLOCK ENGINEERING

APPENDIX D

PRINCETON APPLIED RESEARCH INTERFACE

In the original Block NQR spectrometer system, the analog signal with the associated status and clock timing information was bussed through a screen room wall via optocouplers. The signal was subsequently digitized and coadded by a Digilab® FTS 14 data system in real time.[1]

The maximum clock rate with this arragement was 50 kHz, which limited the bandwidth to 25 kHz.

In order to extend this, a Princeton Applied Research (PAR) signal averager Model 4202 was used to do the coaddition. This had clock rates to 200 kHz, and was directly usable on the NQR instrument with the available output gates.

However, it was necessary to read out the data from the averager into the data system for further processing in some manner.

The method used was to build an interface which read out the digitized data from the averager, converted it to analog form, and added a clock and status output. This data was then bussed through the optocouplers and coadded in the data system. The advantage of this approach was that it was easily implementable and minimized hardware changes. Also, the PAR 4202 has provisions for a hook up in this manner.[2]

[1] A Pulsed NQR-FFT Spectrometer for Nitrogen-14, J.C. Harding, Jr. et al, Journal of Mag. Resonance 36, 21-33 (1979).

[2] Model 4202 Signal Averager Operating and Service Manual Princeton Applied Research 1978.

The circuit shown in Figure D-1 performs these functions. Control of the PAR 4202 digital output is performed by the signals $\overline{\text{DIG ORIGIN RESTORE}}$, $\overline{\text{DIG DATA STROBE}}$ and $\overline{\text{DIG DATA VALID}}$.[3] The first signal resets the origin, while the other two signals handshake successive points out.

The circuitry is fairly straight forward. Switching from stop to start initializes the logic and the PAR 4202.

Subsequently the status is enabled and the 74LS629 clock starts. For each clock point the $\overline{\text{DIG OUTPUT STROBE}}$, $\overline{\text{DIG DATA VALID}}$ signals cause the PAR 4202 to put the digital value of the data point on its digital output lines. The monostable at U7 allows the D/A converter to settle, and then enables the clock out to the optocouplers.

At the 2048th clock point, if the start switch is still in the start position, the logic is reinitialized, and the sequence begins again; otherwise it stops.

Each data word of the PAR 4202 is 28 parallel bits, while the digital to analog converter is only 12 bits. In order to properly choose the appropriate 12 bits for the converter in a reasonable manner, the 28 bits were bussed to 28 successive terminals and a connector consisting of 12 successive matching terminals was constructed. The choice of which successive 12 bits to use is done by manually moving the connector and monitoring the output on a scope.

[3]Model 4202 Signal Averager Operating and Service Manual Princeton Applied Research 1978.

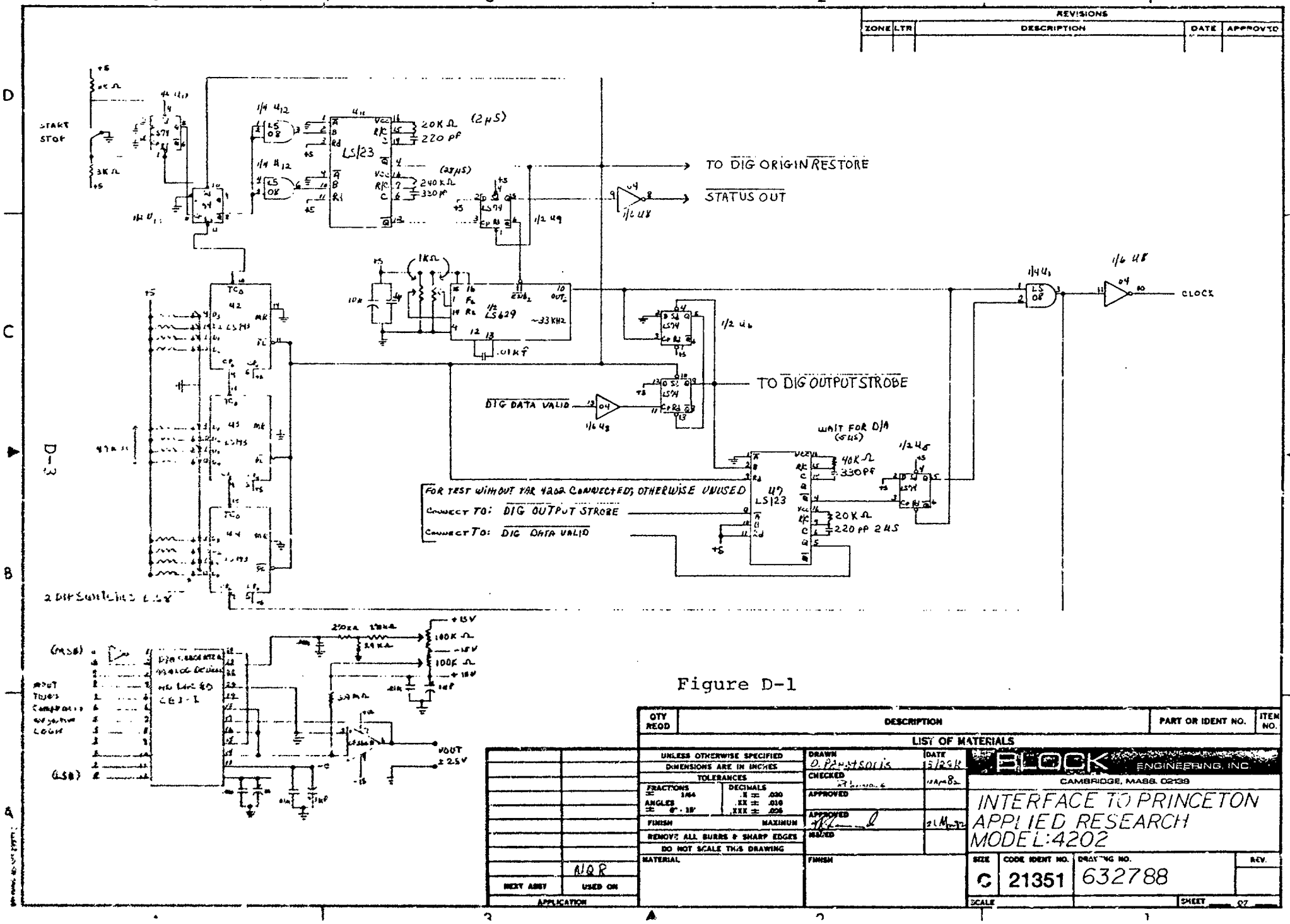
REVISIONS
ZONE
LTR
DESCRIPTION
DATE
APPROVED
START
STOP
TO DIG ORIGIN RESTORE
STATUS OUT
TO DIG OUTPUT STROBE
DIG DATA VALID
CLOCK
WAIT FOR D/A
FOR TEST WITHOUT PAR 4202 CONNECTED; OTHERWISE UNUSED
CONNECT TO: DIG OUTPUT STROBE
CONNECT TO: DIG DATA VALID
LS123
LS629
~33 KHZ
20K Ω
220 pF
240 K Ω
330 pF
1K Ω
.01 KF
40K Ω
330 PF
20K Ω
220 pF 2 μS
100K Ω
VOUT
± 2.5V
QTY REQD
DESCRIPTION
PART OR IDENT NO.
ITEM NO.
LIST OF MATERIALS
UNLESS OTHERWISE SPECIFIED
DIMENSIONS ARE IN INCHES
TOLERANCES
FRACTIONS
DECIMALS
ANGLES
FINISH
MAXIMUM
REMOVE ALL BURRS & SHARP EDGES
DO NOT SCALE THIS DRAWING
MATERIAL
DRAWN
CHECKED
APPROVED
ISSUED
FINISH
NEXT ASSY
USED ON
APPLICATION
BLOCK ENGINEERING, INC.
CAMBRIDGE, MASS. 02139
INTERFACE TO PRINCETON
APPLIED RESEARCH
MODEL:4202
SIZE
C
CODE IDENT NO.
21351
DRAWING NO.
632788
REV.
SCALE
SHEET

Figure D-1

REFERENCES

1. T.P. Das and E.L. Hahn, Nuclear Quadrupole Resonance Spectroscopy Solid State Physics", Suppl. 1, (Academic Press, New York, 1958.

2. E.A.C Lucken, Nuclear Quadrupole Coupling Constants, Academic Press, New York (1969).

3. D.T. Edmonds, Physics Reports 29, 233 (1977).

4. S.M. Klainer, T.B. Hirschfeld, and R.A. Marino, "Fourier Transform NQR" to appear in Fourier, Hadamard and Hilbert Transforms in Chemistry. A. Marshal, ed. (Plenum Press NY, 1982).

5. J.C. Harding, Jr., D.A. Wade, R.A. Marino, E.G. Sauer and S.M. Klainer, J. Mag. Res. 36, 21 (1979).

6. G.L. Petersen, Ph.D. Thesis, Brown University (1975).

7 a) A. Abragam, Principles of Nuclear Magnetism, (Oxford University Press, Oxford, 1961).

b) C.P. Slichter, Principles of Magnetic Resonance, (Springer-Verlag, Berlin, 1978).

8. G.W. Leppelmeier and E.L. Hahn, Phys. Rev. 141, 724 (1966).

9. H.Y. Carr and E.M. Purcell, Phys. Rev. 94, 630 (1954).

10. S. Meiboom and D. Gill, Rev. Sci, Instr. 29, 688 (1958).

11. R.A. Marino and S.M. Klainer, J. Chem. Phys. 67, 3388 (1977).

12. E.D. Ostroff and J.S. Waugh, Phys. Rev. Letters, 16, 1097 (1966).

13. J.S. Waugh, J. Mol. Spec. 35, 298 (1970).

14. R.S. Cantor and J.S. Waugh, J. Chem. Phys. 73, 1054 (1980).

15. J.C. Pratt, P. Raghunathan and C.A. McDowell, J. Chem. Phys. 61, 1016 (1974) and J. Mag. Res. 20, 313 (1975).

BLOCK ENGINEERING

16. R. Lenk and E.A.C. Lucken, Pure Applied Chem. 40, 199 (1974).

17. A. Colligiani and R. Ambrosetti, Gazz. Chim. Italiana 106, 439 (1976).

18. A. Colligiani and R. Ambrosetti, J. Chem. Phys. 60, 1871 (1974).

19. D.G. Grabar, F.C. Rauch and A.J. Fanelli, J. Phys. Chem., 73, 3514 (1969).

20. W. Connick, F.G.J. May, and B.W. Thorpe, Aust. J. Chem. 22, 2685 (1969).

21. E. Artini, R.C. Accad. Lincei 24, 274 (1915).

22. E. Hertel and G. Römer, Z. Phys. Chem. B, 2, 77 (1930).

23. L.A. Burkardt and H.H. Bryden, Acta Cryst. 7, 135 (1954).

24. J.R.C. Duke, Private Communication (1979).

25. P. Friedlander, Z. Kristallogr, 3, 169 (1879).

26. R. Hultgren, J. Chem. Phys. 4, 84 (1936).

27. W.C. McCrone, Microchem, J. Symp. Ser. 2, 243 (1962).

28. J.R.C. Duke, Private Communication (1982).

29. J.L. Soderberg, J.S. Back, C.L. Hakanson, U.S. Patent 3,620, 857 (1971).

30. D.K. Philp and B.W. Thorpe, J. Cryst. Growth 35(2) 133.(1976)

31. M.A. Parry and B.W. Thorpe, Rep. -Aust. Mater. Res. Lab. 1978, MRL-R-708 and 1979 MRL-R-748.

32. C.H. Townes and B.P. Dailey, J. Chem. Phys. 17, 782 (1949).

33. E. Schempp and P.J. Bray, in Physical Chemistry: An Advanced Treatise Vol. 4, Academic Press, New York, 1970 p 521.

BLOCK ENGINEERING

34. S.N. Subbarao and P.J. Bray, J. Chem. Phys. 67, 3947 (1977).

35. C.P. Cheng and T.L. Brown, J. Mag. Res. 28, 391 (1977).

36. J. Trotter, Acta Cryst. 12, 884 (1959).

37. J.V. Barve and L.M. Pant, Acta Cryst. B27, 1158 (1971).

38. S.C. Abrahams, Acta Cryst. 3, 194 (1950) and J. Trotter, Can. J. Chem 39, 1638 (1961).

39. T. Higashi and K. Osaki, Acta Cryst. B33, 2337 (1977).

40. E.M. Gopalakrishna, Zeitsch Krist 121, S. 378 (1965).

41. C.S. Choi and J.E. Abel, Acta Cryst B28, 193 (1972).

42. J. Trotter, Acta Cryst. 14, 244 (1961) and Can. J. Chem. 39, 1639 (1961).

43. J.H. Bryden, Acta Cryst. B28, 1395 (1972).

44. T.C. Wang, Phys. Rev. 99, 566 (1955).

45. H. Chihara, N. Nakamura, H. Okuma, J. Phys. Soc. Japan, 24, 306 (1968).

46. This material is adopted from our article: The Contribution by Landers and Brill was supported by the Air Force Office of Scientific Research, under grant number AFOSR-80-0258. A.G. Landers, T.B. Brill and R.A. Marino, J. Phys. Chem 85, 2618 (1981).

47. F. Goetz and T.B. Brill, J. Phys. Chem. 83, 340 (1979).

48. F. Goetz, T.B. Brill, and J.R. Ferraro, J. Phys. Chem. 82, 1912 (1978).

49. A.G. Landers and T.B. Brill, J. Phys. Chem. 84, 3573 (1980).

50. T.B. Brill, and F. Goetz, Proc. Austronaut, Aeronaut, 61, 7, (1978) and J. Chem. Phys. 65, 1217 (1976).

BLOCK
ENGINEERING

51. H.S. Gutowsky and D.W. McCall, J. Chem. Phys. 32, 548 (1960).

52. G.G. Moross, H.S. Story, J. Chem. Phys. 45 3370 (1966).

53. B.L. Barton, J. Chem. Phys. 54, 814 (1971) and 46, 1553 (1967).

54. J. Murgich, J. Chem. Phys. 70 1198 (1979).

55. G. Petersen and T. Oja, Adv. NQR Spectroscopy 1, 179 (1979).

56. L. Guibe, Fortsch. Chem. Forsch, 30, 77 (1972).

57. C.S. Choi, H.P. Boutin, Acta Cryst. B26, 1235 (1970).

58. S. Vega, J. Chem. Phys. 60, 3884 (1974).

59. M. Minematsu, J. Phys. Soc. Japan 14, 1030 (1959).

60. D.H. Smith, R.M. Cotts, J. Chem, Phys. 41, 2403 (1964).

61. S.N. Subbarao and P.J. Bray, J. Chem. Phys. 67, 1085 (1977).

62. J.J. Kaufman, Johns Hopkins Univeristy, Private Communication, 1981.

63. T.B. Brill, C.O. Reese, J. Phys. Chem. 84, 1376 (1980).

64. S. Bulusu, J.R. Autera and T. Axenrod, J.C.S. Chem. Comm., 1973, 602.

65. C.S. Choi and E. Prince, Acta Cryst. B28, 2857 (1972).

66. T. Kushida, G.B. Benedek and N. Bloembergen, Phys. Rev. 104, 1364 (1956).

67. E.R. Andrew and R.G. Eades, Proc. Roy. Soc. A218, 537 (1953).

68. A. Zussman and M. Oron, J. Chem. Phys. 66, 743 (1977).

BLOCK ENGINEERING